

An Efficient Multiscale Method for Modeling Progressive Damage in Composite Materials

vom Fachbereich Maschinenbau und Verfahrenstechnik
der Technischen Universität Kaiserslautern
zur Verleihung des akademischen Grades
Doktor-Ingenieur (Dr.-Ing.)
genehmigte Dissertation

von
M.Sc. Johannes Spahn
aus Würzburg

Hauptreferent: PD. Dr. Heiko Andrä
Korreferenten: Prof. Dr.-Ing. Ralf Müller
Prof. Christian Linder
Vorsitzender: Prof. Dr.-Ing. Tilmann Beck
Dekan: Prof. Dr.-Ing. Christian Schindler

Tag der Einreichung: 12.06.2014
Tag der mündlichen Prüfung: 09.12.2014

Kaiserslautern, 2015

D 386

Herausgeber

Lehrstuhl für Technische Mechanik
Technische Universität Kaiserslautern
Gottlieb-Daimler-Straße
Postfach 3049
67653 Kaiserslautern

© Johannes Spahn

Ich danke der „Prof. Dr. Hans Georg und Liselotte Hahn Stiftung“ für die finanzielle Unterstützung bei der Drucklegung.

Druck

Technische Universität Kaiserslautern
ZTB – Abteilung Foto-Repro-Druck

Alle Rechte vorbehalten, auch das des auszugsweisen Nachdrucks, der auszugsweisen oder vollständigen Wiedergabe (Photographie, Mikroskopie), der Speicherung in Datenverarbeitungsanlagen und das der Übersetzung.

ISBN 978-3-942695-09-1

Vorwort

Die vorliegende Arbeit entstand während meiner Tätigkeit als Stipendiat am Fraunhofer Institut für Techno- und Wirtschaftsmathematik in der Abteilung Strömungs- und Materialsimulation sowie am Lehrstuhl für Technische Mechanik der Technischen Universität Kaiserslautern im Zeitraum von 2011 bis 2014.

Mein besonderer Dank gilt Herrn Prof. Dr.-Ing. Ralf Müller und PD Dr. Heiko Andrä für die in jeder Hinsicht hervorragende Betreuung und Unterstützung meiner wissenschaftlichen Arbeit. Weiterhin danke ich Herrn Prof. Christian Linder für die Übernahme des Korreferats. Ich bedanke mich für die Ermöglichung meines Forschungsaufenthalts an der Stanford University in Kalifornien im Herbst 2013, bei dem ich viele einzigartige Erfahrungen und Eindrücke sammeln konnte. Herrn Prof. Dr.-Ing. Tilmann Beck danke ich vielmals für die Übernahme des Prüfungsvorsitzes.

Ich danke allen direkten Kollegen am Fraunhofer ITWM, die mich bei meiner Promotion fachlich unterstützt haben, dabei insbesondere, neben vielen anderen, Dr. Tobias Zangmeister und Dr. Matthias Kabel. Von ganzem Herzen bedanken möchte ich mich bei allen weiteren Kollegen die mich während meiner Promotionszeit begleitet haben, und stets für eine sehr angenehme und kollegiale Atmosphäre gesorgt haben. Mein besonderer Dank gilt Dr. Janis Sliseris für die spannenden fachlichen Diskussionen und die Begleitung bei zahlreichen sportlichen Aktivitäten, Dr. Marco Buck, Dr. Clément Zémerli und vielen mehr, die dazu beigetragen haben, dass ich die Zeit für immer in guter Erinnerung behalten werde!

Zu guter Letzt möchte ich meinen Eltern und meinem Bruder für Ihre bedingungslose und fortwährende Unterstützung nicht nur während meiner Promotion bedanken!

Ingolstadt, im Januar 2015

Johannes Spahn

„Das, wobei unsere Berechnungen versagen, nennen wir Zufall :-)“
(Albert Einstein)

Kurzfassung

Faserverstärkte Verbundmaterialien nehmen in zukünftigen industriellen Leichtbauanwendungen eine zentrale Bedeutung ein, insbesondere im Hinblick auf die aktuellen Entwicklungen im Bereich Elektromobilität. Komposite besitzen jedoch ein sehr komplexes Materialverhalten. Da experimentelle Untersuchungen teuer und zeitaufwendig sind, werden fortschrittliche Simulationsmethoden benötigt, um diese Materialien effektiv einsetzen zu können. Speziell die Modellierung von Schädigung und Versagen stellt eine große Herausforderung dar. Konventionelle makromechanische Methoden sind in vielen Anwendungen nicht ausreichend, um die korrekte Materialantwort vorherzusagen. Das Versagen von Verbundmaterialien geschieht infolge verschiedener mikromechanischer Schädigungsmechanismen in den einzelnen Materialphasen. Diese Effekte müssen berücksichtigt werden, um das Materialverhalten korrekt zu simulieren. Daher wurden verschiedene Multiskalen-Modellierungs- und Simulationstechniken entwickelt, die das mikromechanische Materialverhalten berücksichtigen. Multiskalenmethoden, die auf analytischen Abschätzungen oder semi-analytischen Interpolationsmethoden basieren, sind nur für einfache Materialeinschlüsse geeignet oder in ihrer Anwendbarkeit für komplexe, makroskopische Lastfälle begrenzt. Daher muss auf gekoppelte Simulationsmethoden zurückgegriffen werden. Bei diesen werden die mikrostrukturellen Bestandteile explizit modelliert und die resultierende Materialantwort wird in einer gekoppelten Simulation erhalten. Im Zuge des damit verbundenen Anstiegs der im System erhaltenen Freiheitsgrade ist eine effiziente Lösung des mikromechanischen Randwertproblems notwendig. In dieser Arbeit wird eine schnelle und speichereffiziente numerische Methode angewendet, die ein periodisches Randwertproblem auf der Mikroskala löst. Die Differentialgleichung des statischen Gleichgewichts wird in eine Integralgleichung vom Lippmann-Schwinger-Typ überführt, und das entsprechende Faltungsintegral mittels schneller Fourier-Transformation gelöst. Mithilfe der Methode wird die effektive Materialantwort von periodischen Mikrostrukturen an makroskopischen Punkten berechnet. Das makroskopische Problem wird mittels der Finite Element Methode (FEM) gelöst.

Zur Berechnung effektiver, nichtlinearer Materialeigenschaften von Verbundwerkstoffen wird ein mikromechanisches Modell erstellt. In einem ersten Schritt werden Konstitutivgesetze der entsprechenden mikroskopischen Materialphasen definiert. Sprödes Versagen des Matrixmaterials wird durch ein isotropes elastisches Schädigungsgesetz beschrieben. Die Fasern werden linear elastisch modelliert. Um duktilen Versagen von thermoplastischen Polymeren zu modellieren, muss ein Konstitutivgesetz verwendet werden, welches die Interaktion von Schädigung und plastischer Deformation beschreiben kann. Verschiedene Ansätze zur Kopplung beider Effekte werden in Kapitel 2 diskutiert. Die Hauptunterschiede zwischen den Ansätzen liegen in der Gestaltung des Stoffgesetzes, das aus der freien Energie abgeleitet wird, der Form des Schädigungskriteriums und der Art der Kopplung und Evolution der internen Variablen. Das Modell von Ju [1989] behandelt die Entwicklung

von Plastizitäts- und Schädigungseffekten separat und ermöglicht somit das Verhalten thermoplastischer Polymere zu reproduzieren. Neben der Definition des physikalischen Verhaltens der einzelnen Materialbestandteile werden unter Verwendung experimentell ermittelter geometrischer Mikrostrukturparameter repräsentative Volumenelemente (RVE) generiert. Auflösung und Größe der RVEs werden getestet und mit experimentellen Daten validiert. Periodische Randbedingungen werden gewählt, da diese zur Berechnung effektiver Eigenschaften periodischer Mikrostrukturen die besten Ergebnisse liefern. Die effektiven Eigenschaften ergeben sich als Volumenmittel über das gesamte Volumenelement. Es wird auf das Energiekriterium von Hill zurückgegriffen um die Konsistenz der aufgebrachten makroskopischen Energie mit der gemittelten mikroskopischen Energie sicher zu stellen.

Die in der Arbeit betrachteten Mikroprobleme werden mittels eines effizienten numerischen Ansatzes gelöst. Dabei wird die Differentialgleichung des statischen Gleichgewichts auf der Mikroskala in eine Integralgleichung vom Lippmann-Schwinger-Typ umformuliert. Die effektive Materialantwort wird mit einem auf der schnellen Fourier-Transformation basierenden Algorithmus berechnet. Die iterative numerische Lösung der Lippmann-Schwinger-Gleichung wird in Kapitel 3 erläutert. Neben Vorzügen hinsichtlich Berechnungszeit und Speicherbedarf erfordert die Methode nicht das Assemblieren und Speichern einer globalen Steifigkeitsmatrix. Daher können größere, und somit realistischere Mikrostrukturen effizient berechnet werden. Weiterhin kann die effektive Materialantwort direkt aus dreidimensionalen Bildaufnahmen periodischer Mikrostrukturen ermittelt werden. Die zeitaufwendige und speicherintensive Netzgenerierung entfällt. Der gesamte Algorithmus ist in einer detaillierten Übersicht dargestellt. Der ursprüngliche Algorithmus von Moulinec und Suquet [1998] erwies sich für die in dieser Arbeit behandelten Probleme hinsichtlich Genauigkeit und numerischer Robustheit als am besten geeignet. Die numerische Konvergenz der Methode wird an einem Testproblem untersucht.

In Kapitel 5.1 werden anhand eines numerischen Beispiels die Mechanismen fortschreitender Schädigung veranschaulicht, die man bei faserverstärkten Kunststoffen beobachten kann. Die Übereinstimmung der Simulation mit Mikroaufnahmen geschädigter Strukturen zeigt, dass die mikromechanischen Schädigungsmechanismen durch die Simulation sehr gut erfasst werden. Des Weiteren wird das Mikrostrukturmodell mit experimentellen Daten eines kurzfaserverstärkten thermoplastischen Materials validiert. Um das Polymermatrix Verhalten zu simulieren wird das Modell von Ju [1989] modifiziert. In einem zyklischen Entlastungsversuch gemessene tabellarische Werte werden linear interpoliert. Zur Simulation des Verbundverhaltens wird ein mikroskopisches Modell mit Geometriedaten erzeugt, die aus einer mikroskopischen Bildanalyse stammen. Für die elastischen Parameter der Glasfasern werden Standardwerte gewählt. Größe und Auflösung der RVEs werden anhand gemessener anisotroper Steifigkeitswerte validiert. Ein Vergleich mit experimentellen Ergebnissen zeigt, dass die effektive lineare und nichtlineare Antwort des Verbundes präzise vorhergesagt werden kann. Die effektive Materialantwort folgt direkt aus

dem Verhalten der Materialphasen und der Geometrie des mikrostrukturellen Modells. Mit Hilfe dieses effizienten numerischen mikromechanischen Ansatzes können sogar Entlastungsversuche in unterschiedlichen Lastrichtungen korrekt reproduziert werden. Mittels analytischer oder semi-analytischer Homogenisierungsmethoden ist es kaum möglich, diese experimentellen Ergebnisse zu reproduzieren, gerade wenn nichtproportionale Lastpfade in Betracht gezogen werden.

Zur Untersuchung des makroskopischen Verhaltens nichtlinearer Verbundwerkstoffe wurde eine Multiskalenmethode entwickelt. Die numerischen Methoden, die zur Lösung der Randwertprobleme auf den betrachteten Skalen eingesetzt werden, sind in einem FE^2 -ähnlichen Ansatz gekoppelt. Die Konstitutivgleichung der Makroskala wird durch ein assoziiertes Randwertproblem auf der Mikroskala ersetzt. Aufgrund steigender Rechenzeiten, die mit der Verwendung eines voll gekoppelten Ansatzes entstehen, wird die entwickelte effiziente mikroskopische Methode verwendet um das Mikroproblem zu lösen. Die Verwendung der FEM zur Lösung des Makroproblems ermöglicht es, beliebig geformte makroskopische Bauteile in herkömmlicher Weise zu behandeln. Das eigenständige mikroskopische Problem kann leicht in kommerzielle FEM-Codes implementiert werden. Die Technik der Skalenkopplung und die Berechnung des makroskopischen tangentialen Steifigkeitstensors mittels numerischer Störung werden in Kapitel 4 erläutert. Details über die algorithmische Implementierung und das Speichern bzw. die Evolution der internen Variablen sind beschrieben. Mittels eines numerischen Beispiels werden die Größe der numerischen Störung und deren Einfluss auf das Konvergenzverhalten des Makroproblems analysiert. Optimale Ergebnisse werden mit Perturbationsdehnungen zwischen 10^{-7} und 10^{-5} erzielt. Des Weiteren wird der Startpunkt makroskopischen Versagens in einer numerischen Analyse untersucht. Mikroskopisches Versagen führt zum Verlust der Elliptizität der makroskopischen Differentialgleichung, sobald die kleinsten Eigenwerte des mit der effektiven Steifigkeitsmatrix assoziierten Akustiktensors Null oder sogar negativ werden. Anhand eines numerischen Beispiels wird der Startpunkt des Versagens durch eine Studie am akustischen Tensor detektiert, der aus dem homogenisierten Steifigkeitstensor berechnet wird. Mit der entwickelten Methode kann der Versagensbeginn beliebiger Mikrostrukturen effizient bestimmt werden.

Abschließend sind in Kapitel 5.2 einige Multiskalenrechnungen realistischer Strukturen dargestellt. Der mikromechanische Schädigungsfortschritt wird zur Makroskala transportiert und resultiert in einem Verlust makroskopischer Steifigkeit sowie einer Umverteilung der makroskopischen Spannungen. Die Multiskalenmethode erlaubt es, nichtlineare Materialeffekte direkt auf einer feineren Skala zu erfassen. Somit wird die exakte Materialantwort unter nichtproportionalen multiaxialen Lasten für beliebig komplexe Mikrostrukturen erhalten. Die benötigten Parameter der Materialphasen können direkt aus physikalischen Messungen bestimmt werden. Eine Untersuchung des Newton-Algorithmus auf der Makroskala zeigt quadratische Konvergenz für alle Lastschritte. Zur Reduzierung der Rechenzeiten werden die entkoppelten RVE-Rechnungen unter Verwendung paralleler Algorithmen simultan ausgeführt.

Abstract

Fiber reinforced composite materials play a crucial role in future light-weight applications, especially in current developments in the field of electro mobility. At the same time, composites possess a highly complex material behavior. Since experimental tests are expensive and time consuming, advanced simulation techniques are necessary to use these composite materials efficiently. In particular, modeling progressive damage and failure of composite materials presents a challenging task. Conventional macro mechanical methods are in many cases not sufficient to predict the appropriate mechanical material response. Composite failure occurs as a result of complex microstructural damage mechanisms. These effects have to be taken into account in order to predict the material behavior correctly. Hence, several multiscale modeling and simulation techniques were developed to incorporate the micromechanical material behavior. Multiscale methods, based on analytical closed form estimates or semi-analytical interpolation methods, are only applicable to simple reinforcement shapes and are not always suitable when complex macroscopic loads are applied. In these cases coupled full-field simulations must be resorted to. This is performed by modeling the microstructural constituents explicitly and the resultant material response is obtained in a coupled simulation. However, the coupled simulation results in an increase in the overall number of degrees of freedom, and so an efficient solution of the microscopic boundary value problem (BVP) is necessary. In this work, a fast and memory efficient numerical method is applied to solve a periodic BVP at the microscale. The governing differential equation is transformed into an integral equation of Lippmann-Schwinger type and the convolution is solved using the fast Fourier transformation (FFT). Using this method, the overall material response at a macroscopic point is computed, and the finite element method (FEM) is applied for solving the macroscopic problem.

In order to compute the effective material properties of nonlinear composite materials, a microscopic model is generated. In the first step, suitable constitutive laws for the microscopic constituents are defined. Brittle damage of fiber reinforced materials is modeled by an elastic isotropic damage law for the matrix material. The reinforcements are assumed to behave linear elastic. For modeling ductile damage of thermoplastic polymer materials a constitutive law describing the interaction between the physical effects of damage and plastic deformation is necessary. Different approaches for coupling both these effects are discussed in Chapter 2. The model of Ju [1989] treats the evolution of plasticity and damage effects in a separate way which enables one to reproduce the material behavior of thermoplastic polymers. Besides the definition of the physical behavior of the particular material phases, representative volume elements (RVE) are generated using measured geometrical microstructural parameters. Size and resolution of the RVEs are tested and validated with experimental data. Periodic boundary conditions are chosen, since these are the most accurate for computing effective properties of periodic microstructures.

Effective homogenized quantities are calculated as volume averages over the entire unit cell. Hill's energy criterion is resorted to ensure the consistency of the applied macroscopic energy with the resulting averaged microscopic energy.

The homogenization problems are solved using an efficient numerical framework. The governing differential equation that describes the static equilibrium at the microscopic level is reformulated into an integral equation of Lippmann-Schwinger type and the overall material response is computed by an efficient numerical algorithm based on fast Fourier transforms. Details regarding the iterative numerical solution of the Lippmann-Schwinger equation are discussed in Chapter 3. In addition to its benefits in terms of memory consumption and computational time, the method does not require the assembly and storage of a global stiffness matrix. Thus, larger and more realistic microstructures can be computed efficiently. Furthermore, homogenized quantities can be directly computed from three dimensional micro images. The time and memory consuming mesh generation is omitted. A detailed description of the entire algorithm of the numerical method is given. In terms of accuracy and numerical robustness, the original algorithm of Moulinec and Suquet [1998] was found to be appropriate for the applications treated in this work. The numerical convergence of the method is investigated on a test problem.

In Chapter 5.1 a comparison of microscans of failed structures with simulated results is performed and shows that the mechanisms of growing damage in short fiber reinforced composites are captured very well by the numerical simulation. Furthermore, the microstructural model is validated with experimental data of a short fiber reinforced thermoplastic material. In order to reproduce the matrix material behavior, the modified coupled constitutive law of Ju [1989] is used. For simulating the effective composite response, a microstructural model is generated with geometrical data obtained from micrograph analysis. Standard values for the elastic parameters of the glass fibers are chosen. The size and resolution of the RVE are validated with measured anisotropic stiffness values. Comparison with experimental results shows that the effective linear and nonlinear response of the composite is predicted precisely. The effective response follows directly from the material laws of the constituents and the geometry of the microstructural model. The approach can also reproduce results of unloading tests in different loading directions. Using analytical or semi-analytical homogenization approaches, it would be hard to reproduce these results, in particular when non proportional load paths are taken into consideration.

For the investigation of the macroscopic damage behavior a multiscale approach has been established. The numerical methods, which are used to solve the boundary value problems on the two considered spatial scales, are coupled by a procedure similar to the FE² approach. The constitutive equation at the coarse scale is replaced by an associated boundary value problem at the microscopic level. Due to the increased computational costs involved with the application of a fully coupled multiscale framework, the proposed efficient microscopic homogenization method is used

to compute the microscale BVP. Solving the macroscale problem by FEM enables us to deal with arbitrary shaped macroscopic components in a standard manner. The decoupled microscopic problem can easily be implemented as a material routine in commercial FEM codes. The scale coupling technique and the computation of the macroscopic tangential stiffness tensor by numerical perturbation is shown in Chapter 4. Details of the algorithmic implementation and the storage and evolution of internal variables are assessed. In a numerical example, the size of the perturbation strain and its influence on the convergence behavior of the Newton algorithm at the macroscale is investigated. Optimal results are obtained by choosing the perturbation strain in a range between 10^{-5} and 10^{-7} . Furthermore, the onset of macroscopic failure is studied using the effective stiffness matrix. Microscopic failure leads to the loss of ellipticity of the governing macroscopic differential equation, when the eigenvalues of the associated acoustic tensor become zero or even negative. By means of a numerical example, the failure onset is detected by an analysis of the acoustic tensor of the current homogenized tangent stiffness tensor. Within the established procedure, failure of arbitrary microstructures can be detected efficiently.

Finally, in Chapter 5.2, some multiscale examples of realistic structures are shown. Growing damage among the material constituents at the microscale results in a macroscopic reduction of stiffness and a redistribution of macroscopic stresses. The multiscale approach enables us to capture the nonlinear material effects directly at a finer length scale. Hence, within this method, the correct physical response under complex non-proportional, multiaxial loading conditions is obtained for arbitrary microstructures. The required parameters of the material phases can be measured directly in physical experiments. An investigation of the Newton algorithm at the macroscale shows quadratic convergence for all load steps. In order to reduce the computational time, the decoupled RVE computations are solved simultaneously using parallel algorithms.

Contents

1	Introduction	1
1.1	Motivation and State of the Art	1
1.2	Scope and Outline	5
2	Continuum Mechanics	7
2.1	Kinematics of Deformations	7
2.2	Balance Equations	8
2.3	Constitutive Equations	10
2.3.1	Continuum Damage Mechanics	10
2.3.2	Elasticity Coupled with Damage	12
2.3.3	Elastoplasticity Coupled with Damage	16
2.4	Micromechanics and Homogenization	23
2.4.1	Basic Concept and Length Scales	23
2.4.2	Bounds and Estimates	25
2.4.3	Analytical Homogenization Techniques	26
2.4.4	Semi-analytical Homogenization Techniques	27
2.4.5	Computational Homogenization Techniques	29
3	Numerical Methods	35
3.1	Finite Element Method	35
3.1.1	Weak Formulation of the Equilibrium Equations	35
3.1.2	Linearized Equilibrium Equations	37
3.1.3	Spatial Discretization	38
3.1.4	Iterative Solution Procedure	40
3.2	Lippmann-Schwinger Equ. and Fast Fourier Trans.	41
3.2.1	Periodic Strain Field and Local Boundary Value Problem	41
3.2.2	Lippmann-Schwinger Equation and Equivalent Boundary Value Problem	43
3.2.3	Green's Operator in Bounded Domains	47
3.2.4	Lippmann-Schwinger Equation in Fourier Space	49
3.2.5	Voxel Discretization and Fast Fourier Transformation	52
3.2.6	Numerical Solution Scheme and Discrete Algorithm	53
4	Multiscale Method	61
4.1	Iterative Scale Coupling	61
4.2	Boundary Value Problems at the Spatial Scales	62
4.3	Consist. Macroscopic Tangent and Num. Algorithm	64
4.4	Onset of Macroscopic Failure	73

5	Numerical Examples	77
5.1	Microscale Computations	77
5.1.1	Convergence Microscale Model	77
5.1.2	Microscopic Failure Mechanisms in Fiber Reinforced Composites	78
5.1.3	Experimental Validation with a Short Fiber Reinforced Thermoplastic Material	81
5.2	Multiscale Computations	93
5.2.1	Strip with a Hole and Spherical Inclusion	93
5.2.2	Strip with a Hole and Fiber Composite	95
5.2.3	L-Profile and Fiber Composite	96
6	Conclusion and Outlook	99
6.1	Conclusion and Main Results	99
6.2	Outlook and Future Work	102
	Bibliography	105

Chapter 1

Introduction

1.1 Motivation and State of the Art

Recent research activities in aerospace and automotive industries are focused on developing and applying new light-weight materials in order to reduce vehicle weight and thus decrease fuel consumption and carbon dioxide emissions. Fiber reinforced composite materials play a crucial role in future industrial applications, especially in the context of electro mobility. Besides their outstanding mechanical properties in terms of strength and stiffness related to their weight, fiber reinforced composite materials possess a highly complex material behavior. As experimental tests are expensive and time consuming, advanced simulation techniques are necessary in order to use these composite materials efficiently. In particular, modeling failure and progressive damage of composite materials presents a challenging task in current research activities. Composite failure occurs as a result of a variety of complex microstructural damage mechanisms, such as matrix damage, fiber pull out and fiber breakage. These effects have to be taken into account in order to predict the material behavior correctly.

In many practical applications, phenomenological macroscale models are used for failure investigations of composite materials, for instance in the work of Maimí et al. [2007] and Pinho et al. [2012]. These models assume homogeneous material behavior and are usually based on macroscopic failure criteria, like those proposed by Puck and Schürmann [1998] and Cuntze [2006]. The material parameters have to be determined in an extensive identification process for each particular material structure and loading condition. Physical phenomena occurring on a finer length scale are not considered.

A more accurate approach is to capture nonlinear material effects directly at a finer length scale within a multiscale approach. Involved with an increase of the overall degrees of freedom coming along with the use of a multiscale method recent modeling and simulation techniques were developed to limit the computational effort to an acceptable extent, see Kanouté et al. [2009] and Zohdi and Wriggers [2008] for an overview.

In this context, analytical homogenization methods were established to compute overall effective material properties from heterogeneous microstructures. So called mean field approaches are based on Eshelby's inclusion theory [Eshelby, 1957] and consider the geometrical shape of the micromechanical material structure by means of analytical approximations like the Mori-Tanaka model [Mori and Tanaka, 1973].

In this regard, reinforcements, such as fibers, are considered as ellipsoidal inclusions in a surrounding matrix material. The elastic fields around these inclusions are obtained as closed form estimates which are only accessible for certain inclusion shapes [Klusemann et al., 2012]. Hence, the method is restricted to simple microstructures containing particles that are locally uniformly distributed in terms of their size, orientation and volume density. Furthermore, the volume fraction of the particles is restricted and interactions between separated particles are only captured to a limited degree. This is an important limitation for the simulation of the evolution of micro cracks. Progressive damage is usually modeled using empirical failure criteria, for example, the Tsai-Wu, Tsai-Hill, maximum stress or strain criterion, which are based on the work of Tsai and Wu [1971] and Hill [1998].

To improve the accuracy of a micromechanical model, the microstructural constituents are modeled explicitly on the scale of interest. However, the detailed resolution of the microstructural constituents leads to a fine discretization of the computational model and thus to large algebraic systems with many degrees of freedom. Despite increasing computational power, simulations of macroscopic components using explicitly modeled realistic microstructures cannot be accomplished with reasonable computational times today. In this context, semi-analytical methods were proposed. The key idea of these is to utilize the benefits of numerical homogenization techniques in terms of their accuracy and their ability to deal with sophisticated reinforcement shapes while retaining the efficiency of analytical methods. In this regard, the generalized method of cells (see [Aboudi, 1996]) or the transformation field analysis (TFA) proposed by Dvorak [1992] were developed. Moreover, Michel and Suquet [2003] introduced the so called nonuniform TFA. The latter method aims to reconstruct local inelastic fields from a finite number of precomputed unit cell problems. Instead of forming effective macroscopic constitutive equations, separate material models are defined for the explicitly modeled microstructural constituents. Besides its numerical efficiency, the nonuniform TFA method has some limitations. The choice of the precomputed unit cell problems depends in general on the type of macroscopic loading. In particular, when strongly non-proportional cyclic and/or temperature dependent loads are applied the method could hardly predict any macroscopic loading situation.

The following numerical example shows the dependence of a microstructural response on a particular loading history. Periodic Neumann boundary conditions are used to apply a combined load in the x - and y -directions on a microstructural sample containing a single elliptical inclusion. As shown in Figure 1.1a, the load is applied first in the x -direction and, after a small decrease of the x -load, an additional load in y -direction is applied (load path 1). Applying the loads in the opposite order is referred to as load path 2, and is illustrated in Figure 1.1b. The resulting damage fields are shown in Figure 1.2. The difference between the two fields is obvious. In the local field resulting from load path 1 (Figure 1.2a) high damage values around the tips of the ellipsoid can be observed. While the load order according to load

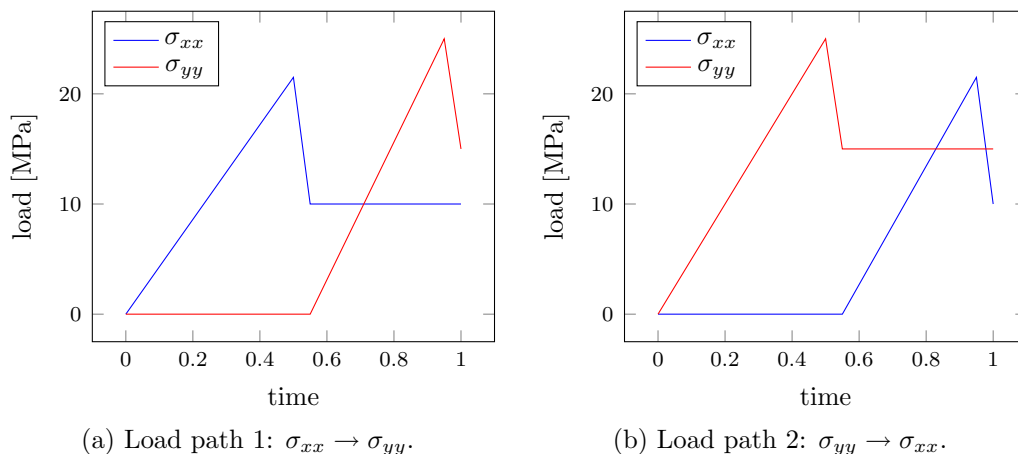


Figure 1.1: Different ordering of loads applied on the microstructure.

path 1 would result in global failure of the structure (see Figure 1.2a), the reverse order of the applied loads according to load path 2 reduces the critical damage zones significantly (see Figure 1.2b). Applying the critical x -load after the load in y -direction according to load path 2 attenuates the influence of the critical x -load (see Figure 1.2b).

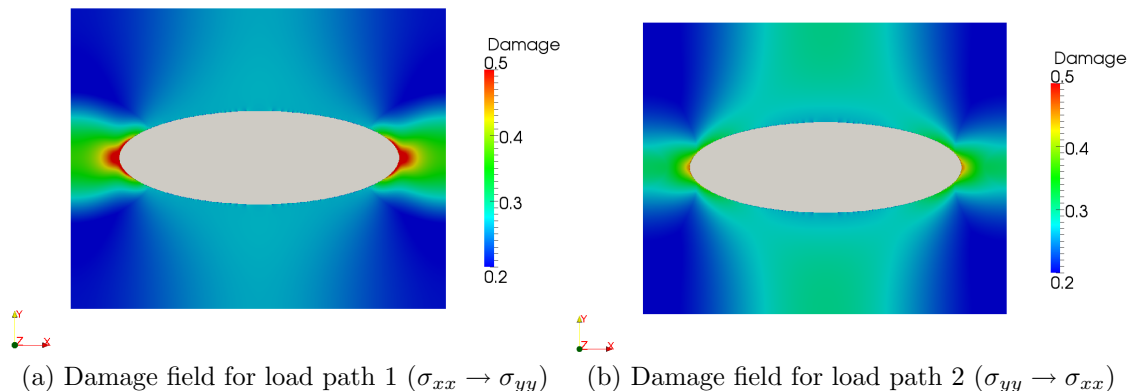


Figure 1.2: Resulting local damage fields for different load history. The loads according to Figure 1.1 are applied using periodic Neumann boundary conditions.

The example illustrates the influence of the proper loading history on the resulting local fields and thus, on the overall global response.

In order to overcome the shortcomings related to analytical and semi-analytical methods, one has to resort to coupled direct or full-field simulations. Therein, the microstructural constituents are modeled explicitly and the resultant material response is obtained in a coupled simulation. Hence, any arbitrary microstructure can be considered. In each load step the particular current macroscopic load is applied on the microstructure and thus, any complex non-proportional, multiaxial loading condition can be captured. The response of the actual load state is consequently based on genuine physical effects. Moreover, simple (isotropic) constitutive laws

can be used to define the material behavior of the microstructural constituents and the required parameters can be measured directly in physical experiments. Over the last decade, several fully coupled numerical multiscale modeling and simulation techniques have been developed. One well-known method is the FE^2 approach introduced by Feyel and Chaboche [2000] and Smit et al. [1998]. This numerical method considers different length scales of the material structure by means of a fully coupled micro-macro simulation process. The scales are solved separately and every macroscopic point is equipped with a certain microstructure, which describes the material behavior at this spatial point. The constitutive equation at the coarse scale is replaced by an associated microscopic boundary value problem (BVP). Information passes in both directions and a mutual exchange between both scales takes place.

Due to the increased computational costs involved with the application of a fully coupled multiscale framework, an efficient solution of the microscopic BVP is necessary. In this work, an alternative numerical method is applied which uses the fast Fourier transformation (FFT) to solve an equivalent periodic BVP on the microscale. This periodic BVP is reformulated in an integral equation of Lippmann-Schwinger type, as proposed by Kröner [1977], Zeller and Dederichs [1973]. Neumann series is used to solve the integral equation iteratively. An efficient FFT-based numerical algorithm was introduced by Moulinec and Suquet [1998]. The method is applicable on regular periodic unit cell structures and is used in this work to compute the overall material response on a certain macroscopic point. Advantages of the numerical method are its efficiency in terms of memory consumption and computational time. Furthermore, the unit cell computations are carried out on regular voxel grids. Therefore, the method can be applied directly, to compute homogenized quantities on three dimensional images like tomographies without using any complicated mesh generation. The fine scale problem can easily be integrated in a standard finite element framework which is used to solve the macroscopic BVP. Hence, regarding the incorporation of boundary conditions and the spatial discretization arbitrary shaped macroscopic components can be treated in a standard finite element manner.

A more detailed overview of the current state of research and the fundamental contributions related to the topics of this work are given in the particular chapters of this thesis.

1.2 Scope and Outline

The scope of this thesis is to develop an efficient computational multiscale method for modeling nonlinear material effects in composite materials in order to precisely predict component failure for arbitrary external loading conditions. A particular focus is on the modeling of progressive damage and plasticity in fiber reinforced polymers and its related microstructural mechanisms.

The thesis is composed of six chapters. Chapter 2 covers the fundamentals of continuum mechanics and the constitutive equations regarding continuum damage mechanics and the coupling to plasticity. Furthermore, the theory of homogenization and micromechanics, its basic concepts, analytical bounds, and computational modeling approaches are briefly discussed.

The numerical methods which are used to solve the boundary value problems related to the spatial scales considered in this work are outlined in Chapter 3. In addition to the finite element method, which is associated to the macroscopic problem, the microscopic homogenization method is described. In this context, the Lippmann-Schwinger equation in elasticity and its iterative solution using fast Fourier transforms to compute the convolution with a Green's function are discussed.

The coupling technique of the geometrical scales by combining the two numerical methods is addressed in Chapter 4. The numerical homogenization process including the computation of the macroscopic tangent and the evolution of internal variables at the microscale are explained. The onset of macroscopic failure is demonstrated by an illustrative numerical example.

In the first part of Chapter 5, some numerical examples of microscale computations are given. The microscopic damage mechanisms are investigated, and simulated results are validated with experimental data for short fiber reinforced thermoplastic materials. The second part of this chapter illustrates the macroscopic convergence behavior of the numerical method by specific scale coupling problems.

Finally, Chapter 6 summarizes the results and gives an outlook to future work.

Chapter 2

Continuum Mechanics

Continuum mechanics is known as the branch of mechanics that aims at describing the mechanical relations of continuously distributed matter. This chapter deals with the basic concepts which serve as the underlying physical and mathematical theory of this work. For more detailed information in the field and some nonlinear extensions the reader is referred to the textbooks of Bonet and Wood [2008] and Holzapfel [2000].

2.1 Kinematics of Deformations

The kinematic relations describe the motion and the deformation of a body. According to Figure 2.1 the original position of the material points in the reference configuration Ω_0 at time $t = 0$ is described with the position vector \mathbf{X} . For the specification of the material points at time t in the current configuration Ω_t the vector \mathbf{x} is introduced.

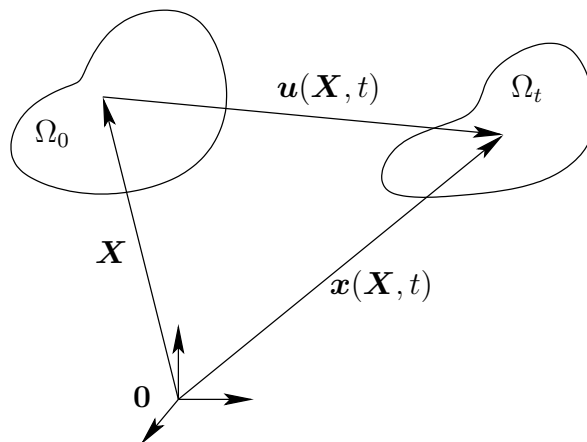


Figure 2.1: Motion of the body Ω .

The motion of the body is given by a nonlinear deformation map

$$\mathbf{x} = \boldsymbol{\varphi}(\mathbf{X}, t) . \quad (2.1)$$

The displacement vector \mathbf{u} is defined by the difference of the position vectors $\mathbf{x} = \mathbf{x}(\mathbf{X})$ and \mathbf{X} , i.e.

$$\mathbf{u} = \mathbf{x} - \mathbf{X} . \quad (2.2)$$

Furthermore, the deformation gradient \mathbf{F}

$$\mathbf{F} = \text{Grad } \boldsymbol{\varphi}(\mathbf{X}, t) = \frac{\partial \mathbf{x}}{\partial \mathbf{X}} \quad (2.3)$$

and its closely related displacement gradient \mathbf{H}

$$\mathbf{H} = \text{Grad } \mathbf{u} = \frac{\partial \mathbf{u}}{\partial \mathbf{X}} = \frac{\partial \mathbf{x}}{\partial \mathbf{X}} - \frac{\partial \mathbf{X}}{\partial \mathbf{X}} = \mathbf{F} - \mathbf{I} \quad (2.4)$$

are introduced. The symbol \mathbf{I} in (2.4) represents the second order identity tensor. To obtain a suitable measurement for the deformation of the body, the distances between the material points in the reference and the current configuration are considered. Therefore the squares of the lengths of a line element in the respective configuration are introduced

$$ds^2 = d\mathbf{x} \cdot d\mathbf{x} = (\mathbf{H} d\mathbf{X} + d\mathbf{X}) \cdot (\mathbf{H} d\mathbf{X} + d\mathbf{X}) \quad (2.5)$$

$$dS^2 = d\mathbf{X} \cdot d\mathbf{X}, \quad (2.6)$$

and the difference between the lengths of these line elements

$$ds^2 - dS^2 = (\mathbf{H} d\mathbf{X} + d\mathbf{X}) \cdot (\mathbf{H} d\mathbf{X} + d\mathbf{X}) - d\mathbf{X} \cdot d\mathbf{X} \quad (2.7)$$

$$= d\mathbf{X} \cdot [(\mathbf{H} + \mathbf{H}^T + \mathbf{H}^T \mathbf{H}) d\mathbf{X}] = d\mathbf{X} \cdot [2\mathbf{E} d\mathbf{X}], \quad (2.8)$$

gives the definition of the Green-Lagrange strain tensor \mathbf{E}

$$\mathbf{E} = \mathbf{H} + \mathbf{H}^T + \mathbf{H}^T \mathbf{H} = \frac{1}{2} \left(\frac{\partial \mathbf{u}}{\partial \mathbf{X}} + \frac{\partial \mathbf{u}}{\partial \mathbf{X}} + \frac{\partial \mathbf{u}}{\partial \mathbf{X}} \frac{\partial \mathbf{u}}{\partial \mathbf{X}} \right). \quad (2.9)$$

For infinitesimal small displacement gradients ($|\partial \mathbf{u} / \partial \mathbf{X}| \ll 1$) the derivative with respect to the reference coordinates \mathbf{X} is replaced by the derivative with respect to the current coordinates \mathbf{x} and the terms of higher order in (2.9) are neglected. The resulting linearized strain tensor $\boldsymbol{\varepsilon}$ is given by the symmetric part of the displacement gradient

$$\boldsymbol{\varepsilon} = \frac{1}{2} (\text{grad } \mathbf{u} + (\text{grad } \mathbf{u})^T) = \text{grad}_s \mathbf{u}. \quad (2.10)$$

This work is restricted to infinitesimal small deformations states for which the linear deformation theory can be applied. This means that no explicit distinction between the two configurations Ω_0 and Ω_t is necessary. The stress and strain measurements used in this work are related to the same single configuration Ω .

2.2 Balance Equations

The resulting deformation of a solid body under prescribed external load can be described by the static equilibrium in differential form. To derive these differential static equilibrium conditions, as illustrated in Figure 2.2, a deformable body defined

by a bounded domain Ω with Lipschitz boundary $\partial\Omega$ is considered.

Remark: A function $f(x)$ is Lipschitz continuous if there exists a constant L , with $|f(x) - f(y)| \leq L \cdot |x - y|$. Assuming Lipschitz continuous boundary functions allows considering not only smooth but more realistic shaped domains.

The body is deformed under the action of volume forces $\mathbf{f} = \rho\mathbf{b}$ per unit volume and surface forces \mathbf{t} acting on the area dA . Due to the limitation to static loads,

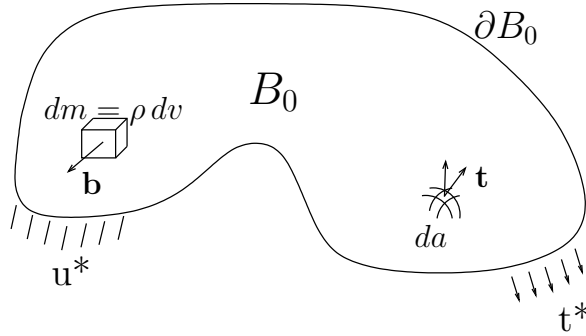


Figure 2.2: Boundary value problem with arbitrary boundary conditions.

inertia forces are neglected and the translational equilibrium equation in terms of the sum of all forces gives

$$\int_{\partial\Omega} \mathbf{t} dA + \int_{\Omega} \mathbf{f} dV = \mathbf{0}. \quad (2.11)$$

Applying Cauchy's theorem $\mathbf{t} = \boldsymbol{\sigma}^T \mathbf{n}$ which introduces the Cauchy stress tensor $\boldsymbol{\sigma}$ that maps the outward normal vector \mathbf{n} to the respective surface traction vector \mathbf{t} one obtains for smooth boundaries $\delta\Omega$ ¹

$$\int_{\partial\Omega} \boldsymbol{\sigma} \mathbf{n} dA + \int_{\Omega} \mathbf{f} dV = \mathbf{0}. \quad (2.12)$$

The surface integral of the first term in (2.12) can be transformed into a volume integral using Gauss' theorem

$$\int_{\Omega} (\text{div } \boldsymbol{\sigma} + \mathbf{f}) dV = \mathbf{0}. \quad (2.13)$$

The above equation is valid in any closed region of the body so that the local form reads

$$\text{div } \boldsymbol{\sigma} + \mathbf{f} = \mathbf{0}. \quad (2.14)$$

¹The outward normal vector \mathbf{n} is defined uniquely for smooth boundaries, only.

The symmetry of the Cauchy stress tensor

$$\boldsymbol{\sigma} = \boldsymbol{\sigma}^T \quad (2.15)$$

follows from the rotational equilibrium equation

$$\int_{\Omega} \mathbf{x} \times \mathbf{f} \, dV + \int_{\partial\Omega} \mathbf{x} \times \mathbf{t} \, dA = \mathbf{0} . \quad (2.16)$$

Equation (2.13) represents the strong form of the static equilibrium equations which describe the mechanical state of a solid body in the presence of volume forces. For defining a solvable boundary value problem appropriate boundary conditions have to be applied and further, suitable constitutive equations have to be defined. The latter describe the mechanical material behavior and connect the deformation state of the body with the corresponding stress field.

2.3 Constitutive Equations

This section refers to the basic concept of continuum damage mechanics. The coupling of damage mechanics with linear elastic material behavior and elasto-plastic behavior is described.

2.3.1 Continuum Damage Mechanics

Damage mechanics is considered as the theory that describes the deterioration process of matter due to growing micro cracks or micro voids. In contrast to fracture mechanics that is related to macroscopic discontinuous failure mechanisms, like crack development and crack branching, damage mechanics is focused on mechanisms occurring on the micro- and mesoscale in the framework of continuous deformable bodies. Hence, damage mechanics can be regarded as the theory for describing deterioration of matter until the onset of macroscopic failure. Two approaches are mainly used to model the effect of material degradation due to growing micro defects. The first one considers the macroscopic damage behavior with nucleation and growth of microscopic voids. This approach was mainly developed by Gurson [1977], Rousselier [1981] and Tvergaard and Needleman [1984]. The second approach, the Continuum Damage Mechanics (CDM), can be classified in a more phenomenological way. The considered domain is regarded on the continuum's level and microscopic degradation is described by internal variables which can be determined in physical experiments. The first approach is not object of this work and thus, only the second one will be explained more in detail in the following sections. For a comprehensive review in the field of damage mechanics see, for instance, the work of Krajcinovic [1989, 1996], more recently Lemaitre and Desmorat [2005], Besson et al. [2010] and Murakami [2012]. Concerning the numerical implementation of these kinds of models see de Souza Neto et al. [2011] or Simo and Ju [1987b].

In the context of CDM, Kachanov [1958, 1986] introduced an internal variable d ranging from 0 to 1. While $d = 0$ represents the undamaged state, $d = 1$ describes the status of completely failed material. The parameter d describes the relation between the damaged area A_d and the undamaged area A_0

$$d = \frac{A_d}{A_0} \quad \text{in } [0, 1] . \quad (2.17)$$

In addition, an effective undamaged reference material with cross section $A_0 - A_d$ according to Figure 2.3 is defined. The reference material is homogeneous and allows for the formulation of isotropic constitutive relations in an effective manner.

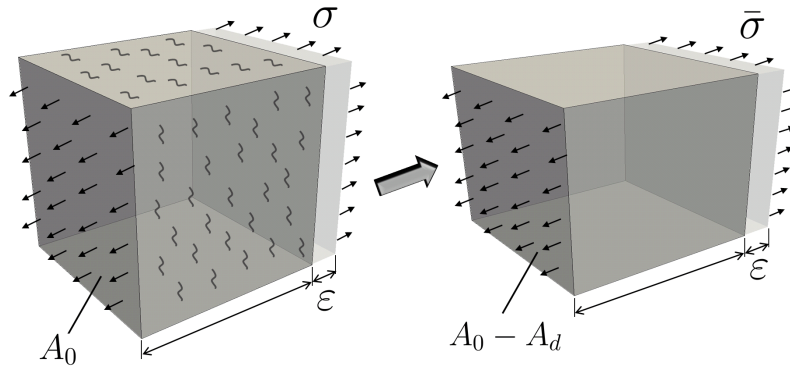


Figure 2.3: Concept of strain equivalence between real damaged (left) and effective undamaged reference material (right).

In this regard, Rabotnov et al. [1969] introduced the concept of effective stresses which sets the nominal stresses in relation to the (higher) effective stresses which would act in an undamaged material. Models using this concept are either based on the principle of strain equivalence (Chaboche [1977], Ju [1989]) or the principle of equivalent strain energy (Cordebois and Sidoroff [1982], Hansen and Schreyer [1994]). The concept of strain equivalence states that the effective strain $\bar{\epsilon}$ equals the real strain ϵ . From the balance of forces acting on both areas we obtain

$$\bar{\sigma}(A_0 - A_d) = \sigma A_0 \quad \text{with} \quad \bar{\sigma} = \frac{\sigma}{1 - d} . \quad (2.18)$$

The scalar variable d is used for characterizing isotropic damage processes. Considering materials with pre-existing directions in which damage takes place preferentially, an anisotropic damage model is necessary. In this regard, second or fourth order damage tensors are introduced.

Murakami and Ohno [1982] proposed a second order damage tensor \mathbf{D} to describe directional dependent damage effects. The effective stress is given by

$$\bar{\sigma} = \frac{1}{2} \left((1 - \mathbf{D})^{-1} \sigma + \sigma (1 - \mathbf{D})^{-1} \right) . \quad (2.19)$$

A more general framework is obtained from the effective stress concept directly. Chaboche [1979] introduced a fourth order damage effect tensor \mathbf{M} to describe the damage induced anisotropy accurately (see also Cordebois and Sidoroff [1982], Simo and Ju [1989]). The tensor \mathbf{M} transforms the stress in the effective space

$$\bar{\boldsymbol{\sigma}} = \mathbf{M}^{-1} : \boldsymbol{\sigma} . \quad (2.20)$$

The above expression can be written similar to (2.18) as

$$\mathbf{M} = \mathbb{I} - \mathbf{D} , \quad (2.21)$$

where \mathbb{I} is the fourth order identity tensor and \mathbf{D} the fourth order damage tensor that describes the state of damage. For the isotropic damage case \mathbf{M} reduces to

$$\mathbf{M} = (1 - d)\mathbb{I} . \quad (2.22)$$

Later, among others, Chaboche [1988], Lemaitre [1984], Lemaitre and Lippmann [1996] and Krajcinovic [1985] formulated the theory of continuum damage mechanics in the context of a thermodynamical framework for irreversible processes.

2.3.2 Elasticity Coupled with Damage

In this work a strain based continuum damage model according to Ju [1989] and Simo and Ju [1987a], respectively, is used to describe the elastic deterioration process of composite materials. The constitutive equation is derived from a thermodynamic state potential, the Helmholtz free energy

$$\psi = \frac{1}{2}(1 - d) \boldsymbol{\varepsilon} : \mathbf{c}_e : \boldsymbol{\varepsilon} , \quad (2.23)$$

where \mathbf{c}_e is the isotropic elasticity tensor. Furthermore, the stresses $\boldsymbol{\sigma}$ can be derived subsequently as the thermodynamical conjugated force related to the strains $\boldsymbol{\varepsilon}$. The Cauchy stress is derived by the following equation:

$$\boldsymbol{\sigma} = \frac{\partial \psi}{\partial \boldsymbol{\varepsilon}} = (1 - d) \mathbf{c}_e : \boldsymbol{\varepsilon} . \quad (2.24)$$

The specific strain energy is the thermodynamic force Y associated with the internal state variable d

$$Y = -\frac{\partial \psi}{\partial d} = \frac{1}{2} \boldsymbol{\varepsilon} : \mathbf{c}_e : \boldsymbol{\varepsilon} . \quad (2.25)$$

For the isothermal case the second law of thermodynamics can be expressed in terms of the Clausius-Duhem inequality

$$\mathcal{D} = \mathcal{P} - \dot{\psi} \geq 0 , \quad (2.26)$$

with the energy dissipation \mathcal{D} and the rate of mechanical work

$$\mathcal{P} = \boldsymbol{\sigma} : \dot{\boldsymbol{\epsilon}} . \quad (2.27)$$

Equation (2.26) claims that the rate of mechanical work \mathcal{P} is always greater than the change of energy $\dot{\psi}$ and thus, no negative energy dissipation is allowed. With the absence of further dissipative processes one obtains the Clausius-Duhem inequality in the following form:

$$\begin{aligned} \mathcal{D} &= \boldsymbol{\sigma} : \dot{\boldsymbol{\epsilon}} - \left(\frac{\partial \psi}{\partial \boldsymbol{\epsilon}} \dot{\boldsymbol{\epsilon}} + \frac{\partial \psi}{\partial d} \dot{d} \right) \geq 0 , \\ \mathcal{D} &= \underbrace{\left(\boldsymbol{\sigma} - \frac{\partial \psi}{\partial \boldsymbol{\epsilon}} \right)}_0 \dot{\boldsymbol{\epsilon}} - \frac{\partial \psi}{\partial d} \dot{d} \geq 0 , \\ \mathcal{D} &= Y \dot{d} \geq 0 . \end{aligned} \quad (2.28)$$

Thus, according to (2.29) the dissipated energy is defined by the product of the strain energy and the rate of the growing damage variable. A damage criterion f is introduced describing the state of damage, which is in the case of growing damage expressed by a monotonic function $\phi(Y)$

$$f(Y, d) = \phi(Y) - d \leq 0 \quad \begin{cases} f < 0 & \text{elastic} \\ f = 0 & \text{damage} . \end{cases} \quad (2.29)$$

According to Kuhl [2000] and Simo and Ju [1987a] the above damage criterion function f and the dissipation inequality (2.28) in combination with the principle of maximum dissipation

$$\mathcal{D} = Y \dot{d} \rightarrow \max , \quad (2.30)$$

leads to a constrained optimization problem subject to the constraint $f = 0$. Introducing the Lagrangian multiplier $\dot{\lambda} \geq 0$ the constrained optimization problem is transformed into a saddle point problem described by the following Lagrangian functional:

$$\mathcal{L} = -\mathcal{D} + \dot{\lambda} f = -Y \dot{d} + \dot{\lambda} (\phi(Y) - d) \rightarrow \text{stat} . \quad (2.31)$$

The necessary condition for the extremum problem of the Lagrangian functional

$$\frac{\partial \mathcal{L}}{\partial Y} = -\dot{d} + \dot{\lambda} \frac{\partial \phi}{\partial Y} = 0 , \quad (2.32)$$

leads to an evolution law for the damage variable d in dependence of the Lagrangian multiplier $\dot{\lambda}$

$$\dot{d} = \frac{\partial f}{\partial Y} \dot{\lambda} = \frac{\partial \phi}{\partial Y} \dot{\lambda} \quad (\text{for } f = 0) . \quad (2.33)$$

Introducing the loading/unloading conditions according to the Kuhn-Tucker relations with λ as the damage consistency parameter

$$f \leq 0, \quad \dot{\lambda} \geq 0, \quad f \dot{\lambda} = 0, \quad (2.34)$$

and assuming that $\phi(\cdot)$ is a monotonic increasing function $\dot{\lambda}$ is determined by the consistency condition

$$\dot{f} = f = 0. \quad (2.35)$$

The derivative of the damage criterion

$$\dot{f} = \frac{\partial f}{\partial Y} \dot{Y} + \frac{\partial f}{\partial d} \dot{d} = \frac{\partial f}{\partial Y} \dot{Y} - \dot{d} = \frac{\partial f}{\partial Y} (\dot{Y} - \dot{\lambda}) = 0, \quad (2.36)$$

yields the following consistency parameter

$$\dot{\lambda} = \dot{Y}. \quad (2.37)$$

This results in a closed form expression for the damage variable

$$\dot{d} = \frac{\partial \phi(Y)}{\partial Y} \dot{Y} = \dot{\phi}(Y). \quad (2.38)$$

Usually the time integration of the damage evolution law is performed by an iterative predictor-corrector scheme. However, in some simple cases, an analytical integration yields an exponential expression for the growing damage variable d

$$d = \phi(Y) + d_0. \quad (2.39)$$

Remark: In the work at hand the initial damage value d_0 is equal to zero and the following functional form for the growing damage variable d is chosen:

$$\phi(Y) = 1 - e^{(-H(\tilde{\varepsilon}(Y) - Y_0))}, \quad d \in [0, 1) \quad (2.40)$$

$$d(t) = \max_{-\infty < \tau < t} \left\{ d(\tau), \phi(Y) \right\}. \quad (2.41)$$

In the above equation the material parameters H as the damage growth rate and Y_0 as the initial damage threshold are introduced. The maximization expression means that the damage variable always takes the maximal value during the time history t . This takes the irreversibility of the damage variable into account and ensures that the value of the damage variable never decreases. According to Simo and Ju [1987a] the strain energy Y is replaced by an equivalent strain measurement $\tilde{\varepsilon}(Y)$ which is obtained by a small modification of Y , namely the energy norm of the strain tensor

$$\tilde{\varepsilon}(Y) = \sqrt{2Y} = \sqrt{\boldsymbol{\varepsilon} : \mathbb{C}_e : \boldsymbol{\varepsilon}}. \quad (2.42)$$

There exist several proposals to calculate the equivalent strain (see e.g. Lemaitre

and Desmorat [2005] and Mazars and Pijaudier-Cabot [1989]). Choosing the energy norm of the strain tensor as an equivalent strain measurement in conjunction with the thermodynamic consistent (associated) damage formulation ensures the symmetry of the fourth order elastic-damage tangential material modulus \mathfrak{c} (see Simo and Ju [1987a]) which relates the stress rate tensor and the strain rate tensor $\dot{\boldsymbol{\sigma}} = \mathfrak{c} : \dot{\boldsymbol{\varepsilon}}$

$$\begin{aligned} \mathfrak{c} &= (1-d)\mathfrak{c}_e - \frac{\partial\phi}{\partial\tilde{\varepsilon}(Y)} \frac{\partial\tilde{\varepsilon}(Y)}{\partial\boldsymbol{\varepsilon}} \mathfrak{c}_e : \boldsymbol{\varepsilon} = (1-d)\mathfrak{c}_e - \frac{\partial\phi}{\partial\tilde{\varepsilon}(Y)} \frac{1}{\tilde{\varepsilon}(Y)} \boldsymbol{\sigma}_e \otimes \boldsymbol{\sigma}_e \\ &= (1-d)\mathfrak{c}_e - He^{-H(\tilde{\varepsilon}(Y)-Y_0)} \frac{1}{\tilde{\varepsilon}(Y)} \boldsymbol{\sigma}_e \otimes \boldsymbol{\sigma}_e . \end{aligned} \quad (2.43)$$

The schematic stress strain response of the elastic damage model is depicted in Figure 2.4. The Young's modulus E_e decreases progressively with increasing load and

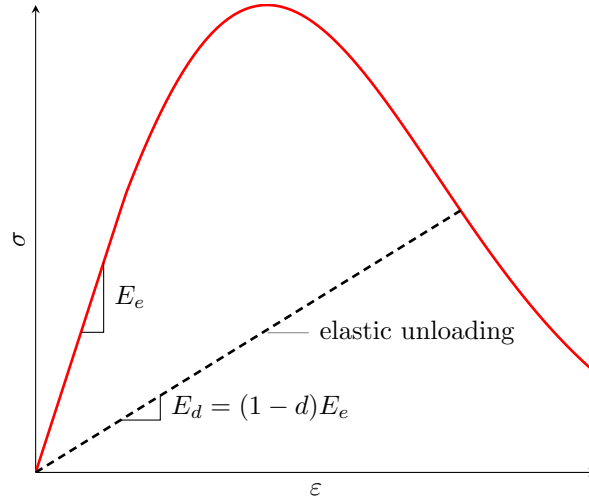


Figure 2.4: Schematic stress strain relation of the continuum damage model in a 1D tensile test.

increasing damage, while unloading occurs on linear paths. During these unloading paths the damage remains constant. Beyond the maximum stress peak, softening takes place and thus the tangential stiffness becomes negative. Failure of brittle materials usually occurs before the stress starts to decrease. A wide softening regime can be observed for rubber-like materials.

The basic equations of the elastic damage law are summarized in Table 2.1.

Helmholtz free energy	$\psi = \frac{1}{2}(1-d) \boldsymbol{\varepsilon} : \mathbb{C}_e : \boldsymbol{\varepsilon}$
Damage criterion	$f(Y, d) = \phi(Y) - d \leq 0$
Evolution law	$\dot{d} = \frac{\partial f}{\partial Y} \dot{Y}$ $d(t) = \max_{-\infty < \tau < t} \left\{ d(\tau), \phi(Y) \right\}$
State law	$\boldsymbol{\sigma} = (1-d)\mathbb{C}_e : \boldsymbol{\varepsilon}$

Table 2.1: Summary and basic equations of the isotropic damage model.

2.3.3 Elastoplasticity Coupled with Damage

While continuum damage mechanics focuses on the degradation of the elastic properties, due to growing microscopic defects (cracks or voids), the theory of plasticity is motivated by describing irreversible inelastic deformations based on microscopic slip or dislocation processes. Ductile materials, like e.g. thermoplastic polymers, show both effects at the same time and thus, a complex constitutive law containing the non-trivial interaction between the different processes is required. Several approaches of the coupling of both effects were introduced. For an overview and a discussion of some common models see for example Sciarra [1997], Hesebeck [2000] and Besson et al. [2010]. According to Besson et al. [2010] a basic classification in three characteristics is possible. First, the definition of the state or constitutive law which is derived from the free energy. The coupling of the dissipations and the form of the evolution of the variables associated with the dissipative mechanisms, and finally the form of the elastic limit criterion.

Neglecting thermal effects and considering isotropic damage and isotropic hardening only, the required state variables can be summarized according to Lemaitre and Desmorat [2005] in the following Table (2.2).

Mechanisms	State variables		Associated variables
	internal	observable	
Elasticity		$\boldsymbol{\varepsilon}_e$	$\boldsymbol{\sigma}$
Plasticity	$\boldsymbol{\varepsilon}_p$		$\boldsymbol{\sigma}$
Isotropic hardening	r		R
Isotropic damage	d		Y

Table 2.2: State and associated variables occurring in an elasto-plastic damage model.

In the following some general differences in the thermodynamic framework are described by means of two common models, namely the models of Lemaitre [1985a] and Ju [1989].

Model of Lemaitre

In the model of Lemaitre [1984, 1985b] (see also Lemaitre and Lippmann [1996]) the constitutive relations are derived from a thermodynamic potential, the Helmholtz free energy ψ , which is decomposed into an elastic ψ_e and into a plastic ψ_p part

$$\psi(\boldsymbol{\varepsilon}_e, d, r) = \psi_e(\boldsymbol{\varepsilon}_e, d) + \psi_p(r) = \frac{1}{2}(1-d) \boldsymbol{\varepsilon}_e : \mathbb{c}_e : \boldsymbol{\varepsilon}_e + \psi_p(r). \quad (2.44)$$

In this case there is no coupling between both effects, because the internal variables occur only in the respective associated part of the free energy. Consequently, the thermodynamic force Y associated with damage is only associated with the elastic part, namely the elastic energy release rate

$$Y = -\frac{\partial \psi}{\partial d} = -\frac{\partial \psi_e}{\partial d} = \frac{1}{2} \boldsymbol{\varepsilon}_e : \mathbb{c}_e : \boldsymbol{\varepsilon}_e. \quad (2.45)$$

The Cauchy stress is also defined in terms of the elastic part

$$\boldsymbol{\sigma} = \frac{\partial \psi}{\partial \boldsymbol{\varepsilon}_e} = \frac{\partial \psi_e}{\partial \boldsymbol{\varepsilon}_e} = (1-d) \mathbb{c}_e : \boldsymbol{\varepsilon}_e, \quad (2.46)$$

where \mathbb{c}_e is the isotropic elasticity tensor. The driving force R is conjugated to the isotropic hardening variable r and is derived from the plastic part of the free energy

$$R = -\frac{\partial \psi}{\partial r} = -\frac{\partial \psi_p(r)}{\partial r}. \quad (2.47)$$

Considering small deformations, the total strain tensor can be split into an elastic and a plastic part

$$\boldsymbol{\varepsilon} = \boldsymbol{\varepsilon}_e + \boldsymbol{\varepsilon}_p, \quad (2.48)$$

and the dissipation or Clausius-Duhem inequality for the purely mechanical problem takes the form

$$\mathcal{D} = \mathcal{P} - \dot{\psi} = \mathcal{P} - \dot{\psi}_e - \dot{\psi}_p \geq 0 \quad (2.49)$$

$$\mathcal{D} = \boldsymbol{\sigma} : (\dot{\boldsymbol{\varepsilon}}_e + \dot{\boldsymbol{\varepsilon}}_p) - \left(\frac{\partial \psi}{\partial \boldsymbol{\varepsilon}_e} \dot{\boldsymbol{\varepsilon}}_e + \frac{\partial \psi}{\partial r} \dot{r} + \frac{\partial \psi}{\partial d} \dot{d} \right) \geq 0. \quad (2.50)$$

Taking the time derivative of the free energy (2.44) the dissipation inequality can be written as the product of the thermodynamic forces with the associated internal variables

$$\mathcal{D} = \boldsymbol{\sigma} : \dot{\boldsymbol{\varepsilon}}_p - R \dot{r} + Y \dot{d} \geq 0. \quad (2.51)$$

The evolution laws of the internal variables are derived from a dissipation potential F associated with the variables

$$F(\boldsymbol{\sigma}, R, Y, d) = F_p(\boldsymbol{\sigma}, R, d) + F_d(Y, d) = f(\boldsymbol{\sigma}, R, d) + F_d(Y, d) , \quad (2.52)$$

whereby the potential can be decomposed into an elastic F_e and a plastic F_p part. Applying the normality rule and introducing only one common multiplier $\dot{\lambda}$ the following relations are obtained:

$$\dot{d} = \dot{\lambda} \frac{\partial F}{\partial Y} = \dot{\lambda} \frac{\partial F_d}{\partial Y} \quad (2.53)$$

$$\dot{\boldsymbol{\epsilon}}_p = \dot{\lambda} \frac{\partial F}{\partial \boldsymbol{\sigma}} = \dot{\lambda} \frac{\partial F_p}{\partial \boldsymbol{\sigma}} = \dot{\lambda} \frac{\partial f}{\partial \boldsymbol{\sigma}} \quad (2.54)$$

$$\dot{r} = -\dot{\lambda} \frac{\partial F}{\partial R} = -\dot{\lambda} \frac{\partial F_p}{\partial R} = -\dot{\lambda} \frac{\partial f}{\partial R} . \quad (2.55)$$

The associated evolution of the plastic flow is determined by a von Mises type yield function evaluated in the effective stress space

$$f(\boldsymbol{\sigma}, R, d) = f(\bar{\boldsymbol{\sigma}}, R) = \frac{\sigma_{eq}}{1-d} - \sigma_Y - R \leq 0 , \quad (2.56)$$

where σ_{eq} is the equivalent von Mises stress. According to the effective stress concept, the stress is replaced by its effective value and consequently the plastic flow is influenced by damage through the size of the effective elastic domain.

The plastic multiplier $\dot{\lambda}$ is determined from the consistency condition, $f = 0$, $\dot{f} = 0$. The condition, $f = 0$ means that the yield conditions is fulfilled and the current stress state is located on the actual yield surface. The second condition $\dot{f} = 0$ means that an increasing stress state leads to an increase of the yield stress. Elastic unloading occurs if the condition $f < 0$ or $\dot{f} < 0$ are satisfied. In this case the internal variables keep a constant value. The numerical integration of the model requires a Jacobian matrix containing all residual functions to solve the system of equations, see Lemaitre and Desmorat [2005] for details. Neglecting kinematic hardening de Souza Neto [2002] introduced a fast algorithm which consists only of one single equation.

The evolution of the damage variable is governed by the plastic strain and can only increase during plastic flow. Both effects are coupled through the same multiplier $\dot{\lambda}$. A separate treatment of the damage evolution can only be enabled to a limited degree by introducing a initial threshold value for the elastic strain energy release rate. Beyond this damage initiation threshold plastic flow comes always along with an increase in damage. Using the same multiplier $\dot{\lambda}$ the evolution of both internal variables are strongly coupled with each other. This fact represents in general a strong limitation in the modeling capacity. Especially for modeling materials, which show brittle damage character at lower strain states and a damage saturation effect with increasing ductility.

This damage saturation effect over the plastic strain (see Figure 2.5) was observed

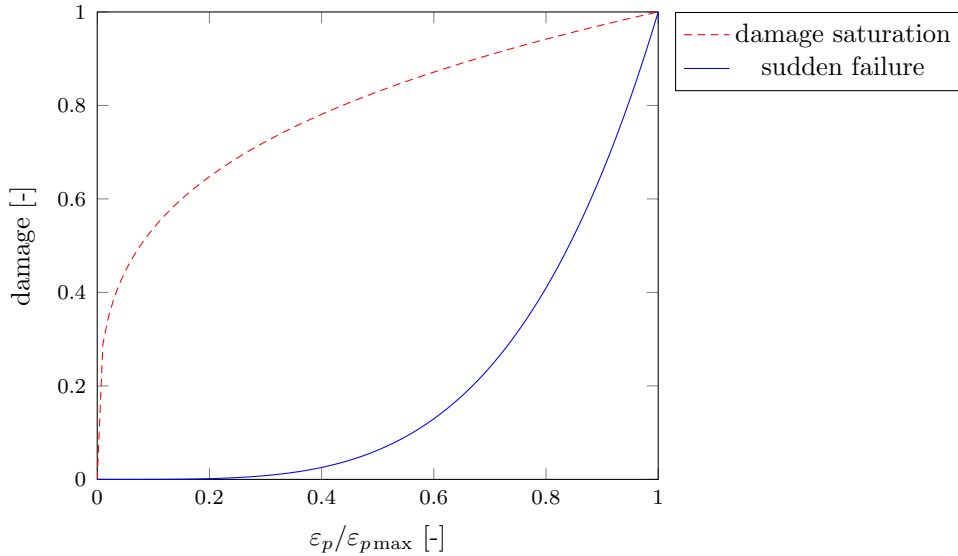


Figure 2.5: Possible curves for damage growth with increasing plastic strain.

e.g. for aluminum alloys (see Zhang and Cai [2010]), high strength steels (see e.g. Abu Al-Rub and Voyiadjis [2003] and Hesebeck [2001]) or thermoplastic polymers (see Detrez et al. [2011], Hoffmann [2012]). In Section 5.1.3 this behavior of thermoplastic polymers is shown and reproduced with numerical simulations. However, in other contributions (see e.g. Celentano and Chaboche [2007], Lemaitre and Desmorat [2005] and Saanouni et al. [2000]) an opposite behavior for steels or steel alloys is demonstrated. In this case damage starts growing only at higher plastic strain states, rises rapidly and ends in sudden ductile failure. A discussion for the damage accumulation behavior with increasing strain and a micromechanical interpretation in terms of the nucleation, grows and coalescence of voids can be found in Bonora [1997].

Model of Ju

The model of Ju [1989] is based on the former work of Simo and Ju [1987a] who originally formulated the model in the stress space. It treats the evolution of plastic and damage effects in an independent manner. This allows more flexibility in designing a material model and further, from the numerical point of view, the separation of plasticity and damage results in a reduction of the complexity of the numerical system and the problem becomes easier to solve. The free energy is decomposed in an elastic and a plastic part, whereby here the damage variable is also included in the plastic part

$$\psi(\boldsymbol{\varepsilon}_e, d, r) = \psi_e(\boldsymbol{\varepsilon}_e, d) + \psi_p(d, r) = \frac{1}{2}(1-d) (\boldsymbol{\varepsilon}_e : \mathbb{C}_e : \boldsymbol{\varepsilon}_e + \psi_p(r)) . \quad (2.57)$$

One can observe that the plastic hardening part of the free energy $\psi_p(d, r)$ is also dependent on the damage variable d . Thus, the state laws are obtained in the following form:

$$\boldsymbol{\sigma} = \frac{\partial \psi}{\partial \boldsymbol{\varepsilon}_e} = \frac{\partial \psi_e}{\partial \boldsymbol{\varepsilon}_e} = (1 - d) \mathbb{C}_e : \boldsymbol{\varepsilon}_e \quad (2.58)$$

$$Y = -\frac{\partial \psi}{\partial d} = \frac{1}{2} \boldsymbol{\varepsilon}_e : \mathbb{C}_e : \boldsymbol{\varepsilon}_e + \psi_p(r) \quad (2.59)$$

$$R = -\frac{\partial \psi}{\partial r} = -\frac{\partial \psi_p}{\partial r} . \quad (2.60)$$

Hence, the damage conjugated force Y includes, contrary to Lemaitre [1984, 1985b] and Cordebois and Sidoroff [1982] an additional plastic part. This approach which was also followed by Saanouni [1988], Saanouni et al. [1994] considers the influence of the plastic strain on the continuous micro crack process. The evolution laws of the internal variables are derived from two independent dissipation potentials F_p and F_d and two independent multipliers $\dot{\lambda}_p$ and $\dot{\lambda}_d$. Furthermore, both mechanisms are controlled by two independent criteria.

$$f_p(\boldsymbol{\sigma}, R, d) \leq 0 \quad f_d(Y, d) \leq 0 \quad (2.61)$$

$$F_p(\boldsymbol{\sigma}, R, d) \quad F_d(Y, d) \quad (2.62)$$

$$\dot{\boldsymbol{\varepsilon}}_p = \dot{\lambda}_p \frac{\partial F_p}{\partial \boldsymbol{\sigma}} = \dot{\lambda} \frac{\partial f_p}{\partial \boldsymbol{\sigma}} \quad \dot{d} = \dot{\lambda}_d \frac{\partial F_d}{\partial Y} \quad (2.63)$$

$$\dot{r} = -\dot{\lambda}_p \frac{\partial F_p}{\partial R} = -\dot{\lambda} \frac{\partial f_p}{\partial R} \quad (2.64)$$

The associated evolution of the plastic flow is determined by a von Mises type yield function which is evaluated in the effective stress space, similar to Lemaitre's model

$$f_p(\boldsymbol{\sigma}, R, d) = f_p(\bar{\boldsymbol{\sigma}}, R) = \frac{\sigma_{eq}}{1 - d} - \sigma_Y - R \leq 0 . \quad (2.65)$$

The damage criterion is characterized by a damage threshold in terms of a current energy barrier that limits the elastic domain

$$f_d(Y, d) = Y(t) - \max_{-\infty < \tau < t} \{Y\} . \quad (2.66)$$

The two independent multipliers for plasticity and damage are determined by the two consistency conditions $f_p = \dot{f}_p = 0$ and $f_d = \dot{f}_d = 0$.

The computational algorithm for the integration of the elastoplastic damage evolu-

tion is straightforward and efficient. It consists of three independent steps:

1. Elastic predictor
2. Plastic corrector
3. Damage corrector

The plastic corrector step is in the case of the simple von Mises type plasticity usually solved using the return mapping algorithm Simo and Hughes [1998] followed from an additional damage corrector step which is usually performed in a single iteration step. This approach is in general quite popular because it allows to establish independent relations for plasticity and damage. Similar ideas are followed by many other authors in this field, see for instance Chow and Wang [1987], Hansen and Schreyer [1994], Zhu and Cescotto [1995] or Chaboche [1996]. Both mechanisms are coupled only by the effective stress concept in the plastic yield criterion, like in the Lemaitre model, but additionally the plastic part of the strain energy is evolved in the associated evolution of the damage variable. Within this model the extreme cases of material behavior can be captured. For instance, brittle damage, that takes place without a remarkable increase of the plastic strain. On the opposite it is possible to model large plastic strains before damage occurs.

In the following, possible choices for the thermodynamic potentials and the resultant evolution laws for the internal variables are given. The evolution of the plastic strain $\boldsymbol{\varepsilon}_p$ and the isotropic hardening variable r are formulated similar to ordinary von Mises plasticity

$$F_p(\boldsymbol{\sigma}, R, d) = f_p(\boldsymbol{\sigma}, R, d) = \frac{\sigma^{eq}}{1-d} - \sigma_Y - R \quad (2.67)$$

$$\Rightarrow \dot{\boldsymbol{\varepsilon}}_p = \dot{\lambda}_p \frac{3}{2} \frac{\boldsymbol{\sigma}^{dev}}{(1-d)\sigma^{eq}} \quad (2.68)$$

$$\Rightarrow \dot{r} = \dot{\lambda}_p = (1-d)\dot{\varepsilon}_p^{eq}. \quad (2.69)$$

Simo and Ju [1987a] and Ju [1989] proposed to define the damage evolution as a function of the strain energy Y

$$F_d(Y) = 1 - \frac{Y_0(1-b_1)}{Y} - b_1 e^{b_2(Y_0-Y)} \quad (2.70)$$

$$\Rightarrow \dot{d} = \dot{\lambda}_d \frac{\partial F_d(Y)}{\partial Y} = \dot{Y} \left(\frac{Y_0(1-b_1)}{Y^2} + b_1 b_2 e^{b_2(Y_0-Y)} \right). \quad (2.71)$$

Thus the damage variable can directly be expressed form the current value of Y . It is possible to formulate the damage accumulation in terms of a closed form expression of the damage variabel according to Mazars et al. [1981]

$$d = 1 - \frac{Y_0(1-b_1)}{Y} - b_1 e^{b_2(Y_0-Y)}. \quad (2.72)$$

The above expression was used by Simo and Ju [1989] to describe quasi-static damage propagation in the context of elasto-plasticity and damage at finite strains. The evolution of the damage variable can be expressed additionally as a function of the current absolute value of the damage variable itself, as proposed by Hesebeck [2001]. This enables to model the saturation of damage in dependence of the total damage history

$$F_d(Y, d) = b_1 \frac{Y^2}{2} e^{-b_2 d} \quad \Rightarrow \quad \dot{d} = \dot{Y} b_1 Y e^{-b_2 d} . \quad (2.73)$$

The isotropic hardening can be defined by linear or exponential functions of the hardening variable r

$$\psi_p(r) = a_1 \left(r + \frac{1}{a_2} e^{-a_2 r} \right) \quad \Rightarrow \quad R = a_1 (1 - e^{-a_2 r}) \quad (2.74)$$

$$\psi_p(r) = \frac{a_1}{2} r^2 \quad \Rightarrow \quad R = a_1 r . \quad (2.75)$$

In general it is desirable to have a method for measuring the damage variable. The simplest way, among others (see Lemaitre and Desmorat [2005], Tasan et al. [2012]), is the measurement of the degradation of the elastic modulus E_d

$$d = 1 - \frac{E_d}{E_e} . \quad (2.76)$$

This can be realized in some cyclic tensile tests (see Section 5.1.3), whereby the degraded modulus can be determined in the unloading regime.

In Table 2.3 the basic equations of the elasto-plastic damage law are summarized.

Helmholtz free energy	$\psi = \frac{1}{2}(1 - d) (\boldsymbol{\varepsilon}_e : \mathbb{C}_e : \boldsymbol{\varepsilon}_e + \psi_p(r))$
Damage criterion	$f_d(Y, d) = Y(t) - \max_{-\infty < \tau < t} \{Y\} \leq 0$
Plasticity criterion	$f_p(\boldsymbol{\sigma}, R, d) = f_p(\bar{\boldsymbol{\sigma}}, R) = \frac{\sigma_{eq}}{1-d} - \sigma_Y - R \leq 0$
Evolution laws	$\dot{\boldsymbol{\varepsilon}}_p = \dot{\lambda}_p \frac{\partial F_p}{\partial \boldsymbol{\sigma}}$ $\dot{d} = \dot{\lambda}_d \frac{\partial F_d}{\partial Y}$ $\dot{r} = -\dot{\lambda}_p \frac{\partial F_p}{\partial R}$
State laws	$\boldsymbol{\sigma} = \frac{\partial \psi}{\partial \boldsymbol{\varepsilon}_e} = \frac{\partial \psi_e}{\partial \boldsymbol{\varepsilon}_e} = (1 - d) \mathbb{C}_e : \boldsymbol{\varepsilon}_e$ $Y = -\frac{\partial \psi}{\partial d} = \frac{1}{2} \boldsymbol{\varepsilon}_e : \mathbb{C}_e : \boldsymbol{\varepsilon}_e + \psi_p(r)$ $R = \frac{\partial \psi}{\partial r} = \frac{\partial \psi_p}{\partial r}$

Table 2.3: Summary and basic equations of the elasto-plastic damage model.

2.4 Micromechanics and Homogenization

In this section the basics of homogenization as well as analytical bounds for effective composite properties are explained. In addition, a comprehensive overview of analytical, semi-analytical and numerical homogenization methods is given.

2.4.1 Basic Concept and Length Scales

Engineering materials and also naturally occurring materials are often considered as homogeneous on the macroscopic scale. But on certain finer scales these materials show heterogeneities, like different laminate layers at the meso scale, inclusions, cracks or voids at the microscale or grain boundaries and defects or irregularities in the crystal lattice at the atomistic scale (see Figure 2.6).

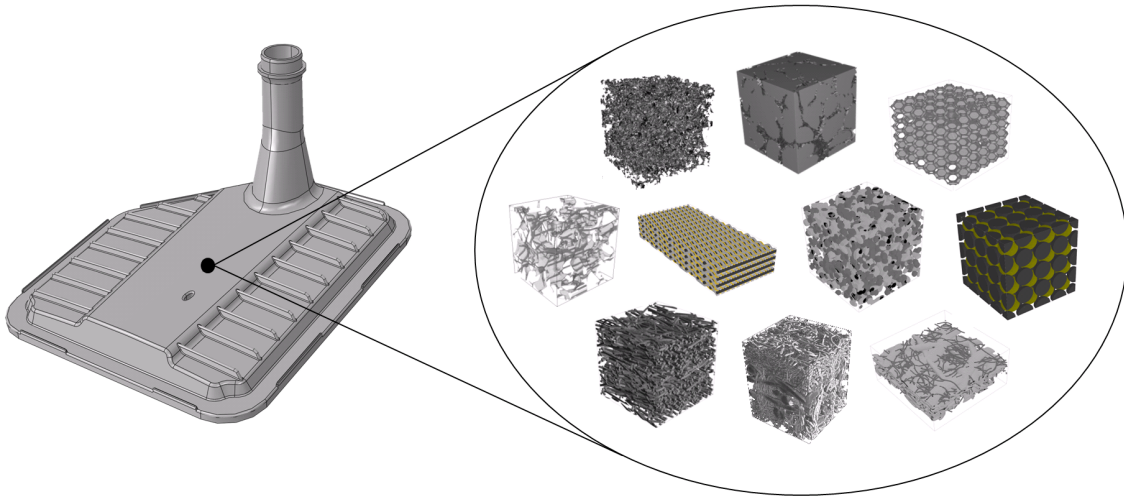


Figure 2.6: Equivalent Mises stress distribution in a homogeneous component at the macroscale (filter housing of IBS Filtran GmbH) and underlying heterogeneous microstructures.

Micromechanical concepts investigate the influence of these heterogeneities or defects on the macroscopic material behavior. These inhomogeneities are often characteristic for the macroscopic behavior and in many cases, even represent local stress concentrations and thus, initiate local material degradation. On the other hand, a more detailed consideration of the material structure increases the computational effort of the mechanical problem. The correct choice of the scales and which of them influence the macroscopic material behavior in a significant way are important issues of the micromechanical model. Furthermore, in a coupled simulation, the connection between the scales has to be realized within a technical framework.

The overall material behavior of a microstructure is regarded as the behavior of a single macroscopic material point. This micro-macro transition is performed with suitable averaging techniques of the spatial quantities and is referred to as homogenization. The macroscopic properties which are influenced by the microstructural

quantities are called effective properties. These properties characterize the macroscopic material by averaging the underlying heterogeneous microstructure. They are determined on a sample which has to be representative for the microscopic material setting, the so-called representative volume element (RVE) which was suggested by Hill [1963].

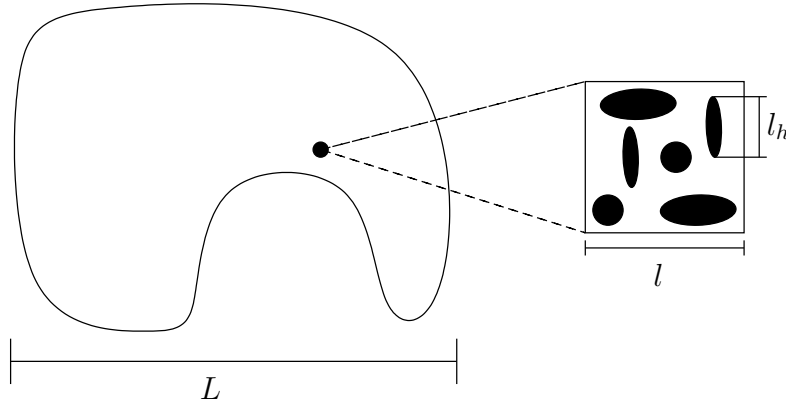


Figure 2.7: Characteristic lengthscales on macro and microscale.

For a sample to be representative in a statistical sense, its characteristic length L has to be much larger than the characteristic length l of the attached RVE

$$L \gg l. \quad (2.77)$$

Thus, the assumption of separation of scales holds, which allows a separate treatment of multiple scales. Furthermore, the sample must contain a sufficient large number of heterogeneities, and thus, the characteristic length l_h of the heterogeneities² has to be much smaller than the characteristic length l of the microstructure

$$l \gg l_h. \quad (2.78)$$

The mathematical theory of homogenization (see e.g. Bakhvalov and Panasenko [1989] and Sánchez-Palencia [1980]) introduces a small parameter as the ratio between the characteristic length of the heterogeneities and the length of the microstructure. Homogenized equations are obtained if this parameter goes to 0. On the other hand, to keep the computational effort of a RVE simulation in acceptable limit the RVE size should be as small as possible. The representative size of the RVE depends on the scale of the underlying microstructure and the size of its heterogeneities. The statistical representativity can be tested by investigating the convergence of the responses of varying RVE sizes. By applying uniform traction or displacement boundary conditions on a RVE the response should coincide in both cases and even more for arbitrary boundary conditions. For a detailed study of the

²The characteristic length l_h can also be determined by other microscopic values, like for example the localization or buckling length.

construction and testing of representative samples the reader is referred to the work of Drugan and Willis [1996], Gusev [1997], Kanit et al. [2003], Ostoja-Starzewski [2006], Gitman et al. [2007] or more recently, Balzani et al. [2014].

2.4.2 Bounds and Estimates

The simplest approach for forming effective, homogenized quantities of heterogeneous materials is given by the rule of mixtures. The average properties are obtained by adding the different properties of the material phases, weighted by their volume fraction c_α . Averaging either the stiffness moduli or the compliance of the material phases upper or lower bounds for the macroscopic effective moduli have been proposed by Voigt [1889] and Reuss [1929]. Voigt assumed constant strains in

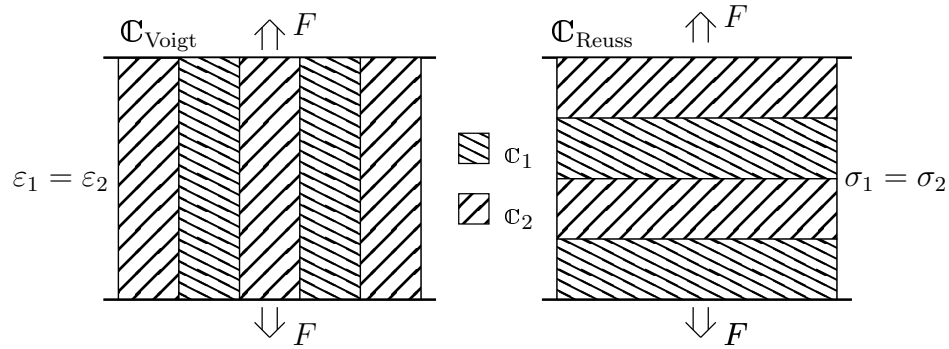


Figure 2.8: Simplified stiffness model for estimating the effective properties of a composite material. Left, constant strain condition, Voigt bound, right, constant stress condition, Reuss bound.

the materials phases under macroscopic loading. The obtained effective composite properties correspond to the effective response of simplified stiffness model in which the material phases are arranged in a parallel manner. Conversely, Reuss simplified the macroscopic homogenized behavior of a composite by a serial arrangement of the phases' properties and thus, the microscopic constituents are subjected to the same uniform stress.

$$\mathbf{C}_{\text{Voigt}} = \sum_{\alpha=1}^n c_\alpha \mathbf{C}_\alpha = \langle \mathbf{C} \rangle, \quad \boldsymbol{\varepsilon}(\mathbf{x}) = \langle \boldsymbol{\varepsilon} \rangle = \text{const} \quad (2.79)$$

$$\mathbf{C}_{\text{Reuss}}^{-1} = \sum_{\alpha=1}^n c_\alpha \mathbf{C}_\alpha^{-1} = \langle \mathbf{C}^{-1} \rangle, \quad \boldsymbol{\sigma}(\mathbf{x}) = \langle \boldsymbol{\sigma} \rangle = \text{const} \quad (2.80)$$

In the above equations the brackets $\langle \cdot \rangle$ denote the average of a certain quantity, and c_α the volume fraction of the phase α . The results are rough estimates of the macroscopic effective properties. More rigorous bounds for overall properties are obtained using variational principles which were introduced by Hashin and Shtrikman [1963] for heterogeneous multiphase materials. These second order bounds are based on the principle of minimum potential energy and use the concept of polarization with an auxiliary stress or strain field. The result are strict optimal upper and lower bounds for the overall properties of composites. Nonlinear extensions of the

Hashin-Shtrikman variational principle were proposed by Ponte Castañeda [1991, 1992], Talbot and Willis [1985] and Suquet [1993].

2.4.3 Analytical Homogenization Techniques

Classical analytical methods relate back to Eshelby's inclusion theory (Eshelby [1957]) which considers the micromechanical material response by means of analytical approximations. The heterogeneous microstructure is decomposed into a homogeneous infinite matrix material and isolated inclusions which are approximated by spheres or ellipsoids. Assuming constant, uniform stress and strain fields in the inclusions the elastic field under uniform far field loading is obtained. Extensions of Eshelby's inclusion theory for determining effective properties of composites including several regularly shaped particles were developed. The so called mean-field approaches consider interaction of inclusions by mutual influence of its analytical microfields. In this regard, see for instance the work of Kröner [1958] who introduced the so-called self-consistent scheme (see Hashin [1962], Budiansky [1965] and Hill [1965]) or the generalized self-consistent scheme (see Christensen and Lo [1979], Christensen [1990]). Furthermore, in the context of interacting adjacent particles, the Mori-Tanaka method (Mori and Tanaka [1973]) was introduced and later extended by Benveniste [1987] and Lielens [1999]. With regard to analytical methods based on Eshelby's theory the differential scheme (see e.g. McLaughlin [1977]) and the double inclusion method (Nemat-Nasser et al. [1993]) have to be mentioned. Moreover, higher order theories have been proposed by Ponte Castañeda [1996, 2002], Ponte Castañeda and Suquet [1997] and Suquet [1995] using the secant or tangent moduli of the phases. In a more mathematical context the asymptotic homogenization theory, documented in Bensoussan et al. [1978, 2011], Sánchez-Palencia [1980] and Fish et al. [1999] should be mentioned. Within this method asymptotic expansions of displacement and stress fields provide the effective (homogenized) material parameters by applying appropriate variational principles.

However, there are a number of limitations coming along with analytical methods (see for instance Hashin [1983]). These closed form estimates fail in cases of large stiffness ratios between the inclusion and the matrix material or for structures with a complex microscopic setting. Therefore, they are restricted to simple inclusion shapes (ellipsoidal, convex, unbent) which are uniformly distributed, see e.g. the work of Klusemann et al. [2012], who investigated several analytical methods concerning their applicability for materials with inhomogeneities of non-elliptical shape. Furthermore, interactions between inclusions and local stress and strain concentrations are only captured to a limited degree. Damage and failure are governed by these local field concentrations and hence, analytical methods experience difficulties in modeling progressive damage and failure of composite materials.

2.4.4 Semi-analytical Homogenization Techniques

To overcome the shortcomings related to analytical homogenization methods, semi-analytical methods were proposed. The key idea is to utilize the benefits of numerical homogenization techniques in terms of their accuracy and keep at the same time the efficiency of analytical methods. In this regard, the method of cells (Aboudi [1989]), later extended to the generalized method of cells (see Aboudi [1996], Paley and Aboudi [1992]), and the Transformation Field analysis (TFA) proposed by Dvorak [1992] were introduced.

The latter method aims to reconstruct local inelastic fields from a finite number of precomputed eigen- or transformation modes using interpolation operators. The number of internal variables to be stored is reduced by decomposing the unit cell into a finite number of subdomains. The inelastic transformation strains which can be caused by e.g. plastic strain or thermal expansion are considered to be uniform in the subdomains. The constant strain $\boldsymbol{\varepsilon}$ in each subdomain s caused by given eigenstrains $\boldsymbol{\varepsilon}^*$ in the subdomains r is obtained by

$$\boldsymbol{\varepsilon}_s = \mathbf{A}_s : \mathbf{E} + \sum_r \mathbb{L}_{sr} : \boldsymbol{\varepsilon}_r^*. \quad (2.81)$$

The mechanical influence or localization tensor \mathbf{A} and the transformation influence tensor \mathbb{L} describe the local influence of the macroscopic strain \mathbf{E} and the given eigenstrains $\boldsymbol{\varepsilon}^*$. These fourth order tensors depend on the local elastic moduli, as well as the shape and volume fraction of the material phases. In simple cases they can be expressed in closed form by means of Eshelby tensors. For a larger number of subdomains and complex shaped microstructures the tensors are precomputed by solving a set of linear elastic unit cell problems. Chaboche et al. [2001] and Fish et al. [1997] for instance, used the method for analyzing composite structures under consideration of plasticity and damage effects. However, in many cases a large number of subdomains is necessary to predict the effective material behavior correctly.

In order to increase the accuracy within an acceptable computational effort, Michel and Suquet [2003] introduced the so-called nonuniform TFA for considering a nonuniform distribution of eigenstrains in the subdomains. While the localization and transformation tensors are precomputed in elastic load cases, the spatially dependent transformation fields $\boldsymbol{\varepsilon}^*(\boldsymbol{x})$ are determined by solving selected inelastic unit cell problems during several time steps. In crystal plasticity the inelastic load cases are selected according to existing crystal slip systems and are referred to as plastic modes. In general cases these modes are identified from the precomputed fields (snapshots) by an eigenvalue analysis (see e.g. Proper Orthogonal Decomposition (POD) method). In the framework of a multiscale simulation the applied macroscopic load history is defined by the strain tensor $\mathbf{E}(t)$. The path dependent effective

stress response $\boldsymbol{\Sigma}(t)$ is obtained by superposition of the precomputed modes $\boldsymbol{\varepsilon}_j^*(\boldsymbol{x})$

$$\boldsymbol{\Sigma}(t) = \underbrace{\mathbf{c}(\boldsymbol{x}) : \mathbf{A}(\boldsymbol{x}) : \mathbf{E}(t)}_{\textcircled{1}} + \sum_j \underbrace{\langle \mathbf{c}(\boldsymbol{x}) : (\mathbb{L} * \boldsymbol{\mu}_j(\boldsymbol{x}) - \boldsymbol{\varepsilon}_j^*(\boldsymbol{x})) \rangle}_{\textcircled{2}} \varepsilon_j(t). \quad (2.82)$$

The scalar mode stimulation coefficients or generalized inelastic strains $\varepsilon_j(t)$, respectively, result from evolution equations for each mode. In an iterative time integration scheme the constitutive law is integrated and the current coefficients $\varepsilon_j^{t+\Delta t}$ corresponding to the current macroscopic load $\mathbf{E}^{t+\Delta t}$ are obtained. The tensors in expressions $\textcircled{1}$ (the effective elastic stiffness) and $\textcircled{2}$ are computed once in advance. For more details about the computational implementation of the method see Michel and Suquet [2004] and Fritzen and Böhlke [2010]. In contrary to Michel and Suquet [2003, 2004] who used the FFT method (see Moulinec and Suquet [1998], Section 3.2) to solve two dimensional precomputed unit cell problems, Fritzen and Böhlke [2010] discretized the microstructure using finite elements and extended the method to three dimensional plasticity problems. Recent contributions take into account rate dependent material behavior, see Roussette et al. [2009], Fritzen and Boehlke [2013] in the context of viscoplasticity and viscoelasticity. Largenton et al. [2014] extended the method for viscoelasticity in the presence of aging and swelling.

Besides the evident benefits in terms of reducing the size of the numerical model significantly, the method points out some limitations: First, the choice of the pre-computed modes is a difficult task and in general depends on the type of macroscopic loading. Especially when strongly non-proportional, cyclic and/or temperature dependent loads are applied, hardly any macroscopic loading situation could be reconstructed from precomputed modes. The same applies to strongly anisotropic structures with even anisotropic constitutive behavior of the constituents. Due to the applied superposition principle the method is limited to infinitesimal strains. Furthermore, for defining evolution laws only a class of generalized standard materials can be applied to specify the phases' constitutive behavior.

Remark: The expression in (2.81) can be seen as discretization of a continuous strain field. The exact expression can be obtained by applying a Green's operator Γ operating on the transformation strain induced eigenstress $\boldsymbol{\tau} = \mathbf{c} : \boldsymbol{\varepsilon}^*$

$$\boldsymbol{\varepsilon}(\boldsymbol{x}) = \mathbf{A}(\boldsymbol{x}) : \mathbf{E} + \frac{1}{|\omega|} \int_{\omega} \mathbb{L}(\boldsymbol{x}, \boldsymbol{y}) : \boldsymbol{\varepsilon}^*(\boldsymbol{y}) \, d\boldsymbol{y}, \quad (2.83)$$

with $\mathbb{L}(\boldsymbol{x}, \boldsymbol{y}) = \Gamma(\boldsymbol{x}, \boldsymbol{y}) : \mathbf{c}(\boldsymbol{y})$.

For more detailed information on the Green's operator see Section 3.2 of this work. An overview of classical analytical and semi-analytical homogenization methods can be found in Mura [1987], Nemat-Nasser and Hori [1999], Torquato [2002] and Segurado and Llorca [2002], more recently in Zohdi and Wriggers [2008], Gross and Seelig [2011] and Christensen [2012]. Recent comprehensive overviews and critical comparisons of different methods can be found in the work of Kanouté et al. [2009] and Geers et al. [2010].

2.4.5 Computational Homogenization Techniques

With increasing computational power numerical homogenization methods or full-field simulations become more and more interesting. Instead of formulating closed-form macroscopic constitutive equations, the microscopic material setting is directly resolved on a finer length scale. The actual physical phenomena occurring on a finer scale are captured and consequently, the direct simulation substantially improves the accuracy of the macroscopic material response. In addition, the direct resolution of the microscopic constituents enables to deal with complex inclusion shapes like non-elliptical or even convex geometries.

Several modeling and simulation techniques were developed in the last decade to obtain the effective numerical material response and establish the coupling across different length scales. There are various ways to classify multiscale or numerical homogenization methods in a general setting, see for instance Weinan et al. [2007]. Domain decomposition methods, so-called (embedded) concurrent methods, decompose the macroscopic domain in several finer subdomains. The coarse scale mesh is refined in interesting zones by resolving the microstructural setting, whereby both modeling scales refer to the same length scale. Thus, the scales are strongly linked together and solved simultaneously. Mutual exchange of information takes place between the scales in both directions. For contributions in this field see the e.g. the work of Zohdi and Wriggers [1999], Farhat et al. [2000], Guidault et al. [2008], Ibrahimbegović and Markovič [2003] and Belytschko et al. [1990].

On the other hand hierarchical methods pre-compute effective properties on a separated microscale problem and pass this information to a coupled or uncoupled macroscale. Due to the fact that the fine and the coarse scale problem 'live' in different length scales the assumption of the separation of scales is valid and the microscopic sample can be regarded as a representative volume element (RVE). The idea of computing the microscopic material response by solving a separate microscopic boundary value problem was introduced by Suquet [1985, 1987] and Renard and Marmonier [1987].

In an uncoupled simulation effective homogenized properties are pre-computed on a discretized microscopic cell containing the microscopic structural setting. Subsequently, the effective quantities are transferred to the macroscale and used to formulate effective constitutive equations. The exchange only takes place in one direction in terms of a numerical upscaling process. This allows to pre-compute anisotropic linear elastic properties. Furthermore, the method can be used to provide quantities like failure or yield surfaces for a nonlinear macroscopic simulation. In the context of pre-computing viscoelastic fiber composites see for instance Staub et al. [2012] or Schmidt [2011] for elasto-plastic polymers.

Dealing with strongly nonlinear problems including microscopic irreversible effects, like progressive damage, an iterative coupling between the scales is necessary. Within the scope of a coupled hierarchical simulation the separated scales are solved sequentially, information passes in both directions and a mutual exchange between both scales takes place. Every macroscopic point is equipped with a certain microstructure which captures the complete geometrical information by detailed modeling of

the microstructural setting. The macroscopic constitutive material behavior at a particular point is replaced by the effective response of a representative sample associated with this point. For describing the mechanical behavior any arbitrary constitutive law can be assigned to the microscopic constituents.

Following the ideas of Guedes and Kikuchi [1990], Ghosh et al. [1995], Smit et al. [1998] and Miehe et al. [1999] coupled computational homogenization techniques were developed. One well-known method is the FE^2 approach introduced by Feyel and Chaboche [2000]. Appropriate boundary conditions which are mainly linear displacements, constant tractions or periodic conditions are applied on the RVE. For different techniques to impose these boundary conditions see for instance Kouznetsova et al. [2001], Miehe and Koch [2002] and Bayreuther [2005]. The microscopic boundary value problem is solved using numerical approximation techniques. Besides the finite element method which is used in most publications in this context (see e.g. Kouznetsova et al. [2001], Miehe et al. [1999] and Terada et al. [2000]), other numerical methods are used to analyze the microstructural problem, like the Voronoi-Cell method documented in Ghosh et al. [1995, 1996], or methods using fast Fourier transforms introduced by Moulinec and Suquet [1998]. The latter was compared in Michel et al. [1999] with the finite element method for computing linear effective properties of composites. Both methods are also described shortly in Chapter 3.

Furthermore, Kouznetsova et al. [2004, 2002] introduced homogenization schemes of higher order. These methods involve higher order approximations of the strain and stress fields. Consequently, besides the macroscopic strain also its gradients are imposed on the microscopic domain. The response of the microscale boundary value problem contains in addition to the averaged stress tensor, also the higher-order stress tensor and the corresponding tangents. Consequently, the size of the RVE is taken into account and geometrical size effects, as far as they occur, are considered. Softening and localization phenomena coming along with damage and fracture of heterogeneous microstructured materials can be treated independently of the macroscopic mesh size.

Regarding damage and fracture of composite materials the continuous-discontinuous homogenization approach represents another interesting multiscale technique which enables to deal with macroscopic localization effects. The macroscale is enriched with a discontinuity in terms of an effective displacement jump. This enables the incorporation of a macroscopic crack which is obtained by extracting a shear band on the microscopic scale. In this regard see for instance the work of Coenen et al. [2012], Massart et al. [2007] and Linder and Raina [2013]. In these contributions the macroscopic enrichment is based on the embedded discontinuity concept (see Armero and Garikipati [1996], Linder and Armero [2007] and Simo et al. [1993]). Loehnert and Belytschko [2007] proposed the so-called multiscale projection method using the extended finite element method (XFEM) approach to incorporate a discontinuity at the macroscale. In this context the so-called multiscale aggregating discontinuity was proposed by Belytschko et al. [2008] and Song and Belytschko [2009]. This method also takes the advantages of the XFEM approach to inject a discontinuity at the macroscale which is in this case obtained by 'aggregating' the averaged microscopic

localization effects. However, due to the fact that the fine scale problem and its corresponding macro element have the same size, the separation of scales is no longer valid.

In this work a classical first order homogenization scheme is employed. The development of macroscopic cracks is not treated and the simulations performed in this work were stopped when localization on the coarse scale occurred. Thus, the assumption of separation of scales remains valid.

Recent contributions concerning the FE² method can be found in Schröder [2014] or Gruttmann and Wagner [2013] in the context of layered shell structures. Numerical investigations of damage in fiber reinforced thermoplastic polymers with experimental background are addressed in Hoffmann [2012], Pan and Pelegri [2011] and Spahn et al. [2014b]. Multiscale techniques concerning damage of composite materials were presented by Zohdi et al. [1998], Döbert [2001] or more recently by Unger and Eckardt [2011].

First Order Homogenization Technique

The classical first order homogenization schemes consist of four steps (see Kouznetsova et al. [2001]):

- defining a representative volume element including the definition of the material phases' constitutive behavior
- choosing appropriate boundary conditions derived from macroscopic quantities
- determining the macroscopic variables from the computed microscopic solution fields
- specify the relation between the macroscopic input and computed output variables (tangential stiffness matrix)

Effective macroscopic properties, basically the stress or strain response are obtained by averaging the computed microscopic solution fields. The macroscopic stresses Σ or strains \mathbf{E} are calculated as the volume average over the volume ω of the RVE

$$\Sigma = \langle \boldsymbol{\sigma} \rangle = \frac{1}{|\omega|} \int_{\omega} \boldsymbol{\sigma} \, dv \quad (2.84)$$

$$\mathbf{E} = \langle \mathbf{E} \rangle = \frac{1}{|\omega|} \int_{\omega} \boldsymbol{\varepsilon} \, dv . \quad (2.85)$$

The computation of the macroscopic stress during the homogenization procedure has to meet the energy criterion proposed by Hill [1963, 1972]. This energy averaging theorem, also known as Hill-Mandel condition, states that the rate of mechanical work done at the microscale equals the rate of work resulting from the computed macroscopic quantities. The micro-macro work balance in differential form has to

be satisfied

$$\boldsymbol{\Sigma} : \dot{\mathbf{E}} = \langle \boldsymbol{\sigma} : \dot{\boldsymbol{\epsilon}} \rangle = \frac{1}{|\omega|} \int_{\omega} \boldsymbol{\sigma} : \dot{\boldsymbol{\epsilon}} \, dv . \quad (2.86)$$

In the sense of a direct micro-macro scale coupling the averaged variables are transferred or upscaled to the macroscale. Using the Newton-Raphson algorithm to solve the global macroscopic BVP the macroscopic tangent stiffness has to be computed. The tangential stiffness matrix sets the macroscopic load in relation to the microscopic solution fields. In a strain driven algorithm the tangent is defined as the derivative of the computed averaged stress with respect to the macroscopic strain

$$\mathbb{C} = \frac{\partial \boldsymbol{\Sigma}}{\partial \mathbf{E}} . \quad (2.87)$$

In general, the constitutive behavior on the macroscale is not explicitly defined a priori and thus, there is no closed form expression of the macroscopic tangent at each macro point available. The stiffness matrix has to be determined numerically. Classical FE² schemes use finite elements to solve the boundary value problems on both scales. The tangent can be directly obtained using the condensed microscopic (global) stiffness matrix \mathbf{k} received from the RVE computation. Miehe and Koch [2002] extracted the overall stress and stiffness tangent in terms of the relation between forces acting on the RVE boundary and the associated boundary displacements. Lagrange multiplier method was used to incorporate the boundary constraints. An similar approach was proposed by Kouznetsova et al. [2001], Kouznetsova [2002] which is based on a direct condensation of the constrained degrees of freedom. The microstructural system is rearranged through partition of the global matrix \mathbf{k} into degrees of freedom related to the boundary (index b) and the inner nodes (index a)

$$\begin{bmatrix} \mathbf{k}_{bb} & \mathbf{k}_{ba} \\ \mathbf{k}_{ab} & \mathbf{k}_{aa} \end{bmatrix} \begin{bmatrix} \mathbf{u}_b \\ \mathbf{u}_a \end{bmatrix} = \begin{bmatrix} \mathbf{f}_b \\ \mathbf{0} \end{bmatrix} . \quad (2.88)$$

Macroscopic stress and the macroscopic tangent are obtained from the external force vector \mathbf{f}_b on the boundary and from the condensed stiffness matrix $\tilde{\mathbf{k}}_{bb}$ associated with this boundary

$$\tilde{\mathbf{k}}_{bb} = \mathbf{k}_{bb} - \mathbf{k}_{ba} \mathbf{k}_{aa}^{-1} \mathbf{k}_{ab} \quad (2.89)$$

$$\mathbf{f}_b = \tilde{\mathbf{k}}_{bb} \mathbf{u}_b \quad (2.90)$$

$$\boldsymbol{\Sigma} = \frac{1}{|\omega|} \mathbf{D} \mathbf{f}_b \quad (2.91)$$

$$\mathbb{C} = \frac{\partial \boldsymbol{\Sigma}}{\partial \mathbf{E}} = \frac{1}{|\omega|} \mathbf{D} \tilde{\mathbf{k}}_{bb} \mathbf{D}^T . \quad (2.92)$$

Thereby \mathbf{D} denotes the global coordinate matrix associated with all surface points.

The direct tangent computation appears very efficient, but the inverse \mathbf{k}_{aa}^{-1} is not determined explicitly. Rather, it is obtained by solving a system of linear equations using direct or iterative solvers. Using standard Gaussian elimination or Cholesky method \mathbf{k}_{aa} is decomposed into triangular factors \mathbf{L} , \mathbf{D} and the problem is reduced to solve two triangular systems

$$\mathbf{k}_{aa} = \mathbf{L}\mathbf{D}\mathbf{L}^T . \quad (2.93)$$

By an efficient reordering of nodes the computational labor still increases with an order of $\mathcal{O}(N^{2.33})$ for three dimensional problems (see [Axelsson and Barker, 1984]), where N represents the number of degrees of freedom. Hence, with increasing size of the microstructural problem the computation of \mathbf{k}_{aa}^{-1} becomes more and more expensive. For larger systems the memory requirements for storing the matrix coefficients increases significantly. Regarding realistic microstructures the memory requirements may not be met using standard workstations.

In this work, we compute the macroscopic tangent by numerical linearization around the current macroscopic load step, see Section 4. As proposed by Miehe [1996] the tangent is obtained by numerical differentiation of the macroscopic stress-strain relation. Hence, six additional perturbation load cases are applied to the equilibrated microstructure.

Chapter 3

Numerical Methods

Many time dependent or even just static nonlinear physical problems are described by partial differential equations (PDEs). Basically, there exist several numerical methods for solving PDEs by approximating the solution fields in time and space domain. In this chapter the two numerical methods which are used to solve the governing static equations expressing the physical phenomena of deformation related to this work are shortly described.

3.1 Finite Element Method

In this section the spatial resolution of a static problem by the Finite Element Method (FEM) is considered. In this work, the method is used to solve the macroscopic boundary problem. After introducing the variational formulation of the static equilibrium equation the linearization of a general nonlinear problem is shortly described. Finally, the spatial discretization of a solid body and the iterative solution procedure are depicted. For more detailed information and extensions of the finite element method it is referred to the textbooks of Hughes [2012], Wriggers [2008] or Zienkiewicz and Taylor [2005]. In a more mathematical context see also Oden and Reddy [2012] or Belytschko et al. [2013].

3.1.1 Weak Formulation of the Equilibrium Equations

The strong form of the static equilibrium introduced in (2.13) can be reformulated by the multiplication with a virtual and kinematical admissible displacement test function \boldsymbol{v}

$$G(\boldsymbol{u}, \boldsymbol{v}) = \int_{\Omega} (\operatorname{div} \boldsymbol{\sigma} + \boldsymbol{f}) \cdot \boldsymbol{v} \, dV = 0 . \quad (3.1)$$

The displacements take prescribed values \boldsymbol{u}^0 at the Dirichlet boundary Γ_D of the domain Ω (see Figure 3.1, left) and are defined in the solution space

$$\mathcal{V}^* = \{ \boldsymbol{u} \in H^1(\Omega) : \boldsymbol{u}|_{\Gamma_D} = \boldsymbol{u}^0 \} . \quad (3.2)$$

In the weak formulation the strong form is not required to hold absolutely anymore, but has instead weak solutions in the Sobolev space $H^1(\Omega)$. Similarly, associated with \mathcal{V}^* the function space \mathcal{V}_0 of admissible test functions \boldsymbol{v} is defined

$$\mathcal{V}_0 = \{ \boldsymbol{v} \in H^1(\Omega) : \boldsymbol{v}|_{\Gamma_D} = \mathbf{0} \} . \quad (3.3)$$

In terms of the kinematical relations for small deformations (see Section 2.1) the

strains $\boldsymbol{\varepsilon}$ are related to the displacements \mathbf{u} by

$$\boldsymbol{\varepsilon} = \frac{1}{2} (\text{grad } \mathbf{u} + (\text{grad } \mathbf{u})^T) . \quad (3.4)$$

The constitutive behavior that connects the stresses $\boldsymbol{\sigma}$ with the strains $\boldsymbol{\varepsilon}$ is defined by the general nonlinear relation \mathcal{F}

$$\boldsymbol{\sigma} = \mathcal{F}(\boldsymbol{\varepsilon}(\mathbf{u})) . \quad (3.5)$$

Applying the Gauss theorem and integrating by parts, one obtains the weak form of the static equilibrium equations, also known as the principle of virtual work. The weak form is composed of the internal and external virtual work

$$G(\mathbf{u}, \mathbf{v}) = \underbrace{\int_{\Omega} \boldsymbol{\sigma} : \text{grad } \mathbf{v} \, dV}_{G_{\text{int}}} - \underbrace{\int_{\partial\Omega} \mathbf{t}_0 \cdot \mathbf{v} \, dA - \int_{\Omega} \mathbf{f} \cdot \mathbf{v} \, dV}_{-G_{\text{ext}}} = 0 . \quad (3.6)$$

The gradient of \mathbf{v} can also be interpreted as the variation of the strain tensor $\delta\boldsymbol{\varepsilon}$. The weak form in (3.6) is identical to the first variation of the total potential energy (if such a potential exists) or Gateaux directional derivative, respectively. The Gateaux variation gives the directional derivative of a functional $F : \mathcal{V} \rightarrow \mathbb{R}$ at \mathbf{u} in a direction \mathbf{v} .

A functional $F(\mathbf{u})$ is Gateaux differentiable if there exists a linear functional $DF(\mathbf{u}) \in \mathcal{V}'$ such that for every $\mathbf{v} \in \mathcal{V}$

$$\langle DF(\mathbf{u}), \mathbf{v} \rangle = \lim_{\epsilon \rightarrow 0} \frac{F(\mathbf{u} + \epsilon\mathbf{v}) - F(\mathbf{u})}{\epsilon} = \left. \frac{dF(\mathbf{u} + \epsilon\mathbf{v})}{d\epsilon} \right|_{\epsilon=0} . \quad (3.7)$$

The following notations for the Gateaux differential can also be found in literature

$$\langle DF(\mathbf{u}), \mathbf{v} \rangle = DF(\mathbf{u})(\mathbf{v}) = \delta F(\mathbf{u}; \mathbf{v}) . \quad (3.8)$$

The total potential energy for an elastic static problem is given by

$$\Pi(\mathbf{u}) = \frac{1}{2} \int_{\Omega} \boldsymbol{\sigma} : \boldsymbol{\varepsilon} \, dV - \int_{\partial\Omega} \mathbf{t}_0 \cdot \mathbf{u} \, dA - \int_{\Omega} \mathbf{f} \cdot \mathbf{u} \, dV . \quad (3.9)$$

Using Gateaux derivative the first variation of the total potential energy functional Π at \mathbf{u} in the direction of the variation \mathbf{v} is obtained as

$$\delta\Pi(\mathbf{u}, \mathbf{v}) = \int_{\Omega} \boldsymbol{\sigma} : \text{grad } \mathbf{v} \, dV - \int_{\partial\Omega} \mathbf{t}_0 \cdot \mathbf{v} \, dA - \int_{\Omega} \mathbf{f} \cdot \mathbf{v} \, dV \equiv G(\mathbf{u}, \mathbf{v}) . \quad (3.10)$$

In this regard, the variation \mathbf{v} represents a small kinematically admissible perturbation of the equilibrated solution field \mathbf{u} . The weak formulation in (3.6) is a necessary

condition for the existence of a minimum of the total potential energy

$$\min_{\mathbf{u} \in \mathcal{V}^*} \Pi(\mathbf{u}) \quad \text{with} \quad \delta\Pi(\mathbf{u}, \mathbf{v}) = 0 \quad \text{and} \quad \delta^2\Pi(\mathbf{u}, \mathbf{v}) > 0. \quad (3.11)$$

In the equation above $\delta^2\Pi(\mathbf{u}, \mathbf{v})$ represents the second variation of the potential energy and is obtained by the second Gateaux derivative of the total energy functional. A necessary condition for the existence of a minimum of Π is the positive value of $\delta^2\Pi$. The existence of the minimum characterizes a stable equilibrium state and uniqueness of the solution. The uniqueness is ensured, if the constitutive relation between stress and strains is derived from a convex thermodynamical potential ψ

$$\boldsymbol{\sigma} = \frac{\partial\psi(\boldsymbol{\varepsilon}(\mathbf{u}))}{\partial\boldsymbol{\varepsilon}}. \quad (3.12)$$

3.1.2 Linearized Equilibrium Equations

Dealing with strongly nonlinear problems it is in general advisable to increase the external load progressively and linearize the governing nonlinear differential equations around the particular deformation state. The governing equation is transformed into a system of piecewise linear functions and solved in each load step. The linearized form of the weak formulation G expanded in Taylor series form reads as follows

$$G(\mathbf{u} + \epsilon\mathbf{w}, \mathbf{v}) = G(\mathbf{u}, \mathbf{v}) + \underbrace{\frac{dG(\mathbf{u} + \epsilon\mathbf{w}, \mathbf{v})}{d\epsilon}}_{\delta G(\mathbf{u}, \mathbf{v}, \mathbf{w})} \Big|_{\epsilon=0} \cdot \mathbf{w} + R_n. \quad (3.13)$$

In the linearized form above the second Gateaux differential δG or second variation of the potential energy $\delta^2\Pi(\mathbf{u}, \mathbf{v})$, respectively, occurs. By differentiation of the first variation the second Gateaux differential is obtained for constant external forces in the following form

$$\begin{aligned} \delta G(\mathbf{u}, \mathbf{v}, \mathbf{w}) &= \lim_{\epsilon \rightarrow 0} \frac{G(\mathbf{u} + \epsilon\mathbf{w}, \mathbf{v}) - G(\mathbf{u}, \mathbf{v})}{\epsilon} = \frac{dG(\mathbf{u} + \epsilon\mathbf{w})}{d\epsilon} \Big|_{\epsilon=0} \\ &= \int_{\Omega} \frac{d\boldsymbol{\sigma}(\mathbf{u} + \epsilon\mathbf{w})}{d\epsilon} \Big|_{\epsilon=0} : \boldsymbol{\varepsilon}(\mathbf{w}) \, dV \\ &= \int_{\Omega} \frac{d\mathcal{F}(\boldsymbol{\varepsilon}(\mathbf{u} + \epsilon\mathbf{w}))}{d\epsilon} \Big|_{\epsilon=0} : \boldsymbol{\varepsilon}(\mathbf{v}) \, dV \\ &= \int_{\Omega} \frac{\partial\mathcal{F}(\boldsymbol{\varepsilon}(\mathbf{u} + \epsilon\mathbf{w}))}{\partial\boldsymbol{\varepsilon}(\mathbf{u} + \epsilon\mathbf{w})} \Big|_{\epsilon=0} \frac{d\boldsymbol{\varepsilon}(\mathbf{u} + \epsilon\mathbf{w})}{d\epsilon} \Big|_{\epsilon=0} : \boldsymbol{\varepsilon}(\mathbf{v}) \, dV \\ &= \int_{\Omega} \mathbf{C}(\mathbf{u}) : \boldsymbol{\varepsilon}(\mathbf{w}) : \boldsymbol{\varepsilon}(\mathbf{v}) \, dV. \end{aligned} \quad (3.14)$$

In the equations above the linearization of the stress tensor is written in terms of the linearized tangential material stiffness tensor. It is obtained from the derivative

of the constitutive equation $\mathcal{F}(\boldsymbol{\varepsilon}(\mathbf{u}))$

$$\mathbf{C} = \frac{\partial \mathcal{F}(\boldsymbol{\varepsilon})}{\partial \boldsymbol{\varepsilon}}. \quad (3.15)$$

While for linear elastic material behavior the coefficients of \mathbf{C} are constant and thus independent in variations of \mathbf{u} , in the case of nonlinear material behavior the constitutive equation has to be linearized in each solution iteration. This is the case when the material law is dependent on the current deformation state, as it occurs in strain hardening or softening materials (see Section 2.3). This is even more particular in terms of a multiscale simulation, where the microscopic problem has to be linearized around the current macroscopic deformation state (see Section 4.3).

3.1.3 Spatial Discretization

For the numerical solution of the governing PDE which is transferred in a weak linearized form, the domain Ω of the continuous body is decomposed into small subregions Ω_e (finite elements), see Figure 3.1. The continuous body is approximated

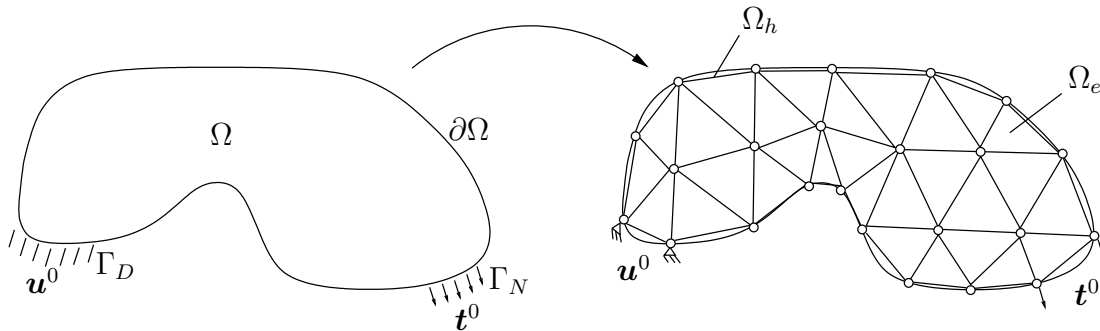


Figure 3.1: Discretization of a body Ω by triangular finite elements Ω_e .

by a discretized domain Ω_h

$$\Omega \approx \Omega_h = \bigcup_{e=1}^{n_e} \Omega_e. \quad (3.16)$$

The exact solution of the field variables are interpolated between discrete points within the finite elements. Thus, the nodal values \mathbf{u}_I of a function $\mathbf{u}(\cdot)$, here the displacements, are approximated by shape functions N_I between the nodes of a finite element

$$\mathbf{u}(\mathbf{x}) \approx \mathbf{u}_h(\mathbf{x}) = \sum_{I=1}^n N_I(\mathbf{x}) \mathbf{u}_I \quad \forall \mathbf{x} \text{ in } \Omega_e. \quad (3.17)$$

Within the isoparametric concept the field variables and the geometric shape of the domain are approximated by the same shape functions

$$\mathbf{x} \approx \mathbf{x}_h = \sum_{I=1}^n N_I \mathbf{x}_I \quad \forall \mathbf{x} \text{ in } \Omega_e . \quad (3.18)$$

The integrals over the domain Ω have the following discretized form

$$\int_{\Omega} (\cdot) dV \approx \int_{\Omega_h} (\cdot) dV = \bigcup_{e=1}^{n_e} \int_{\Omega_e} (\cdot) dV . \quad (3.19)$$

Neglecting body forces ($\mathbf{f} = \mathbf{0}$) the continuous variational formulation of the equilibrium equations introduced in (3.6) reads as follows

$$G(\mathbf{u}, \mathbf{v}) = \int_{\Omega} \boldsymbol{\sigma} : \delta \boldsymbol{\varepsilon} dV - \int_{\partial \Omega} \mathbf{t}_0 \cdot \mathbf{v} dA = 0 . \quad (3.20)$$

The discretized form of the first term in (3.20), the virtual internal work

$$\begin{aligned} G_{\text{int}} &= \int_{\Omega} \boldsymbol{\sigma} : \delta \boldsymbol{\varepsilon} dV \\ &\approx \bigcup_{e=1}^{n_e} \sum_{I=1}^n \mathbf{v}_I^T \underbrace{\int_{\Omega_e} \mathbf{B}_I^T \boldsymbol{\sigma} dV}_{\mathbf{R}_e} = \bigcup_{e=1}^{n_e} \sum_{I=1}^n \mathbf{v}_I^T \mathbf{R}_I = \mathbf{v}^T \mathbf{R} , \end{aligned} \quad (3.21)$$

and the second term, the virtual work of the external loads

$$\begin{aligned} G_{\text{ext}} &= \int_{\partial \Omega^t} \mathbf{t}_0 \cdot \mathbf{v} dA \\ &\approx \bigcup_{e=1}^{n_e} \sum_{I=1}^n \mathbf{v}_I^T \underbrace{\int_{\partial \Omega^t} \mathbf{t}_0 N_I dA}_{\mathbf{P}_e} = \bigcup_{e=1}^{n_e} \sum_{I=1}^n \mathbf{v}_I^T \mathbf{P}_I = \mathbf{v}^T \mathbf{P} \end{aligned} \quad (3.22)$$

are obtained. Thereby the matrix \mathbf{B}_I contains the derivatives of the shape functions N_I of a finite element. The internal and external nodal forces are denoted by \mathbf{R}_I and \mathbf{P}_I , and the sum over the nodal values of each element gives the global force vectors \mathbf{R} and \mathbf{P} .

Remark: In the second part of 3.21 and 3.22 Voigt notation is used. For the sake of simplicity, a special matrix notation is omitted in the following part. Multi dimensional variables, as well as matrices and vectors are indicated with bolt letters.

Hence, the weak formulation of the equilibrium equation in discretized form can be written as

$$G = \bigcup_{e=1}^{n_e} \sum_{I=1}^n \mathbf{v}_I^T (\mathbf{R}_I(\mathbf{u}_I) - \mathbf{P}_I) = \mathbf{v}^T (\mathbf{R}(\mathbf{u}) - \mathbf{P}) = 0 . \quad (3.23)$$

For any admissible virtual test function \mathbf{v} the equation above simplifies to an equilibrium of the internal $\mathbf{R}(\mathbf{u})$ and external force vector \mathbf{P}

$$\mathbf{R}(\mathbf{u}) - \mathbf{P} = \mathbf{0} . \quad (3.24)$$

The discretized field variables in matrix form are given by

$$\boldsymbol{\varepsilon}(\Delta\mathbf{u}) = \Delta\boldsymbol{\varepsilon}(\mathbf{u}) = \sum_{I=1}^n \mathbf{B}_I \Delta\mathbf{u}_I \quad \boldsymbol{\varepsilon}(\mathbf{v}) = \sum_{I=1}^n \mathbf{B}_I \mathbf{v}_I , \quad (3.25)$$

and we end up with the discrete linearized variational formulation of the incremental static equilibrium equations

$$\begin{aligned} \Delta G &= \delta G(\mathbf{u}, \mathbf{v}, \Delta\mathbf{u}) = \int_{\Omega} \mathbf{C}(\mathbf{u}) \Delta\boldsymbol{\varepsilon}(\mathbf{u}) \boldsymbol{\varepsilon}(\mathbf{v}) \, dV \Delta\mathbf{u} \\ &\approx \bigcup_{e=1}^{n_e} \sum_{I=1}^n \sum_{J=1}^n \mathbf{v}_I^T \underbrace{\int_{\Omega^e} \mathbf{B}_I^T \mathbf{C} \mathbf{B}_J \, dV}_{\mathbf{K}_{IJ}^e} \Delta\mathbf{u}_J . \end{aligned} \quad (3.26)$$

In the equation above an incremental increase of G by ΔG with an incremental increase of the solution \mathbf{u} by $\Delta\mathbf{u}$ is considered. Furthermore, the element stiffness matrix \mathbf{K}_{IJ}^e connecting the nodes I and J of a finite element is introduced. The global stiffness matrix is assembled from the element stiffness matrices

$$\mathbf{K} = \bigcup_{e=1}^{n_e} \mathbf{K}^e . \quad (3.27)$$

3.1.4 Iterative Solution Procedure

Finally the following nonlinear set of equations has to be solved iteratively

$$\mathbf{G}(\mathbf{u}) = \mathbf{R}(\mathbf{u}) - \mathbf{P} = \mathbf{0} . \quad (3.28)$$

In the equation above $\mathbf{R}(\mathbf{u})$ covers the internal forces which are dependent on the deformation state and the constant external loads are represented by the vector \mathbf{P} . The most popular method for solving systems of nonlinear equations is the Newton-Raphson method. For obtaining the unknown displacement field iteratively the following approximated Taylor series based on known conditions is used

$$\mathbf{G}(\mathbf{u}^{i+1}, \lambda) = \mathbf{G}(\mathbf{u}^i, \lambda) + \delta\mathbf{G}(\mathbf{u}^i, \lambda) \Delta\mathbf{u}^{i+1} \stackrel{!}{=} \mathbf{0} . \quad (3.29)$$

Thereby the load factor λ enables the gradual increase of the external force $\mathbf{G} = \mathbf{R} - \lambda\mathbf{P}$. Using the linearized form $\delta\mathbf{G}$ defined in (3.26) and the global stiffness matrix \mathbf{K} according to (3.27) the new increment of the unknown displacement field

$\Delta \mathbf{u}^{i+1}$ can be computed with

$$\mathbf{K}^i \Delta \mathbf{u}^{i+1} = \mathbf{G}^i . \quad (3.30)$$

In addition, suitable displacement boundary conditions are incorporated at the boundary nodes to fix possible rigid body modes. Hence, the system matrix \mathbf{K} becomes positive definite and the linearized system can be solved for the current load factor λ within the following algorithm

1. Start	$\mathbf{u}^i = \mathbf{u}^0$
2. Assemble	$\mathbf{G}^i = \mathbf{G}(\mathbf{u}^i, \lambda), \quad \mathbf{K}(\mathbf{u}^i)$
3. Solve	$\mathbf{K}^i \Delta \mathbf{u}^{i+1} = -\mathbf{G}^i$
4. Update	$\mathbf{u}^{i+1} = \mathbf{u}^i + \Delta \mathbf{u}^{i+1}$
5. Check if	$\ \mathbf{G}^{i+1}\ \geq \text{TOL}$ then $i = i + 1$ return to 2

The linearized set of equations (step 3) can be solved directly by standard Gaussian elimination or Cholesky method. Dealing with larger algebraic systems, iterative methods, like e.g. the conjugate gradient method (CG), the biconjugate gradient stabilized method (BiCGSTAB) or multigrid methods (MG) are used in combination with suitable preconditioning methods.

3.2 Lippmann-Schwinger Equation and Fast Fourier Transformation

Considering microstructures with complex geometric shape difficulties may arise during the meshing of these structures. Microstructural images, which are discretized by cubic voxel cells, can be used directly. In this context, methods using Fast (FFT) or Discrete Fourier Transforms (DFT) were introduced by Moulinec and Suquet [1994] and Müller [1996]. These methods operate on regular spatial grids and can directly be applied to analyze cubic volume elements. The problem is solved iteratively and, in contrary to the standard finite element method does not require the assemblage and storage of a global stiffness matrix. The method described in this section is used to solve periodic microstructural unit cell problems.

3.2.1 Periodic Strain Field and Local Boundary Value Problem

In terms of a homogenization problem the macroscopic scale is considered as homogeneous and its effective constitutive response can be obtained by well-separated local unit cell problems. All the heterogeneities are transferred into the microscopic problem and from the macroscopic point of view the samples are homogenized,

so that a smeared macroscopic response is obtained. Composites with periodic microstructure can be represented by a periodic arrangement of these similar unit cells. During macroscopic deformation the unit cells are subjected to displacements on the boundary which result from the macroscopic point of view in a homogeneous strain over the homogenized microscopic domain ω . Due to the local heterogeneous setting of the microstructure the microscopic strain field $\boldsymbol{\varepsilon}(\mathbf{x})$ strongly varies between the microscopic points \mathbf{x} . This local strain field can be decomposed into a spatially constant overall strain \mathbf{E} which would act in a completely homogeneous microstructure and a fluctuation or correction field $\boldsymbol{\varepsilon}^*(\mathbf{x})$ that accounts for the heterogeneities of the microstructure

$$\boldsymbol{\varepsilon}(\mathbf{x}) = \mathbf{E} + \boldsymbol{\varepsilon}^*(\mathbf{x}) . \quad (3.31)$$

The strain fluctuation field $\boldsymbol{\varepsilon}(\mathbf{u}^*(\mathbf{x}))$ is compatible with the fluctuating displacement field $\mathbf{u}^*(\mathbf{x})$ and is calculated according to the kinematical relations by the symmetric part of the displacement gradient

$$\boldsymbol{\varepsilon}(\mathbf{u}^*(\mathbf{x})) = \frac{1}{2} (\nabla \mathbf{u}^*(\mathbf{x}) + (\nabla \mathbf{u}^*(\mathbf{x}))^T) . \quad (3.32)$$

The mean deformation of the unit cell is obtained from the constant macroscopic strain within the relation $\mathbf{E} \cdot \mathbf{x}$ and hence, the entire displacement field in the microscopic domain reads as follows:

$$\mathbf{u}(\mathbf{x}) = \mathbf{E} \cdot \mathbf{x} + \mathbf{u}^*(\mathbf{x}) . \quad (3.33)$$

The coupling of periodic unit cells is ensured by assuming identical values for the components of $\mathbf{u}^*(\mathbf{x})$ on opposite boundaries of the microscopic domain $\partial\omega$

$$\mathbf{u}^*(\mathbf{x}) \text{ periodic } \quad \mathbf{x} \text{ on } \partial\omega . \quad (3.34)$$

The periodic nature of \mathbf{u}^* and $\boldsymbol{\varepsilon}(\mathbf{u}^*)$, respectively, implies that the averages over the whole microscopic domain ω vanish

$$\langle \mathbf{u}^* \rangle = \frac{1}{|\omega|} \int_{\omega} \mathbf{u}^* \, dv = \mathbf{0} , \quad (3.35)$$

$$\langle \boldsymbol{\varepsilon}(\mathbf{u}^*) \rangle = \frac{1}{|\omega|} \int_{\omega} \boldsymbol{\varepsilon}(\mathbf{u}^*) \, dv = \mathbf{0} . \quad (3.36)$$

Consequently, a compatible displacement field from unit cell to unit cell over the macroscopic domain is obtained. Furthermore, the equilibrium condition (here in the absence of volume forces) has to be fulfilled in each point of the microscopic domain

$$\operatorname{div} \boldsymbol{\sigma}(\mathbf{x}) = \mathbf{0} \quad \mathbf{x} \text{ in } \omega . \quad (3.37)$$

To satisfy the equilibrium throughout the global entire macroscopic periodic composite, the interfaces between periodic unit cells have to be in equilibrium. This implies, that tractions \mathbf{t} on opposite boundaries have to cancel each other and thus,

to be opposite or anti-periodic on the boundaries

$$\mathbf{t}(\mathbf{x}) = \boldsymbol{\sigma}(\mathbf{x}) \cdot \mathbf{n}(\mathbf{x}) \quad \text{anti-periodic } \mathbf{x} \text{ on } \partial\omega. \quad (3.38)$$

Thus, the required periodicity of the stress tensor $\boldsymbol{\sigma}$ is ensured by the opposite direction of the normal vectors \mathbf{n} on opposite boundary surfaces (see Figure 3.2). In

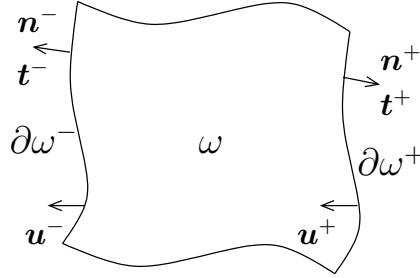


Figure 3.2: Periodic unit cell with periodic displacements \mathbf{u} and anti-periodic tractions \mathbf{t} on opposite boundaries $\partial\omega^-$ and $\partial\omega^+$.

the following the microscopic boundary value problem is summarized by considering a cubic unit cell with the domain ω which is subjected to a prescribed macroscopic constant strain \mathbf{E} . The fluctuating solution field $\mathbf{u}^*(\mathbf{x})$ has to be find such that,

$$\operatorname{div} \boldsymbol{\sigma}(\mathbf{x}) = \mathbf{0} \quad \mathbf{x} \text{ in } \omega, \quad (3.39a)$$

$$\boldsymbol{\sigma}(\mathbf{x}) = \mathbf{c}(\mathbf{x}) : \boldsymbol{\varepsilon}(\mathbf{x}) \quad \mathbf{x} \text{ in } \omega, \quad (3.39b)$$

$$\boldsymbol{\varepsilon}(\mathbf{x}) = \mathbf{E} + \frac{1}{2} (\nabla \mathbf{u}^*(\mathbf{x}) + (\nabla \mathbf{u}^*(\mathbf{x}))^T) \quad \mathbf{x} \text{ in } \omega, \quad (3.39c)$$

$$\mathbf{u}^*(\mathbf{x}) \text{ periodic} \quad \mathbf{x} \text{ on } \partial\omega, \quad (3.39d)$$

$$\boldsymbol{\sigma}(\mathbf{x}) \cdot \mathbf{n}(\mathbf{x}) \text{ anti-periodic} \quad \mathbf{x} \text{ on } \partial\omega. \quad (3.39e)$$

In the equations above linear elastic material behavior and periodic boundary conditions on $\partial\omega$ are assumed.

3.2.2 Lippmann-Schwinger Equation and Equivalent Boundary Value Problem

Due to the heterogeneities occurring on the microscale the local stiffness tensor $\mathbf{c}(\mathbf{x})$ varies between the local points \mathbf{x} . This heterogeneous character of the local stiffness $\mathbf{c}(\mathbf{x})$ represents the main complexity of the problem according to (3.39). In the context of a finite element framework locally strongly varying stiffness contrasts between local material points \mathbf{x} lead to a large condition number of the global matrix \mathbf{K} (see Section 3.1) and hence, makes it difficult to solve with standard methods. To overcome this problem, equivalent formulations of the governing equations are used in many homogenization approaches. The idea of introducing a homogeneous reference medium to solve complex heterogeneous micromechanical problems in a

homogeneous setting goes back to Eshelby [1957]. He considered the heterogeneity of an inclusion by an equivalent eigenstrain transformation and solved the original inhomogeneous problem in an auxiliary homogeneous medium.

In a more general setting Dederichs and Zeller [1973] established a method for disordered or heterogeneous materials by reformulating the heterogeneous elastic problem stated in (3.39). The method which was introduced in a homogenization context was extended by Zeller and Dederichs [1973] and Kröner [1977] to estimate bounds for the effective elastic constants of polycrystals. The authors established an auxiliary problem formulated in a homogeneous linear elastic medium to eliminate the local dependence of the stiffness $\mathbf{c}(\mathbf{x})$.

A homogeneous reference material with the spatially constant elastic stiffness \mathbf{C}^0 is defined and the local stress field reads as follows:

$$\boldsymbol{\sigma}(\mathbf{x}) = \mathbf{C}^0 : \boldsymbol{\varepsilon}(\mathbf{x}) + \boldsymbol{\tau}(\mathbf{x}) . \quad (3.40)$$

The polarization stress $\boldsymbol{\tau}(\mathbf{x})$ expresses the difference between the stress states in the homogeneous auxiliary problem and the initial heterogeneous problem. It is given by:

$$\boldsymbol{\tau}(\mathbf{x}) = \underbrace{(\mathbf{c}(\mathbf{x}) - \mathbf{C}^0)}_{\delta\mathbf{c}(\mathbf{x})} : \boldsymbol{\varepsilon}(\mathbf{x}) = \delta\mathbf{c}(\mathbf{x}) : (\boldsymbol{\varepsilon}^*(\mathbf{x}) + \mathbf{E}) , \quad (3.41)$$

where $\boldsymbol{\tau}(\mathbf{x})$ depends on the solution field $\mathbf{u}^*(\mathbf{x})$ and thus, in the case of nonlinear material behavior, depends nonlinear on the fluctuation field $\mathbf{u}^*(\mathbf{x})$. The governing differential equation (3.39a)

$$\operatorname{div} \boldsymbol{\sigma}(\mathbf{x}) = \operatorname{div} (\mathbf{c}(\mathbf{x}) : \boldsymbol{\varepsilon}(\mathbf{x})) = \mathbf{0}, \quad \mathbf{x} \text{ in } \omega , \quad (3.42)$$

is replaced by the following equivalent equation

$$\operatorname{div} (\mathbf{C}^0 : \boldsymbol{\varepsilon}(\mathbf{x}) + \boldsymbol{\tau}(\mathbf{x})) = \mathbf{0}, \quad \mathbf{x} \text{ in } \omega . \quad (3.43)$$

Thus, the equivalent microscopic boundary problem for linear elastic material behavior according to (3.39) reads as follows:

$$\operatorname{div} (\mathbf{C}^0 : \boldsymbol{\varepsilon}(\mathbf{x}) + \boldsymbol{\tau}(\mathbf{x})) = \mathbf{0} \quad \mathbf{x} \text{ in } \omega , \quad (3.44a)$$

$$\operatorname{div} (\mathbf{C}^0 : \boldsymbol{\varepsilon}(\mathbf{x})) = -\operatorname{div} \boldsymbol{\tau}(\mathbf{x}) \quad \mathbf{x} \text{ in } \omega ,$$

$$\boldsymbol{\sigma}(\mathbf{x}) = \mathbf{C}^0 : \boldsymbol{\varepsilon}(\mathbf{x}) + \boldsymbol{\tau}(\mathbf{x}) \quad \mathbf{x} \text{ in } \omega , \quad (3.44b)$$

$$\boldsymbol{\varepsilon}(\mathbf{x}) = \mathbf{E} + \frac{1}{2} (\nabla \mathbf{u}^*(\mathbf{x}) + (\nabla \mathbf{u}^*(\mathbf{x}))^T) \quad \mathbf{x} \text{ in } \omega , \quad (3.44c)$$

$$\mathbf{u}^*(\mathbf{x}) \text{ periodic} \quad \mathbf{x} \text{ on } \partial\omega , \quad (3.44d)$$

$$\boldsymbol{\sigma}(\mathbf{x}) \cdot \mathbf{n}(\mathbf{x}) \text{ anti-periodic} \quad \mathbf{x} \text{ on } \partial\omega . \quad (3.44e)$$

In the equivalent problem stated above the complexity of the heterogeneous problem is transferred into the polarization field $\boldsymbol{\tau}(\mathbf{x})$. The divergence of $\boldsymbol{\tau}$ can be interpreted

as a distributed body force acting in the whole domain ω

$$\mathbf{f}(\mathbf{x}) = \operatorname{div} \boldsymbol{\tau}(\mathbf{x}), \quad \mathbf{x} \text{ in } \omega. \quad (3.45)$$

Hence, the problem reduces to find the fluctuation field $\mathbf{u}^*(\mathbf{x})$ in an equilibrated homogeneous medium with constant stiffness \mathbf{C}^0 subjected to the macroscopic strain \mathbf{E} and a corresponding initial polarization stress field $\boldsymbol{\tau}(\mathbf{x})$, see Figure 3.3. The

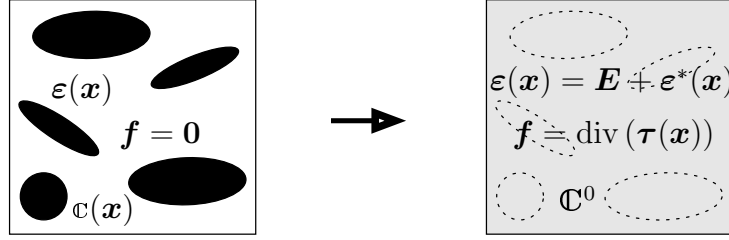


Figure 3.3: Heterogeneous problem (left) and homogeneous reference problem subjected to a body force $\mathbf{f}(\mathbf{x})$ (right).

solution of such problems can be directly expressed by applying a so-called Green's operator $\boldsymbol{\Gamma}^0$ which is associated to the reference material (see Zeller and Dederichs [1973]). The fluctuating strain field $\boldsymbol{\varepsilon}^*$ is obtained by convolution of the Green's operator with the stress polarization $\boldsymbol{\tau}$

$$\boldsymbol{\varepsilon}(\mathbf{u}^*(\mathbf{x})) = (\boldsymbol{\Gamma}^0 * \boldsymbol{\tau})(\mathbf{x}). \quad (3.46)$$

The Green's operator $\boldsymbol{\Gamma}^0$ has a nonlocal character and couples two points \mathbf{x} and \mathbf{y} of the micro domain. The convolution denoted by '*' in (3.46) is defined by

$$(\boldsymbol{\Gamma}^0 * \boldsymbol{\tau})(\mathbf{x}) := \int_{\omega} \boldsymbol{\Gamma}^0(\mathbf{x}, \mathbf{y}) : \boldsymbol{\tau}(\mathbf{y}) \, d\mathbf{y}. \quad (3.47)$$

The solution for the total strain field can be written in the following integral equation:

$$\boldsymbol{\varepsilon}(\mathbf{x}) = \mathbf{E} - \int_{\omega} \boldsymbol{\Gamma}^0(\mathbf{x}, \mathbf{y}) : \boldsymbol{\tau}(\mathbf{y}) \, d\mathbf{y}. \quad (3.48)$$

This type of integral equation is referred to as Lippmann-Schwinger equation in elasticity. The formulation is originally attributed to Lippmann and Schwinger [1950] in the context of the theory of scattering in quantum mechanics. The authors proposed an equivalent integral equation as an alternative to the direct solution of the Schrödinger differential equation describing mechanics of molecular systems on the atomistic level. Later, Zeller and Dederichs [1973] applied this method to reformulate the governing differential equation of heterogeneous elasticity problems on the continuum level. In the regard of the equivalent inclusion method Green's operator was introduced by Mura [1987].

Lippmann-Schwinger Equation for Nonlinear Material Behavior

Dealing with nonlinear material behavior, the constitutive equation for a linear elastic material

$$\boldsymbol{\sigma} = \mathbf{c}(\mathbf{x}) : \boldsymbol{\varepsilon}(\mathbf{x}) , \quad (3.49)$$

has to be replaced by a nonlinear stress-strain relation and possibly additional internal history variables $\mathcal{I}(\mathbf{x})$, like e.g. the plastic strain $\boldsymbol{\varepsilon}_p(\mathbf{x})$, the hardening $r(\mathbf{x})$ or damage variable $d(\mathbf{x})$

$$\boldsymbol{\sigma}(\mathbf{x}) = \mathcal{F}(\boldsymbol{\varepsilon}(\mathbf{x}), \mathcal{I}(\mathbf{x})) . \quad (3.50)$$

The stress polarization $\boldsymbol{\tau}$ according to Equation (3.41) reads

$$\boldsymbol{\tau}(\mathbf{x}) = \boldsymbol{\sigma}(\boldsymbol{\varepsilon}(\mathbf{x}), \mathcal{I}(\mathbf{x})) - \mathbf{C}^0 : \boldsymbol{\varepsilon}(\mathbf{x}) . \quad (3.51)$$

The solution of the nonlinear problem according to Equation (3.48) turns into the following form:

$$\boldsymbol{\varepsilon}(\mathbf{x}) = \mathbf{E} - \int_{\omega} \boldsymbol{\Gamma}^0(\mathbf{x}, \mathbf{y}) : (\boldsymbol{\sigma}(\boldsymbol{\varepsilon}(\mathbf{x}), \mathcal{I}(\mathbf{x})) - \mathbf{C}^0 : \boldsymbol{\varepsilon}(\mathbf{x})) \, d\mathbf{y} . \quad (3.52)$$

The nonlinear stress-strain relation also implies a nonlinear the polarization stress-strain relation. The entire equivalent microscopic boundary value problem according to Equations (3.44) for nonlinear material behavior reads as follows:

$$\operatorname{div}(\boldsymbol{\sigma}(\boldsymbol{\varepsilon}(\mathbf{x}), \mathcal{I}(\mathbf{x}))) = \mathbf{0} \quad \mathbf{x} \text{ in } \omega , \quad (3.53a)$$

$$\boldsymbol{\sigma}(\mathbf{x}) = \mathcal{F}(\boldsymbol{\varepsilon}(\mathbf{x}), \mathcal{I}(\mathbf{x})) \quad \mathbf{x} \text{ in } \omega \quad (3.53b)$$

$$\boldsymbol{\varepsilon}(\mathbf{x}) = \mathbf{E} + \frac{1}{2} (\nabla \mathbf{u}^*(\mathbf{x}) + (\nabla \mathbf{u}^*(\mathbf{x}))^T) \quad \mathbf{x} \text{ in } \omega , \quad (3.53c)$$

$$\mathbf{u}^*(\mathbf{x}) \text{ periodic} \quad \mathbf{x} \text{ on } \partial\omega , \quad (3.53d)$$

$$\boldsymbol{\sigma}(\mathbf{x}) \cdot \mathbf{n}(\mathbf{x}) \text{ anti-periodic} \quad \mathbf{x} \text{ on } \partial\omega , . \quad (3.53e)$$

The stiffness of the reference material \mathbf{C}^0 still remains constant, and thus, the solution of the nonlinear problem can still be expressed in terms of the Green's operator $\boldsymbol{\Gamma}^0$ which is associated to the constant, homogeneous reference material. Solving the Lippmann-Schwinger equation in the framework of a numerical scheme (see Section 3.2.6), the nonlinear computation is decomposed in several time steps, or load increments, respectively. The stiffness of the reference material and the associated Green's operator are updated at the beginning of each time step for obtaining a better convergence behavior.

In this work a linear elastic and a coupled elasto-plastic damage model described in Section 2.3 are implemented in the framework of a three dimensional elasticity solver.

3.2.3 Green's Operator in Bounded Domains

The fourth order Green's operator Γ^0 in Equation (3.48) is obtained from a second order Green's operator \mathbf{G}^0 , also referred to as Green's function, according to Brisard [2011] in index notation given as:

$$4\Gamma_{ijkl}^0(\mathbf{x}, \mathbf{y}) = -\frac{\partial^2 G_{ik}^0}{\partial x_j \partial y_l}(\mathbf{x}, \mathbf{y}) + \frac{\partial^2 G_{il}^0}{\partial x_j \partial y_k}(\mathbf{x}, \mathbf{y}) + \frac{\partial^2 G_{jk}^0}{\partial x_i \partial y_l}(\mathbf{x}, \mathbf{y}) + \frac{\partial^2 G_{jl}^0}{\partial x_k \partial y_i}(\mathbf{x}, \mathbf{y}) . \quad (3.54)$$

The Green's operator \mathbf{G}^0 of the homogeneous medium \mathbb{C}^0 has the following properties

$$\mathbb{C}_{ijkl}^0 G_{km,lj}^0(\mathbf{x}, \mathbf{y}) + \delta_{im} \delta(\mathbf{x} - \mathbf{y}) = 0 , \quad (3.55)$$

where δ_{im} is the Kronecker symbol, and $\delta(\mathbf{x} - \mathbf{y})$ is the Dirac delta distribution. Following Brisard [2011] the interpretation of the second order Green's operator \mathbf{G}^0 can be exemplified by considering a bounded domain ω . The homogeneous body with the material stiffness \mathbb{C}^0 is subjected to a vector point force \mathbf{F} at the local point \mathbf{y} according to Figure 3.4.

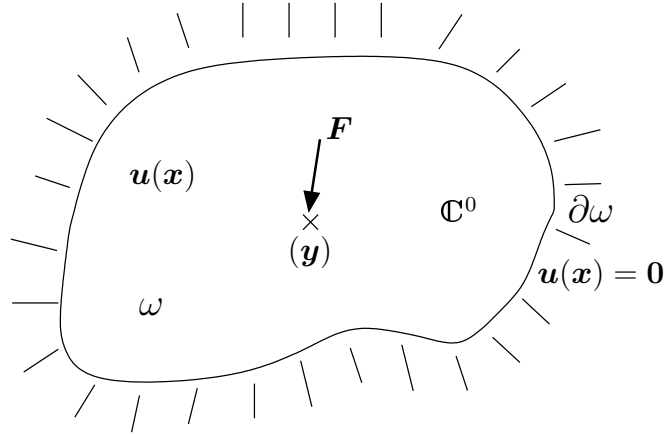


Figure 3.4: Homogeneous domain ω subjected to a vector point force \mathbf{F} at the local point \mathbf{y} and the Dirichlet boundary condition $\mathbf{u}(\mathbf{x}) = \mathbf{0}$ on $\partial\omega$.

The boundaries $\partial\omega$ are subjected to homogeneous Dirichlet conditions

$$\mathbf{u}(\mathbf{x}) = \mathbf{0} , \quad \mathbf{x} \text{ on } \partial\omega , \quad (3.56)$$

the constitutive behavior is assumed to be linear elastic

$$\boldsymbol{\sigma} = \mathbb{C}^0 : \boldsymbol{\varepsilon}(\mathbf{x}) , \quad (3.57)$$

and thus, the response of the system is governed by the following differential equation:

$$\text{div}(\mathbb{C}^0 : \boldsymbol{\varepsilon}(\mathbf{x})) + \delta(\mathbf{x} - \mathbf{y})\mathbf{F} = \mathbf{0} . \quad (3.58)$$

Here δ is the Dirac distribution which describes the local point character of the force \mathbf{F} and is defined by the normalized distribution in the domain ω

$$\int_{\omega} \delta(\mathbf{x} - \mathbf{y}) \, d\mathbf{y} = 1, \quad (3.59)$$

and hence, the distribution of the point force can be written as

$$\mathbf{f}(\mathbf{x}) = \delta(\mathbf{x} - \mathbf{y}) \mathbf{F}. \quad (3.60)$$

The solution field $u_i(\mathbf{x})$ can be expressed in the form

$$u_i(\mathbf{x}) = G_{ik}^0(\mathbf{x}, \mathbf{y}) F_k. \quad (3.61)$$

In the equation above G_{ik}^0 is the Green's operator describing the displacement component u_i at point \mathbf{x} in direction of x_i due to the applied unit force at point \mathbf{y} in direction x_k . In other words, the Green's operator expresses the fundamental (displacement) solution in a homogeneous elastic medium. In the bounded domain ω with zero displacement condition on the boundary $\partial\omega$ the Green's operator has to vanish on the boundary

$$\mathbf{G}^0(\mathbf{x}, \mathbf{y}) = \mathbf{0}, \quad \mathbf{x} \text{ on } \partial\omega. \quad (3.62)$$

Considering the more general case when the homogeneous body ω is subjected to a body force \mathbf{f} , instead of the concentrated point force \mathbf{F} used in the example above. The body force can be seen as a superposition of the elementary case (3.60)

$$\int_{\omega} \mathbf{f}(\mathbf{y}) \delta(\mathbf{x} - \mathbf{y}) \, d\mathbf{y} = \mathbf{f}(\mathbf{x}), \quad (3.63)$$

and, one obtains the solution field by superimposing the previous basic solutions (3.61)

$$\mathbf{u}(\mathbf{x}) = \int_{\omega} \mathbf{G}^0(\mathbf{x}, \mathbf{y}) \cdot \mathbf{f}(\mathbf{y}) \, d\mathbf{y}. \quad (3.64)$$

In the problem stated in Equation (3.44a) one is interested in an equilibrated solution field \mathbf{u} for the elastic body that is subjected to a polarization stress field $\boldsymbol{\tau}$. In order to establish a connection to the problem stated above, the right-hand side of Equation (3.44a), i.e. the divergence of the polarization or eigenstress field, is interpreted as a body force $\mathbf{f}(\mathbf{x})$

$$\mathbf{f}(\mathbf{x}) = \operatorname{div} \boldsymbol{\tau}(\mathbf{x}). \quad (3.65)$$

One obtains the solution with zero displacement conditions on the boundaries by the following equation:

$$\mathbf{u}(\mathbf{x}) = \int_{\omega} \mathbf{G}^0(\mathbf{x}, \mathbf{y}) \cdot \operatorname{div} \boldsymbol{\tau}(\mathbf{y}) \, d\mathbf{y}. \quad (3.66)$$

By partial integration and subsequent differentiation the strain field is given by the fourth order Green's operator

$$\boldsymbol{\varepsilon}(\mathbf{x}) = \int_{\omega} \boldsymbol{\Gamma}^0(\mathbf{x}, \mathbf{y}) : \boldsymbol{\tau}(\mathbf{y}) \, d\mathbf{y} . \quad (3.67)$$

Applying a macroscopic strain \mathbf{E} on the boundary, instead of zero displacements

$$\mathbf{u}(\mathbf{x}) = \mathbf{E} \cdot \mathbf{x}, \quad \mathbf{x} \text{ on } \partial\omega , \quad (3.68)$$

the resulting strain field reads as follows

$$\boldsymbol{\varepsilon}(\mathbf{x}) = \mathbf{E} - \int_{\omega} \boldsymbol{\Gamma}^0(\mathbf{x}, \mathbf{y}) : \boldsymbol{\tau}(\mathbf{y}) \, d\mathbf{y} . \quad (3.69)$$

The meaning becomes more transparent by writing (3.69) in index notation

$$\varepsilon_{ij}(\mathbf{x}) = E_{ij} - \int_{\omega} \Gamma_{ijkl}^0(\mathbf{x}, \mathbf{y}) : \tau_{kl}(\mathbf{y}) \, d\mathbf{y} . \quad (3.70)$$

The operator Γ_{ijkl}^0 gives the strain components ij at point \mathbf{x} due to the applied stress components kl at \mathbf{y} . The operator $\boldsymbol{\Gamma}^0$ does not depend on the fluctuating quantities, but only on the stiffness of the homogeneous linear elastic reference material \mathbf{C}^0 and given boundary conditions.

In the previous part the meaning of the Green's operator is explained for bounded domains with displacement free surfaces. The original contributions of Zeller and Dederichs [1973], Dederichs and Zeller [1973] and Kröner [1977] are also referred to bounded domains with stress or displacement free boundaries. For more details concerning Green operators for bounded domains see Kröner [1990].

Mura [1987] introduced the Green's operator in an infinitely extended material subjected to a given periodic eigenstrain distribution. In order to establish a connection to the present homogenization problem, the eigenstrain distribution can be caused by material heterogeneities, similar to the polarization stress $\boldsymbol{\tau}$ introduced in this chapter. Due to periodicity the applied eigenstrain distribution can be expressed in Fourier series form and the elastic solution field is obtained by superposition of elementary solutions. The Green's operator \mathbf{G}^∞ as the fundamental solution of this problem is expressed in Fourier space. Basically, due to the non-local character a direct expression of Green operators for periodic problems can be given more easily in Fourier space and will be given in Section 3.2.4.

3.2.4 Lippmann-Schwinger Equation in Fourier Space

The solution of a periodic boundary value problem according to Equations (3.44) or (3.53a), respectively, can be obtained using Fourier transforms. As introduced by Mura [1987] continuous Fourier transforms can be used to solve eigenstrain problems in heterogeneous linear elastic bodies. In this context methods using Fast (FFT) or

Discrete Fourier Transforms (DFT) were introduced by Moulinec and Suquet [1994] and Müller [1996] to solve homogenization problems of heterogeneous materials.³ The partial differential equation describing the elastic problem which is reformulated into an integral equation of Lippmann-Schwinger type is transferred in Fourier space. Fourier series are used to express the corresponding field variables. In Fourier space the discrete second order PDE's turn in a system of linear equations which are formally much easier to solve.

The elastic fields according to Equations (3.44) or (3.53a) are periodic and can be easily transformed in Fourier space. A local micro field $\mathbf{u}(\mathbf{x})$ is given in the following Fourier integral form:

$$\hat{\mathbf{u}}(\boldsymbol{\xi}) = \frac{1}{|\omega|} \int_{\omega} \mathbf{u}(\mathbf{x}) \exp(-i\boldsymbol{\xi} \cdot \mathbf{x}) \, d\mathbf{x} , \quad (3.71)$$

with the complex number $i = \sqrt{-1}$. In the following, $\hat{\mathbf{u}}(\cdot)$ denotes a function in Fourier space and $\boldsymbol{\xi}$ is the Fourier space variable or spatial frequency corresponding to the coordinates \mathbf{x} . The inverse Fourier transformation of the function $\hat{\mathbf{u}}(\boldsymbol{\xi})$ is given by

$$\mathbf{u}(\mathbf{x}) = \int_{\omega} \hat{\mathbf{u}}(\boldsymbol{\xi}) \exp(i\boldsymbol{\xi} \cdot \mathbf{x}) \, d\boldsymbol{\xi} . \quad (3.72)$$

An important issue of the Fourier expression is given by the following definition:

$$\hat{\mathbf{u}}(\boldsymbol{\xi} = \mathbf{0}) = \frac{1}{|\omega|} \int_{\omega} \mathbf{u}(\mathbf{x}) \, d\mathbf{x} . \quad (3.73)$$

The expression above means that the value of the function in Fourier space at the point $\boldsymbol{\xi} = \mathbf{0}$ equals to the average of the function $\mathbf{u}(\mathbf{x})$ over the whole domain ω in the real space. Furthermore, the spatial derivative of a function in the real space $\text{grad } \mathbf{u}(\mathbf{x})$, is given in Fourier space by a simple multiplication:

$$\text{grad } \mathbf{u}(\mathbf{x}) = \frac{\partial \mathbf{u}(\mathbf{x})}{\partial \mathbf{x}} = i \hat{\mathbf{u}}(\boldsymbol{\xi}) \boldsymbol{\xi} . \quad (3.74)$$

Thus, the equilibrium condition (3.44a) and the constitutive equation (3.44b) have the following form in Fourier space:

$$\hat{\sigma}_{kl}(\boldsymbol{\xi}) = i \mathbb{C}_{klmn}^0 \xi_n \hat{u}_m^*(\boldsymbol{\xi}) + \hat{\tau}_{kl}(\boldsymbol{\xi}) \quad (3.75)$$

$$i \hat{\sigma}_{kl}(\boldsymbol{\xi}) \xi_l = \mathbf{0} . \quad (3.76)$$

Substituting $\hat{\sigma}_{kl}$ in the equilibrium equation gives

$$\mathbb{C}_{klmn}^0 \xi_l \xi_n \hat{u}_m^*(\boldsymbol{\xi}) = i \hat{\tau}_{kl}(\boldsymbol{\xi}) \xi_l . \quad (3.77)$$

³FFT represents a fast algorithm for computing discrete Fourier transforms and is due to its efficiency more frequently used. The number of computations is reduced by factorizing the DFT matrix.

Introducing the inverse second order Green's operator $(\hat{G}^0)_{km}^{-1}(\boldsymbol{\xi})$ of the homogeneous material

$$(\hat{G}^0)_{km}^{-1}(\boldsymbol{\xi}) = \mathbb{C}_{klmn}^0 \xi_l \xi_n, \quad (3.78)$$

the fluctuating displacement solution is obtained as

$$\hat{u}_m^*(\boldsymbol{\xi}) = \hat{G}_{mk}^0(\boldsymbol{\xi}) i \hat{\tau}_{kl}(\boldsymbol{\xi}) \xi_l = \frac{i}{2} \left(\hat{G}_{mk}^0(\boldsymbol{\xi}) \xi_l + \hat{G}_{ml}^0(\boldsymbol{\xi}) \xi_k \right) \hat{\tau}_{kl}(\boldsymbol{\xi}), \quad (3.79)$$

The kinematical compatibility conditions of the fluctuating displacement field u_m^* according to Equation (3.44c) reads in Fourier space

$$\hat{\varepsilon}_{kl}(\mathbf{u}^*) = \frac{i}{2} (\xi_k \hat{u}_l^* + \xi_l \hat{u}_k^*). \quad (3.80)$$

Using the definition of the fourth order Green's operator in Equation (3.54) in Fourier space

$$\hat{\Gamma}_{klmn}^0(\boldsymbol{\xi}) = \xi_l \xi_n \hat{G}_{km}^0(\boldsymbol{\xi}), \quad (3.81)$$

the corresponding strain field is obtained by

$$\hat{\varepsilon}_{kl}(\mathbf{u}^*) = -\hat{\Gamma}_{klmn}^0(\boldsymbol{\xi}) \hat{\tau}_{mn}(\boldsymbol{\xi}). \quad (3.82)$$

In the equation above one observes that the convolution in Equation (3.46) transforms in Fourier space, into a multiplication. This is a very important fact and represents the key advantage for solving the Lippmann-Schwinger equation in Fourier space. For an isotropic reference material with the Lamé constants λ^0 , μ^0 and the stiffness

$$\mathbb{C}_{ijkl}^0 = \lambda^0 \delta_{ij} \delta_{kl} + \mu^0 (\delta_{ik} \delta_{jl} + \delta_{jk} \delta_{il}), \quad (3.83)$$

the Fourier transform of the Green's operator $\hat{\Gamma}_{ijkl}^0$ is explicitly known and takes the form

$$\hat{\Gamma}_{ijkl}^0(\boldsymbol{\xi}) = \frac{(\delta_{ki} \xi_l \xi_j + \delta_{li} \xi_k \xi_j + \delta_{kj} \xi_l \xi_i + \delta_{lj} \xi_k \xi_i)}{4\mu^0 |\boldsymbol{\xi}|^2} - \frac{\lambda^0 + \mu^0}{\mu^0 (\lambda^0 + 2\mu^0)} \frac{\xi_i \xi_j \xi_k \xi_l}{|\boldsymbol{\xi}|^4}. \quad (3.84)$$

The second order Green's operator $\hat{G}_{ij}^0(\boldsymbol{\xi})$ and its inverse $(\hat{G}^0)_{ij}^{-1}(\boldsymbol{\xi})$ are given by

$$\hat{G}_{ij}^0(\boldsymbol{\xi}) = \frac{\mu^0}{|\boldsymbol{\xi}|^2} \left(\delta_{ij} - \frac{\xi_i \xi_j}{|\boldsymbol{\xi}|^2} \frac{\lambda^0 + \mu^0}{\lambda^0 + 2\mu^0} \right), \quad (3.85)$$

$$(\hat{G}^0)_{ij}^{-1}(\boldsymbol{\xi}) = (\lambda^0 + \mu^0) \xi_i \xi_j + \mu^0 |\boldsymbol{\xi}|^2 \delta_{ij}. \quad (3.86)$$

Expressions of $\hat{\Gamma}^0$ associated with different types of anisotropic material behavior can be found in Mura [1987].

3.2.5 Voxel Discretization and Fast Fourier Transformation

The numerical homogenization problem described in the previous sections is located in a cubic volume element according to Figure 3.5.⁴ The structure is discretized in

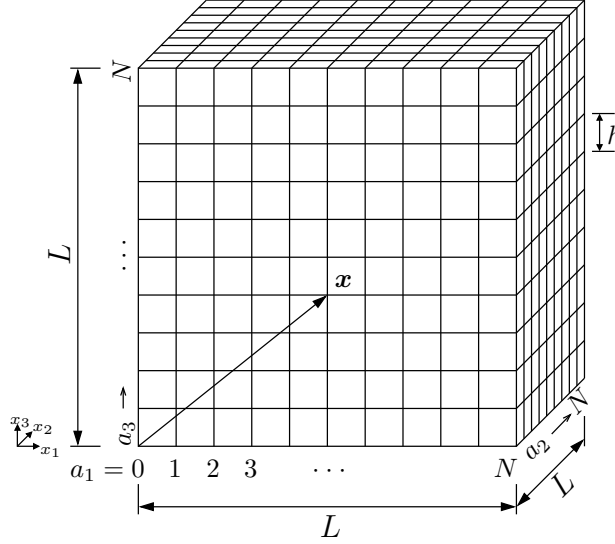


Figure 3.5: Discretization of the cubic volume element ω_h with N cells in each spatial directions a_i , the grid size h and the periodic length L .

$N \times N \times N$ cubic cells arranged in a regular grid with the base length L and hence, the grid size h is given by

$$h = \frac{L}{N}. \quad (3.87)$$

The regular distribution of the discrete points \mathbf{x} , which are located at the center of a cubic cell, permits the expression of the local field variables in Fourier space at the discrete spatial frequency points $\boldsymbol{\xi}$. The indices a_1, a_2, a_3 ($0 \leq a_1, a_2, a_3 \leq N - 1$) correspond to the discrete points \mathbf{x} in each spatial direction in real space. The corresponding numbers of the discrete spatial frequencies $\boldsymbol{\xi}$ in Fourier space are denoted by $\alpha_1, \alpha_2, \alpha_3$. For an even number of cells N the indices $\alpha_1, \alpha_2, \alpha_3$ of the discrete frequency points are defined in the range $-N/2 + 1 \leq \alpha_1, \alpha_2, \alpha_3 \leq N/2$ and for an odd number of N by $-N/2 \leq \alpha_1, \alpha_2, \alpha_3 \leq N/2$. Hence, the discrete Fourier transform of a local micro field \mathbf{u} is obtained from the following finite sum:

$$\hat{\mathbf{u}}(\boldsymbol{\xi}_{\alpha_{1,2,3}}) = \frac{1}{N^3} \sum_{a_1} \sum_{a_2} \sum_{a_3} \mathbf{u}(\mathbf{x}_{a_1}, \mathbf{x}_{a_2}, \mathbf{x}_{a_3}) \exp^{-i(\boldsymbol{\xi}_{\alpha_{1,2,3}} \cdot \mathbf{x}_{a_1} + \boldsymbol{\xi}_{\alpha_{1,2,3}} \cdot \mathbf{x}_{a_2} + \boldsymbol{\xi}_{\alpha_{1,2,3}} \cdot \mathbf{x}_{a_3})}, \quad (3.88)$$

⁴In the example illustrated in Figure 3.5 the volume element has a cubic shape and is discretized by the same amount of cells N in each direction. In general, the transformation rules can also be applied on cuboid structures with a varying number of cells N_1, N_2, N_3 in each spatial direction.

and the inverse transformation (for an odd number of cells N) is given by

$$\mathbf{u}(\mathbf{x}_{a_{1,2,3}}) = \sum_{\alpha_1} \sum_{\alpha_2} \sum_{\alpha_3} \hat{\mathbf{u}}(\boldsymbol{\xi}_{\alpha_1}, \boldsymbol{\xi}_{\alpha_2}, \boldsymbol{\xi}_{\alpha_3}) \exp^{i(\mathbf{x}_{a_{1,2,3}} \cdot \boldsymbol{\xi}_{\alpha_1} + \mathbf{x}_{a_{1,2,3}} \cdot \boldsymbol{\xi}_{\alpha_2} + \mathbf{x}_{a_{1,2,3}} \cdot \boldsymbol{\xi}_{\alpha_3})} . \quad (3.89)$$

With this method, images obtained from three dimensional image processing techniques, like computer tomography (CT), can be used directly. The discretization is obtained in an additional image processing step by segmentation (also referred to as binarization) of the materials' phases according to the gradation of the corresponding grey values, whereby the materials are assumed to be perfectly bonded. In image processing the discrete micro cells or three dimensional image points, respectively, are also referred to as voxels. In comparison to the finite element technique no additional effort has to be put into the mesh generation to discretize the complex geometrical setting of materials' microstructures. The regularity of the grid renders superfluous the storage of the geometrical mesh information, permits the use of higher image resolutions and thus, enables the computation of larger, realistic microstructures. However, periodic boundary conditions are applied for homogenization and periodicity of the microstructures is assumed.

3.2.6 Numerical Solution Scheme and Discrete Algorithm

Moulinec and Suquet [1994] proposed a numerical scheme to solve the Lippmann-Schwinger integral equation iteratively. The so called basic scheme which was originally proposed for linear elastic material behavior was subsequently extended by the authors to account for nonlinear material behavior (Moulinec and Suquet [1998]).

Remark: In the following part, a special matrix notation is omitted. Multi dimensional variables, as well as matrices are indicated with bolt letters.

For the linear elastic case the Lippmann-Schwinger equation can be rewritten as a system of equations which is given in operator notation as

$$(\mathbf{I} + \mathbf{B})\boldsymbol{\varepsilon} := \boldsymbol{\varepsilon} + \boldsymbol{\Gamma}^0 * ((\mathbb{C} - \mathbb{C}^0) : \boldsymbol{\varepsilon}) = \mathbf{E} , \quad (3.90)$$

where \mathbf{I} is the identity matrix and \mathbf{B} a non-symmetric system matrix associated with the linear reference material (see Kabel and Andrä [2012], Zeman et al. [2010])

$$\mathbf{B}\boldsymbol{\varepsilon} := \boldsymbol{\Gamma}^0 * ((\mathbb{C} - \mathbb{C}^0) : \boldsymbol{\varepsilon}) . \quad (3.91)$$

The solution vector $\boldsymbol{\varepsilon}$ of the strain field is given by

$$\boldsymbol{\varepsilon} = (\mathbf{I} + \mathbf{B})^{-1} \mathbf{E} . \quad (3.92)$$

The matrix inverse $(\mathbf{I} + \mathbf{B})^{-1}$ is obtained by a Neumann series expansion and the

$l+1$ -th iterate of the strain field reads

$$\boldsymbol{\varepsilon}^{l+1} = \sum_{m=0}^{l+1} (-\mathbf{B})^m \mathbf{E} . \quad (3.93)$$

The expansion converges for the operator norm $\|\mathbf{B}\| < 1$. The following equivalent expression gives the iterative solution scheme

$$\boldsymbol{\varepsilon}^{l+1} = \mathbf{E} - \mathbf{B}\boldsymbol{\varepsilon}^l , \quad (3.94)$$

with the first iterate $\boldsymbol{\varepsilon}^0 = \mathbf{E}$, and hence, the Lippmann-Schwinger equation to be solved has the following iterative form

$$\boldsymbol{\varepsilon}^{l+1}(\mathbf{x}) = \mathbf{E} - (\boldsymbol{\Gamma}^0 * ((\mathbb{C} - \mathbb{C}^0) : \boldsymbol{\varepsilon}^l))(\mathbf{x}) , \quad \mathbf{x} \text{ in } \omega_h . \quad (3.95)$$

The main benefit of the scheme is based on the fact that the constitutive part in Equation (3.95) $(\mathbb{C} - \mathbb{C}^0) : \boldsymbol{\varepsilon}^l$ is evaluated in the real space at a local point \mathbf{x} in ω_h and the convolution integral $\boldsymbol{\Gamma}^0 : \boldsymbol{\tau}$ is solved in Fourier space as a direct product for each spatial Fourier frequency $\boldsymbol{\xi}$. The transformation of the calculated fields is performed by fast Fourier transformation (FFT). Basically, the transformation strongly affects the efficiency of the numerical scheme, due to the fact that the fields have to be transformed several times in each equilibrium iteration. In this work the transformation of the local field variables is performed with the C subroutine library FFTW [2014].

The problem stated in Equation (3.95) is solved iteratively. Each iteration l consists of four steps which are repeated until global convergence is reached. In the first iteration, $l = 0$, the strain field is initialized at each point in the real space \mathbf{x} by a uniform strain with the size of the constant macroscopic deformation \mathbf{E}

$$\boldsymbol{\varepsilon}^0(\mathbf{x}) = \mathbf{E} . \quad (3.96)$$

The stress polarization is calculated at each point in the real space

$$\boldsymbol{\tau}^l(\mathbf{x}) = (\mathbb{C} - \mathbb{C}^0) : \boldsymbol{\varepsilon}^l(\mathbf{x}) , \quad (3.97)$$

and is then transformed in Fourier space by applying the discrete transformation rule according to Equation (3.88)

$$\hat{\boldsymbol{\tau}}^l(\boldsymbol{\xi}) = \text{FFT}(\boldsymbol{\tau}^l(\mathbf{x})) , \quad (3.98)$$

$$\hat{\boldsymbol{\tau}}^l(\boldsymbol{\xi}_{\alpha_{1,2,3}}) = \frac{1}{N^3} \sum_{a_1} \sum_{a_2} \sum_{a_3} \boldsymbol{\tau}^l(\mathbf{x}_{a_1}, \mathbf{x}_{a_2}, \mathbf{x}_{a_3}) \exp^{-i(\boldsymbol{\xi}_{\alpha_{1,2,3}} \cdot \mathbf{x}_{a_1} + \boldsymbol{\xi}_{\alpha_{1,2,3}} \cdot \mathbf{x}_{a_2} + \boldsymbol{\xi}_{\alpha_{1,2,3}} \cdot \mathbf{x}_{a_3})} .$$

The Green's operator is applied on the calculated stress polarization and the updated

strain field is obtained in Fourier space for each discrete spatial frequency $\boldsymbol{\xi}_{\alpha_{1,2,3}}$

$$\hat{\boldsymbol{\varepsilon}}^{l+1}(\boldsymbol{\xi}_{\alpha_{1,2,3}}) = -\hat{\boldsymbol{\Gamma}}^0(\boldsymbol{\xi}_{\alpha_{1,2,3}}) : \hat{\boldsymbol{\tau}}^l(\boldsymbol{\xi}_{\alpha_{1,2,3}}) \quad \forall \alpha_{1,2,3} \neq 0, \quad (3.99)$$

$$\hat{\boldsymbol{\varepsilon}}^{l+1}(0) = \mathbf{E}. \quad (3.100)$$

Finally, the solution is retransformed in the real space according to the inverse transformation rule specified in Equation (3.89)

$$\boldsymbol{\varepsilon}^{l+1} = \text{FFT}^{-1}(\hat{\boldsymbol{\varepsilon}}^{l+1}), \quad (3.101)$$

$$\boldsymbol{\varepsilon}^{l+1}(\mathbf{x}_{\alpha_{1,2,3}}) = \sum_{\alpha_1} \sum_{\alpha_2} \sum_{\alpha_3} \hat{\boldsymbol{\varepsilon}}^{l+1}(\boldsymbol{\xi}_{\alpha_1}, \boldsymbol{\xi}_{\alpha_2}, \boldsymbol{\xi}_{\alpha_3}) \exp^{i(\mathbf{x}_{\alpha_{1,2,3}} \cdot \boldsymbol{\xi}_{\alpha_1} + \mathbf{x}_{\alpha_{1,2,3}} \cdot \boldsymbol{\xi}_{\alpha_2} + \mathbf{x}_{\alpha_{1,2,3}} \cdot \boldsymbol{\xi}_{\alpha_3})}.$$

The transformation of the strain field, which is known at discrete Fourier frequencies can be interpreted as a trigonometric collocation by approximating the point values with exponential basis functions (see Schneider [2014]). Hence, the continuity of the searched strain field is given.

The iteration steps of the basic scheme are repeated until convergence in terms of an equilibrated global system is reached. The steps are summarized in the following box

1. Solve the constitutive equation in the real space, compute stress polarization
2. Fourier transformation of the stress polarization field
3. Convolution with the Green's operator in the Fourier space
4. Inverse Fourier transformation of the updated strain field

$$\begin{aligned} \boldsymbol{\tau}^l &= (\mathbf{c} - \mathbf{C}^0) : \boldsymbol{\varepsilon}^l \\ \hat{\boldsymbol{\tau}}^l &= \text{FFT}(\boldsymbol{\tau}^l) \\ \hat{\boldsymbol{\varepsilon}}^{l+1} &= -\hat{\boldsymbol{\Gamma}}^0 : \hat{\boldsymbol{\tau}}^l, \quad \hat{\boldsymbol{\varepsilon}}^{l+1}(0) = \mathbf{E} \\ \boldsymbol{\varepsilon}^{l+1} &= \text{FFT}^{-1}(\hat{\boldsymbol{\varepsilon}}^{l+1}) \end{aligned} \quad (3.102)$$

The basic scheme is in principle applicable for any arbitrary nonlinear constitutive law

$$\boldsymbol{\sigma}(\mathbf{x}) = \mathcal{F}(\boldsymbol{\varepsilon}(\mathbf{x}), \mathcal{I}(\mathbf{x})). \quad (3.103)$$

The nonlinear form of the Lippmann-Schwinger equation according to Equation (3.52) has to be solved iteratively:

$$\boldsymbol{\varepsilon}^{l+1} = \mathbf{E} - \boldsymbol{\Gamma}^0 * (\boldsymbol{\sigma}(\boldsymbol{\varepsilon}^l, \mathcal{I}) - \mathbf{C}^0 : \boldsymbol{\varepsilon}^l). \quad (3.104)$$

In this work, the coupled linear elastic and the coupled elasto-plastic damage model described in Section 2.3 are implemented. In a general form the nonlinear scheme

can be summarized as follows.

$$\begin{aligned}
 \boldsymbol{\tau}^l &= \boldsymbol{\sigma}(\boldsymbol{\varepsilon}^l, \boldsymbol{\mathcal{I}}) - \mathbf{C}^0 : \boldsymbol{\varepsilon}^l \\
 \hat{\boldsymbol{\tau}}^l &= \text{FFT}(\boldsymbol{\tau}^l) \\
 \hat{\boldsymbol{\varepsilon}}^{l+1} &= -\hat{\boldsymbol{\Gamma}}^0 : \hat{\boldsymbol{\tau}}^l, \quad \hat{\boldsymbol{\varepsilon}}^{l+1}(0) = \mathbf{E} \\
 \boldsymbol{\varepsilon}^{l+1} &= \text{FFT}^{-1}(\hat{\boldsymbol{\varepsilon}}^{l+1})
 \end{aligned} \tag{3.105}$$

In the nonlinear scheme the linear elastic constitutive law $\boldsymbol{\sigma} = \mathbf{c} : \boldsymbol{\varepsilon}$ in (3.102) is replaced by a nonlinear constitutive equation $\boldsymbol{\sigma} = \mathcal{F}(\boldsymbol{\varepsilon}, \boldsymbol{\mathcal{I}})$ which is computed in the real space. The current stress state and the updated internal variables can be computed in a separated material routine, e.g in a plastic return mapping algorithm. The constitutive law has to be integrated at each local material point \boldsymbol{x} during the global load step, similar to the procedure well-known from the finite element method. The task of the material routine is to find the stress state $\boldsymbol{\sigma}^l$ corresponding to the current strain increment $\Delta\boldsymbol{\varepsilon}^l$ according the following scheme:

$$\begin{array}{c}
 \downarrow \boldsymbol{\varepsilon}^l = \boldsymbol{\varepsilon}^{l-1} + \Delta\boldsymbol{\varepsilon}^l \\
 \boxed{\boldsymbol{\sigma} = \mathcal{F}(\boldsymbol{\varepsilon}^l, \boldsymbol{\mathcal{I}})} \\
 \downarrow \boldsymbol{\sigma}^l, \mathbf{c}^l
 \end{array}
 \quad
 \begin{array}{l}
 \leftarrow \boldsymbol{\mathcal{I}}^{l-1} \\
 \rightarrow \boldsymbol{\mathcal{I}}^l
 \end{array}$$

Furthermore, the internal variables $\boldsymbol{\mathcal{I}}$ are updated and the tangential material stiffness \mathbf{c}^l is computed.

The polarization stress $\boldsymbol{\tau}^l$ is obtained from the current stress state $\boldsymbol{\sigma}^l$ and the stress in the homogeneous reference material $\mathbf{C}^0 : \boldsymbol{\varepsilon}^l$. Thereby the reference stiffness \mathbf{C}^0 remains constant during the iterations. Performing a nonlinear computation in several time steps, the stiffness of the reference material \mathbf{C}^0 and the associated Green's operator $\boldsymbol{\Gamma}^0$ can be updated in each time step for obtaining a better convergence behavior.

Several authors proposed extended algorithms dealing with nonlinear material behavior in a computational framework. Moulinec and Suquet [1998] introduced an algorithm for strain-hardening plasticity, Bilger et al. [2007] suggested a method to describe rigid plastic behavior in porous media and Idiart et al. [2006] as well as Lebensohn et al. [2012] extended existing methods for visco-plastic material behavior. An algorithm for implementing non-local damage was proposed by Moos [2013], and furthermore, in the context of damage mechanics Li et al. [2012] developed a non-local fracture model.

Regarding the stopping criterion of the numerical schemes, several proposals exist, how to check the global solution of a unit cell problem. According to Moulinec and Suquet [1998] convergence is reached when the global stress field is in equilibrium

and the stopping criterion is given by

$$\frac{\|\operatorname{div} \boldsymbol{\sigma}^{l+1}\|}{\|\boldsymbol{\sigma}^{l+1}\|} \leq \operatorname{tol}_1, \quad (3.106)$$

which can easily be computed in Fourier space by a simple direct product:

$$\frac{\|\boldsymbol{\xi} \cdot \hat{\boldsymbol{\sigma}}^{l+1}(\boldsymbol{\xi})\|}{\|\hat{\boldsymbol{\sigma}}^{l+1}(\mathbf{0})\|} \leq \operatorname{tol}_1. \quad (3.107)$$

Here, $\hat{\boldsymbol{\sigma}}(\mathbf{0})$ represents the average or macroscopic stress $\boldsymbol{\Sigma} = \langle \boldsymbol{\sigma} \rangle$ and $\|\cdot\|$ denotes the L^2 -norm of the appropriate field variable. Applying this criterion both fields, the strain and the stress field have to be stored and for computing $\boldsymbol{\xi} \cdot \hat{\boldsymbol{\sigma}}$ an additional Fourier transformation has to be performed.

In this work, a second convergence criterion is applied, which controls the difference of the strain field between two iterations in real space (see e.g. Brisard and Dormieux [2010]):

$$\frac{\|\boldsymbol{\varepsilon}^{l+1} - \boldsymbol{\varepsilon}^l\|^2}{\|\mathbf{E}\|^2} \leq \operatorname{tol}_2. \quad (3.108)$$

Besides the current strain field $\boldsymbol{\varepsilon}^{l+1}$ the strain field of the previous iteration $\boldsymbol{\varepsilon}^l$ has to be stored, which requires additional memory. Typical values for the convergence tolerances are $\operatorname{tol}_1 = 10^{-4}$ and $\operatorname{tol}_2 = 10^{-10}$.

The elastic parameters of the reference material \mathbf{C}^0 have important influence on the convergence rate of the scheme, especially when dealing with nonlinear materials. According to Moulinec and Suquet [1998] the parameters are chosen as an average of the maximum and minimum values of the local material phases:

$$k^0 = \frac{1}{2} \left(\min_{\mathbf{x}} k(\mathbf{x}) + \max_{\mathbf{x}} k(\mathbf{x}) \right), \quad \mu^0 = \frac{1}{2} \left(\min_{\mathbf{x}} \mu(\mathbf{x}) + \max_{\mathbf{x}} \mu(\mathbf{x}) \right), \quad (3.109)$$

where $k(\mathbf{x})$ and $\mu(\mathbf{x})$ denote shear and bulk modulus of an isotropic material, respectively. Instead of choosing the arithmetic average, the parameters of the reference material can be chosen by weighting the local maximum and minimum values of $k(\mathbf{x})$ and $\mu(\mathbf{x})$ by their volume content in the unit cell. In addition, Eisenlohr et al. [2013] proposed to use \mathbf{C}^0 as the volume average of the stiffness matrices over the entire domain

$$\mathbf{C}^0 = \langle \mathbf{c}(\mathbf{x}) \rangle. \quad (3.110)$$

This choice leads to a fully anisotropic reference material which does not admit the explicit expression of the Green's operator $\boldsymbol{\Gamma}^0$. In this work, the reference material is chosen as the average of the minimal and maximal eigenvalue of the local tangential stiffness matrices $\mathbf{c}(\mathbf{x})$. According to Kabel et al. [2014] the identity matrix \mathbb{I} is multiplied by a scalar value which is computed as the average of the positive

maximal and minimal eigenvalue

$$\mathbf{C}^0 = \frac{1}{2} (\lambda_{\min}(\mathbf{c}(\mathbf{x})) + \lambda_{\max}(\mathbf{c}(\mathbf{x}))) \mathbb{I}. \quad (3.111)$$

Besides the choice of the reference material the convergence rate generally depends strongly on the stiffness contrast of the material phases. In particular, progressive damage behavior leads to increasing stiffness contrasts and consequently the convergence behavior becomes worse. Certain numerical schemes were developed during the last decade to improve the convergence behavior of the method for materials with high stiffness contrasts.

In the context of electrical conductivity problems Eyre and Milton [1999] introduced an accelerated scheme using a modified Green's operator. Michel et al. [2000, 2001] established an augmented Lagrangian scheme to improve the convergence of the basic scheme for elasticity problems with high contrasts. In this regard, an equivalent saddle-point formulation is solved using an augmented Lagrangian method. Zeman et al. [2010] proposed a modified scheme using Krylov subspace solvers instead of fixed-point iterations which were initially proposed by Moulinec and Suquet [1998]. The method is applied on a linear electric conduction problem and the linear system is solved by the conjugate gradient (CG) or the biconjugate gradient (BiCG) method. A numerical scheme, which is also applicable to arbitrary phase contrasts was derived by Brisard and Dormieux [2010]. The Green's operator is obtained within a variational framework from the upper Hashin-Shtrikman bound (see Hashin and Shtrikman [1963]). Monchiet and Bonnet [2012] introduced a polarization-based iterative scheme in which a polarization is prescribed over the unit cell instead of a uniform macroscopic strain. Furthermore, Brisard and Dormieux [2012] introduced a modified, so-called filtered Green's operator. By removing oscillations which arise in the neighborhood of inclusions the convergence should be improved for higher phase contrasts. A review of different schemes and an analysis of the convergence behavior for the computation of precise bounds of effective properties in comparison with analytical estimates can be found in Kabel and Andr a [2012] or in Moulinec and Silva [2014].

Regarding large deformations in the context of a FFT-based framework the Newton-Raphson (NR) method can be used. The system has to be linearized at the current load state and the linearized equations are solved iteratively in each NR iteration step. While Lahellec et al. [2003] suggested to use fixed point iteration to solve the linearized equation, Kabel et al. [2014] proposed a memory efficient Newton-Krylov method. The CG method as particular Krylov subspace method is used to solve the linearized differential equation in each Newton iteration. Furthermore, Eisenlohr et al. [2013] applied the fixed point iteration to solve the nonlinear equation directly, without preceding Newton linearization.

As far as no convergence problems occurred, the basic scheme is used to compute the examples in this work. Fixed point iteration is used to solve the (non-linearized) nonlinear equations directly. Regarding its simplicity, accuracy and numerical efficiency the scheme is, in the opinion of the author, still difficult to surpass for most

practical problems.

The complete numerical scheme is illustrated in Algorithm 1. The basic scheme is implemented in the three dimensional code FeelMath [2014].

Loop over time steps n

$\mathbf{E}^n = \mathbf{E}^{n-1} + \Delta \mathbf{E}^n$

$\boldsymbol{\varepsilon}_{i=0}(\mathbf{x}) = \mathbf{E}^n$

Compute reference stiffness $\mathbb{C}^{0,n}$ from local tangential matrices $\mathbb{C}^n(\mathbf{x})$

Loop over fixed-point iterations i

Basic Scheme ① - ④:

Loop over discrete points \mathbf{x}

Read internal variables from last converged time step $\mathcal{I}_{\bullet}^{n-1}(\mathbf{x})$

Loop over iterations of constitutive algorithm

┌ ① $\boldsymbol{\sigma}_i(\mathbf{x}), \mathcal{I}_i(\mathbf{x})$ from $\mathcal{F}(\boldsymbol{\varepsilon}_i(\mathbf{x}), \mathcal{I}_{\bullet}^{n-1}(\mathbf{x}))$

$\mathbb{C}_i(\mathbf{x}) = \frac{\partial \boldsymbol{\sigma}_i(\mathbf{x})}{\partial \boldsymbol{\varepsilon}_i(\mathbf{x})}$

Store internal variables $\mathcal{I}_i(\mathbf{x})$

└ $\boldsymbol{\tau}_i(\mathbf{x}) = \boldsymbol{\sigma}_i(\mathbf{x}) - \mathbb{C}^{0,n} : \boldsymbol{\varepsilon}_i(\mathbf{x})$

② $\hat{\boldsymbol{\tau}}_i(\boldsymbol{\xi}) = \text{FFT}(\boldsymbol{\tau}_i(\mathbf{x}))$

Loop over discrete frequencies $\boldsymbol{\xi}$

┌ ③ $\hat{\boldsymbol{\varepsilon}}_{i+1}(\boldsymbol{\xi}) = -\hat{\mathbf{I}}^{0,n}(\boldsymbol{\xi}) : \hat{\boldsymbol{\tau}}_i(\boldsymbol{\xi}), \quad \hat{\boldsymbol{\varepsilon}}_{i+1}(0) = \mathbf{E}^n$

④ $\boldsymbol{\varepsilon}_{i+1} = \text{FFT}^{-1}(\hat{\boldsymbol{\varepsilon}}_{i+1}(\boldsymbol{\xi}))$

If stopping criterion $\frac{\|\boldsymbol{\varepsilon}_{i+1} - \boldsymbol{\varepsilon}_i\|^2}{\|\mathbf{E}^n\|^2} > \text{tol}$ then $i=i+1$ else break

Update internal variables $\mathcal{I}^n(\mathbf{x}) = \mathcal{I}_{i+1}(\mathbf{x})$

Export solution

Algorithm 1: Incremental solution of nonlinear periodic boundary value problem using fixed point iteration.

Chapter 4

Multiscale Method

This section concerns the multiscale approach proposed in this work. The iterative coupling procedure, the boundary value problems on both scales and the technique to obtain the macroscopic stiffness tangent in each macroscopic Newton iteration are introduced. In the following, capital letters are used to describe macroscopic quantities, whereby the lowercase is used to define quantities on the microscale.

4.1 Iterative Scale Coupling

The microscopic model is used in a multiscale framework in order to investigate the macroscopic damage behavior. The detailed resolution of the microstructural constituents leads to a fine discretization of the computational model and thus to large algebraic systems with many degrees of freedom. Hence, an efficient solution of the microscopic boundary value problem is necessary.

In the work at hand, the Lippmann Schwinger equations and the FFT based formulation introduced in Section 3.2 are used to solve an equivalent periodic microscopic BVP for the homogenization. The macroscopic problem is discretized with finite elements and solved iteratively with the Newton Raphson method (see Section 3.1.4). The approach combines the advantages of both numerical methods, also see Spahn et al. [2014a]. Arbitrary macroscopic geometries can be discretized by the finite element method, while the microscopic problem benefits from its efficiency in terms of computational time and memory consumption. The assembly of a global matrix is circumvented and no further meshing is necessary. The discretized microstructure can directly be obtained from a CT scan. Both scales are coupled by a procedure similar to the FE² approach (see Smit et al. [1998] and Feyel and Chaboche [2000]). Thus the constitutive equation on the macroscale is replaced by a separate BVP on the microscale (see Figure 4.1).

Each macroscopic integration point is equipped with a RVE which represents the particular microstructure at this point. The variables which are transferred between both scales are defined by volume averages over the micro domain ω

$$\langle \cdot \rangle = \frac{1}{|\omega|} \int_{\omega} (\cdot) \, dv . \quad (4.1)$$

The macroscopic strain tensor $\mathbf{E} = \langle \boldsymbol{\varepsilon} \rangle$ is imposed on the microscopic domain and a local periodic boundary value problem is solved. The macroscopic stress response

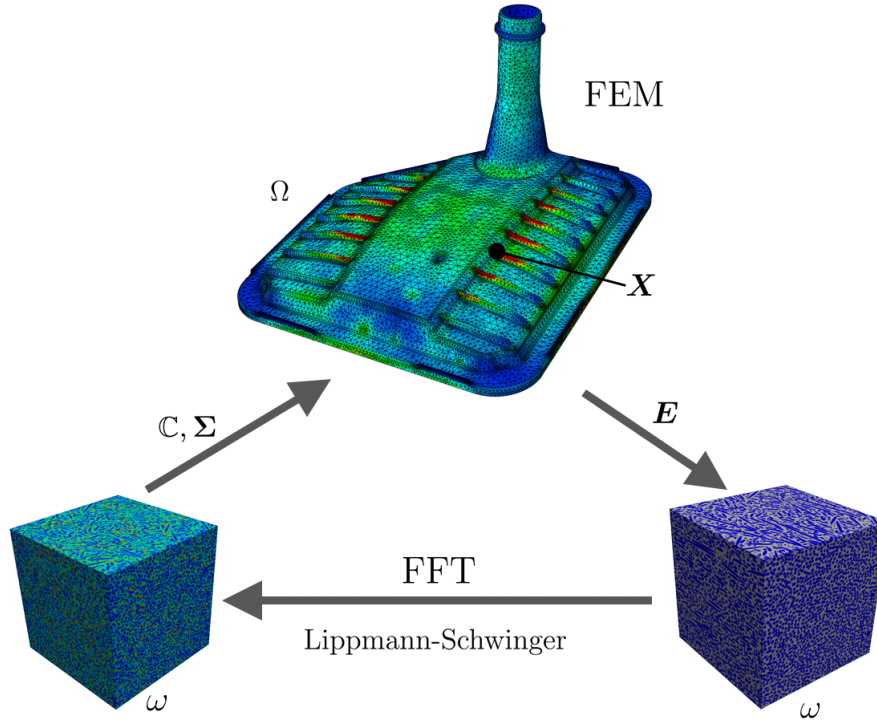


Figure 4.1: Scale coupling and multiscale approach schematically. Macroscopic scale represented by a glass fiber reinforced filter housing.

Σ is obtained in terms of the averaged equilibrated microscopic stress field $\langle \boldsymbol{\sigma} \rangle$

$$\Sigma = \langle \boldsymbol{\sigma} \rangle = \frac{1}{|\omega|} \int_{\omega} \boldsymbol{\sigma}(\mathbf{x}) \, dv . \quad (4.2)$$

Besides the averaged stress, the macroscopic tangential stiffness matrix \mathbf{C} has to be computed at the current macroscopic load iteration. Due to the nonlinearity of the macroscopic and microscopic problem both scales have to be coupled in an iterative way. Hence, the multiscale scheme depicted in Figure 4.1 is repeated until convergence of the global (macroscopic) problem is reached. The microscopic problem is solved in each Newton iteration for the macroscopic level in each macroscopic point \mathbf{X} . In the following the boundary value problems on both scales are introduced.

4.2 Boundary Value Problems at the Spatial Scales

As already mentioned in Section 2.4.5, the computation of the macroscopic stress during the homogenization procedure has to fulfill the energy criterion proposed by Hill [1963, 1972]. According to the energy equivalence principle on both scales the linear elastic homogenized stiffness is defined by the following equation:

$$\frac{1}{2} \langle \boldsymbol{\varepsilon} : \mathbf{c} : \boldsymbol{\varepsilon} \rangle_{\omega} = \frac{1}{2} \langle \boldsymbol{\varepsilon} \rangle_{\omega} : \mathbf{C} : \langle \boldsymbol{\varepsilon} \rangle_{\omega} , \quad \text{where } \mathbf{c} = \mathbf{c}(\mathbf{x}). \quad (4.3)$$

The criterion is valid, among others, for the following type of boundary conditions applied on the RVE:

- Kinematic boundary conditions with prescribed linear displacements (Dirichlet conditions)

$$\mathbf{u}(\mathbf{x}) = \mathbf{E} \cdot \mathbf{x}, \quad \mathbf{x} \text{ on } \partial\omega. \quad (4.4)$$

- Periodic boundary conditions for $u^*(\mathbf{x})$ and

$$\mathbf{u}(\mathbf{x}) = \mathbf{E} \cdot \mathbf{x} + \mathbf{u}^*(\mathbf{x}), \quad \mathbf{x} \text{ in } \omega. \quad (4.5)$$

- Static boundary conditions with prescribed constant tractions (Neumann conditions)

$$\mathbf{t}(\mathbf{x}) = \boldsymbol{\Sigma} \cdot \mathbf{n}, \quad \mathbf{x} \text{ on } \partial\omega. \quad (4.6)$$

While Dirichlet and Neumann boundary conditions provide upper and lower bounds for the effective stiffness \mathbf{C} , the estimation with periodic boundary conditions is situated between both (see Hazanov and Huet [1994], Kanit et al. [2003] and Ostoja-Starzewski [2006] for more details).

In this work strain-controlled periodic BCs according to Section 3.2.1 are applied on the microscopic BVP. Considering a general constitutive relation \mathcal{F} the periodic micro BVP reads as follows:

$$\operatorname{div}(\boldsymbol{\sigma}(\boldsymbol{\varepsilon}(\mathbf{x}), \mathcal{I}(\mathbf{x}))) = \mathbf{0} \quad \mathbf{x} \text{ in } \omega, \quad (4.7a)$$

$$\boldsymbol{\sigma}(\mathbf{x}) = \mathcal{F}(\boldsymbol{\varepsilon}(\mathbf{x}), \mathcal{I}(\mathbf{x})) \quad \mathbf{x} \text{ in } \omega, \quad (4.7b)$$

$$\boldsymbol{\varepsilon}(\mathbf{x}) = \mathbf{E} + \frac{1}{2}(\nabla \mathbf{u}^*(\mathbf{x}) + (\nabla \mathbf{u}^*(\mathbf{x}))^T) \quad \mathbf{x} \text{ in } \omega, \quad (4.7c)$$

$$\mathbf{u}^*(\mathbf{x}) \text{ periodic} \quad \mathbf{x} \text{ on } \partial\omega, \quad (4.7d)$$

$$\boldsymbol{\sigma}(\mathbf{x}) \cdot \mathbf{n}(\mathbf{x}) \text{ anti-periodic} \quad \mathbf{x} \text{ on } \partial\omega. \quad (4.7e)$$

The strain tensor \mathbf{E} in (4.7c) is obtained from the macroscale at a certain point \mathbf{X} . On the macroscale mixed BCs could be used and hence, the static macroscopic BVP with the absence of body forces reads as follows:

$$\operatorname{div} \boldsymbol{\Sigma}(\mathbf{X}) = \mathbf{0} \quad \mathbf{X} \text{ in } \Omega, \quad (4.8a)$$

$$\mathbf{E}(\mathbf{X}) = \frac{1}{2}(\nabla U(\mathbf{X}) + (\nabla U(\mathbf{X}))^T) \quad \mathbf{X} \text{ in } \Omega, \quad (4.8b)$$

$$U(\mathbf{X}) = U_0(\mathbf{X}) \quad \mathbf{X} \text{ on } \partial\Omega, \quad (4.8c)$$

$$\boldsymbol{\Sigma}(\mathbf{X}) \cdot \mathbf{N}(\mathbf{X}) = \mathbf{T}_0(\mathbf{X}) \quad \mathbf{X} \text{ on } \partial\Omega, \quad (4.8d)$$

where $U_0(\mathbf{X})$ and $\mathbf{T}_0(\mathbf{X})$ denote the prescribed macroscopic displacement vector

and traction vector on the boundary of the macroscopic domain Ω .

4.3 Consistent Macroscopic Tangent Computation and Numerical Algorithm

The macroscopic BVP is solved using a standard Newton-Raphson scheme, see Section 3.1.4. In each macroscopic Newton iteration, at each macroscopic point \mathbf{X} , the averaged microscopic stress $\langle \boldsymbol{\sigma} \rangle$ has to be computed for setting up the macroscopic residual force vector \mathbf{G} . According to (3.21) the internal force vector for a macro finite element e is given by

$$\mathbf{R}_e = \int_{\Omega_e} \mathbf{B}^T \boldsymbol{\Sigma} \, dV . \quad (4.9)$$

Additionally, for an efficient macro computation, the linearization of the internal forces $D\mathbf{G}$ is required. The linearized macroscopic tangential stiffness \mathbf{C} has to be computed at each macroscopic integration point to obtain the element stiffness matrix \mathbf{K}^e according to (3.26)

$$\mathbf{K}^e = \int_{\Omega^e} \mathbf{B}^T \mathbf{C} \mathbf{B} \, dV . \quad (4.10)$$

The macroscopic tangential stiffness is defined by the variation of the macroscopic stress with the variation of the macroscopic strain, by the following derivation:

$$\mathbf{C} = \frac{\partial \boldsymbol{\Sigma}}{\partial \mathbf{E}} . \quad (4.11)$$

Dealing with a sophisticated non linear stress-strain relation, as in the present case of a micro-macro multiscale approach, it is not possible to obtain the analytical tangent directly. In this work, the macroscopic tangent is computed by a numerical linearization around the current macroscopic load iteration. This is done by applying six small deformation states $\delta \mathbf{E}$ ⁵ on the equilibrated solution field $\boldsymbol{\varepsilon}(\mathbf{x})$ which was computed during the current macroscopic load iteration (see Figure 4.2). These perturbation strains are applied on the RVE using periodic boundary conditions. The resulting stress field is comprised of the equilibrated stress field of the macroscopic load iteration $\boldsymbol{\sigma}(\mathbf{x})$ and the incremental perturbation field $\delta \boldsymbol{\sigma}(\mathbf{x})$ caused by $\delta \mathbf{E}$

$$\boldsymbol{\sigma}_{\delta E}(\mathbf{x}) = \boldsymbol{\sigma}(\mathbf{x}) + \delta \boldsymbol{\sigma}(\mathbf{x}) = \mathcal{F}(\boldsymbol{\varepsilon}(\mathbf{x}) + \delta \mathbf{E}, \mathcal{I}(\mathbf{x})) . \quad (4.12)$$

After averaging the entire perturbed field the macro stress is obtained

$$\boldsymbol{\Sigma}_{\delta E} = \frac{1}{|\omega|} \int_{\omega} \boldsymbol{\sigma}_{\delta E}(\mathbf{x}) \, dv . \quad (4.13)$$

⁵In the context of numerical perturbation the symbol δ should not be confused with the infinitesimal variation of the total energy functional in the weak formulation of Section 3.1.1.

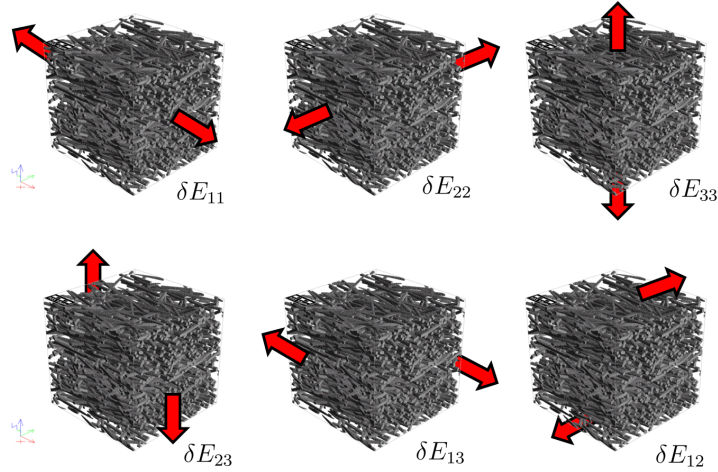


Figure 4.2: Perturbation procedure, six infinitesimal load cases are applied on the current stress state to obtain the columns of the macroscopic tangent \mathbb{C} .

The difference between the perturbed stress $\Sigma_{\delta E}$ and the unperturbed macroscopic stress Σ gives the perturbation stress increment, which is caused by $\delta \mathbf{E}$

$$\delta \Sigma = \Sigma_{\delta E} - \Sigma . \quad (4.14)$$

The numerical tangent $\mathbb{C}_{\delta E}$ can be calculated by setting the perturbation stress increment into relation with the perturbation strain

$$\delta \Sigma = \mathbb{C}_{\delta E} : \delta \mathbf{E} . \quad (4.15)$$

Numerically, each column of the homogenized stiffness $\mathbb{C}_{\delta E}$ is obtained by solving six microscopic boundary value problems according to (4.7). In the following the six perturbation load cases are shown schematically in Voigt notation with the applied strain increments $\delta \mathbf{E}$:

$$\begin{aligned} \textcircled{1} \quad \begin{bmatrix} \delta \Sigma_1 \\ \delta \Sigma_2 \\ \delta \Sigma_3 \\ \delta \Sigma_4 \\ \delta \Sigma_5 \\ \delta \Sigma_6 \end{bmatrix} &= \begin{bmatrix} \mathbf{C}_{11} & \mathbf{C}_{12} & \mathbf{C}_{13} & \mathbf{C}_{14} & \mathbf{C}_{15} & \mathbf{C}_{16} \\ \mathbf{C}_{21} & \mathbf{C}_{22} & \mathbf{C}_{23} & \mathbf{C}_{24} & \mathbf{C}_{25} & \mathbf{C}_{26} \\ \mathbf{C}_{31} & \mathbf{C}_{32} & \mathbf{C}_{33} & \mathbf{C}_{34} & \mathbf{C}_{35} & \mathbf{C}_{36} \\ \mathbf{C}_{41} & \mathbf{C}_{42} & \mathbf{C}_{43} & \mathbf{C}_{44} & \mathbf{C}_{45} & \mathbf{C}_{46} \\ \mathbf{C}_{51} & \mathbf{C}_{52} & \mathbf{C}_{53} & \mathbf{C}_{54} & \mathbf{C}_{55} & \mathbf{C}_{56} \\ \mathbf{C}_{61} & \mathbf{C}_{62} & \mathbf{C}_{63} & \mathbf{C}_{64} & \mathbf{C}_{65} & \mathbf{C}_{66} \end{bmatrix} \begin{bmatrix} \delta E_1 \\ 0 \\ 0 \\ 0 \\ 0 \\ 0 \end{bmatrix} \\ &\vdots \\ \textcircled{6} \quad \begin{bmatrix} \delta \Sigma_1 \\ \delta \Sigma_2 \\ \delta \Sigma_3 \\ \delta \Sigma_4 \\ \delta \Sigma_5 \\ \delta \Sigma_6 \end{bmatrix} &= \begin{bmatrix} \mathbf{C}_{11} & \mathbf{C}_{12} & \mathbf{C}_{13} & \mathbf{C}_{14} & \mathbf{C}_{15} & \mathbf{C}_{16} \\ \mathbf{C}_{21} & \mathbf{C}_{22} & \mathbf{C}_{23} & \mathbf{C}_{24} & \mathbf{C}_{25} & \mathbf{C}_{26} \\ \mathbf{C}_{31} & \mathbf{C}_{32} & \mathbf{C}_{33} & \mathbf{C}_{34} & \mathbf{C}_{35} & \mathbf{C}_{36} \\ \mathbf{C}_{41} & \mathbf{C}_{42} & \mathbf{C}_{43} & \mathbf{C}_{44} & \mathbf{C}_{45} & \mathbf{C}_{46} \\ \mathbf{C}_{51} & \mathbf{C}_{52} & \mathbf{C}_{53} & \mathbf{C}_{54} & \mathbf{C}_{55} & \mathbf{C}_{56} \\ \mathbf{C}_{61} & \mathbf{C}_{62} & \mathbf{C}_{63} & \mathbf{C}_{64} & \mathbf{C}_{65} & \mathbf{C}_{66} \end{bmatrix} \begin{bmatrix} 0 \\ 0 \\ 0 \\ 0 \\ 0 \\ \delta E_6 \end{bmatrix} \end{aligned}$$

The computation of the perturbation load cases requires additional computational time. But in comparison to the condensation procedure introduced in Section 2.4.5 less memory is required for the computation of the macroscopic tangent. There is no need for a memory expensive matrix inverting, and thus, larger micro systems can be treated.

For an infinitesimal small $\delta\mathbf{E}$ the numerical tangent equals the analytical one which is defined in (4.11)

$$\lim_{\delta\mathbf{E}\rightarrow 0} \mathbf{C}_{\delta\mathbf{E}} = \mathbf{C} . \quad (4.16)$$

But the perturbation must not be too small for practical purposes, to avoid numerical problems caused by round-off errors. Difficulties occur when the sensitivity of the numerical method is not sufficient enough to identify the small stress increment $\delta\mathbf{\Sigma}$ correctly. The accuracy is limited in the convergence behavior of the micromechanical method and at least in the machine precision. In this context Dennis and Schnabel [1987] and Miehe [1996] investigated the size of the perturbation in dependence of the existing machine precision. Assuming a machine precision of 10^{-16} , in literature values between 10^{-8} and 10^{-6} are mostly proposed to obtain an efficient macroscopic convergence behavior. In this work $\|\delta\mathbf{E}\| = 10^{-6}$ yields sufficiently accurate results.

For an efficient macroscopic Newton algorithm the macroscopic tangent obtained by the perturbation procedure $\mathbf{C}_{\delta\mathbf{E}}$ has to be consistent with the macroscopic stress $\mathbf{\Sigma}$ which is computed during the current macroscopic load iteration. This means, the algorithms for obtaining both quantities have to be compatible with each other. Hence, the type of boundary conditions applied on the RVE for the computation of both macroscopic quantities has to be consistent. This distinction between different types of boundary conditions is redundant if the micro samples fulfill the requirements of being representative for the microstructural setting, because different types of boundary conditions should cause the same effective response, see for instance Hazanov and Huet [1994], Kanit et al. [2003] and Ostoja-Starzewski [2006] for a more detailed discussion. However, in this work, strain driven periodic boundary conditions are applied on the representative microscopic sample for solving the macroscopic load step and the six numerical homogenization load cases.

Moreover, besides the type of boundary conditions, the evolution of the internal variables \mathcal{I} during the perturbation step has to be consistent with the macroscopic load iteration. In this regard, $\mathcal{I}_{\bullet}^n = \mathcal{I}_{\bullet}(\mathbf{E}^n)$ denotes a fixed state of the internal variables which is stored after the macroscopic load iteration t^n . Thereby, the time step is defined by $t^n = t^{n-1} + \Delta t^n$ and a fixed state in the sense that the variables are irreversible from this loading point onwards is marked by '•'. Different techniques concerning the storage, loading and evolution of these variables on the microscale can be used to obtain a consistent macroscopic tangent during the perturbation step. Temizer and Wriggers [2008] proposed to store the internal variables \mathcal{I}_{\bullet}^n at the

end of the current macroscopic load iteration Δt^n and reload this state in advance of each perturbation load case. Performing the subsequent perturbation procedure with frozen internal variables, i.e. $\delta\mathcal{I}(\delta\mathbf{E}) = 0$, leads to an elastic secant stiffness. The macroscopic perturbation stress increment is obtained by the following relation

$$\delta\Sigma^n = \Sigma_{\delta E}(\mathbf{E}^n + \delta\mathbf{E}, \mathcal{I}_{\bullet}^n) - \Sigma(\mathbf{E}^n, \mathcal{I}_{\bullet}^{n-1} + \Delta\mathcal{I}(\mathbf{E}^{n-1}, \Delta\mathbf{E}^n)) . \quad (4.17)$$

Using the secant stiffness leads to slower convergence rates of the macroscopic iterative algorithm, while the convergence with a consistent tangent is quadratic at least in the neighborhood of the solution.

In order to obtain the consistent tangent stiffness the perturbation has to be performed inelastically. This means, the internal variables have to be able to evolve during the perturbation step by $\delta\mathcal{I}(\mathbf{E}^n, \delta\mathbf{E})$, consistent with the evolution during the macroscopic load step $\mathcal{I}(\mathbf{E}^n)$. The stress during the perturbation step $\sigma_{\delta E}(\mathbf{x})$ has to evolve at a local micro point \mathbf{x} along the same elastic or inelastic load path as the stress has evolved during the macro load iteration $\sigma(\mathbf{x})$. If the internal variables are updated at the end of the current macroscopic load iteration Δt^n , the evolution of the variables during the perturbation step has to be treated in a special way. Temizer and Wriggers [2008] proposed the evolution of the internal variables under certain constraint conditions. In dependence of the local evolution history during the current load iteration Δt^n a particular material point of the RVE behaves elastically or inelastically during the perturbation step. That means, if at a certain micro point \mathbf{x} elastic unloading occurred during the macro load iteration, the perturbation at this point is also performed elastically, i.e. with frozen internal variables, even if loading occurs during the perturbation at this point. On the other hand, an inelastic loading step at a micro point is followed from an inelastic perturbation, regardless of whether loading or unloading occurs during the perturbation at this point. This is also valid for damage, where normally the internal variables only increase during a loading step, while elastic unloading occurs always with frozen internal variables. The relation for the macroscopic perturbation stress increment by a constraint inelastic perturbation procedure can be summarized as follows

$$\begin{aligned} \delta\Sigma^n = & \Sigma_{\delta E}(\mathbf{E}^n + \delta\mathbf{E}, \mathcal{I}_{\bullet}^n + \delta\mathcal{I}(\mathbf{E}^n, \delta\mathbf{E})) \\ & - \Sigma(\mathbf{E}^n, \mathcal{I}_{\bullet}^{n-1} + \Delta\mathcal{I}(\mathbf{E}^{n-1}, \Delta\mathbf{E}^n)) . \end{aligned} \quad (4.18)$$

Miehe [1996] proposed an alternative approach for obtaining the consistent tangent stiffness by loading back from the last load step and performing an inelastic perturbation. The internal variables of the former macroscopic load step Δt^{n-1} are reloaded before each perturbation load case and evolve unconstrained (i.e. independent from the current load history) during the perturbation procedure.

In this work, the perturbation is done by applying the current macro load \mathbf{E}^n together with the particular perturbation strain $\delta\mathbf{E}$. According to the scheme shown in Figure 4.3 the macroscopic load step Δt^n is solved by applying the current strain

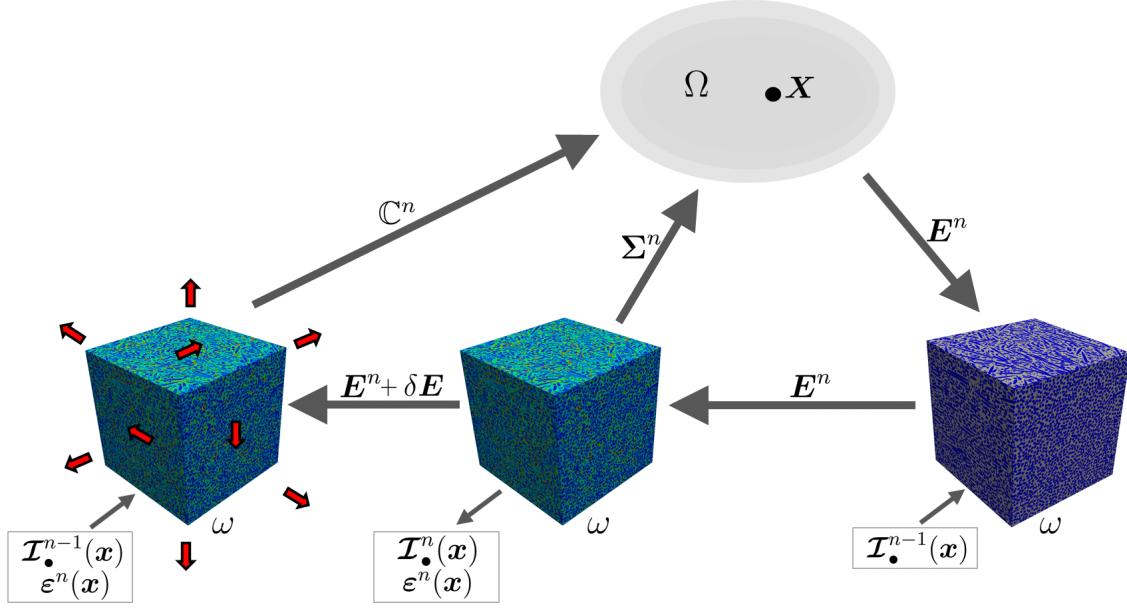


Figure 4.3: Multiscale approach and perturbation procedure schematically.

increment on the RVE

$$\mathbf{E}^n = \mathbf{E}^{n-1} + \Delta \mathbf{E}^n . \quad (4.19)$$

Volume averaging of the resulting microscopic stresses over the whole micro domain ω gives the macroscopic stress

$$\Sigma^n = \frac{1}{|\omega|} \int_{\omega} \boldsymbol{\sigma}^n(\mathbf{x}) \, dv . \quad (4.20)$$

The solution field $\boldsymbol{\varepsilon}^n$ is stored at the end of the current load step and reloaded in each perturbation load case in order to obtain the perturbed solution field with less micro iterations. For each perturbation step the internal variables $\mathcal{I}_{\bullet}^{n-1}$ are loaded from the previous converged macro step t^{n-1} . There is no need to distinct between an elastic or inelastic evolution during the perturbation step, because the internal variables are taken from t^{n-1} and can evolve freely during Δt^n . They evolve inelastically and unconstrained, i.e. they locally increase during a loading step and remain fixed during unloading. The perturbation stress increment for the computation of the macroscopic tangent according to (4.15) is given by

$$\begin{aligned} \delta \Sigma^n &= \Sigma_{\delta E}(\mathbf{E}^n + \delta \mathbf{E}, \mathcal{I}_{\bullet}^{n-1} + \delta \mathcal{I}(\mathbf{E}^n, \delta \mathbf{E})) \\ &\quad - \Sigma(\mathbf{E}^n, \mathcal{I}_{\bullet}^{n-1} + \Delta \mathcal{I}(\mathbf{E}^{n-1}, \Delta \mathbf{E}^n)) . \end{aligned} \quad (4.21)$$

The entire algorithm of the nested multiscale scheme is illustrated in Algorithm 2.



Algorithm 2: Algorithm for the nested multiscale scheme.

The the macroscale is solved by a FEM solver written in C++ programming language. The microscale problem including the numerical homogenization procedure is solved by an encapsulated FFT-based solver which is started in each macroscopic Newton iteration at each macroscopic integration point. The data between both scales are transferred via input and result files. The solution fields and the internal variables of the microstructures are stored in restart files.

Macroscopic Tangent Computation - Convergence Analysis

The size of the perturbation strain is investigated by a numerical example. Within this context two objectives are pursued: On the one hand $\delta \mathbf{E}$ has to be infinitesimally small to obtain a numerical tangent which is close to the analytical one. But on the other side, the perturbation strain must not be too small, to avoid round-off errors, which occur if the machine precision is not accurate enough to identify the small stress increment $\delta \Sigma$ caused by $\delta \mathbf{E}$ correctly.

In order to investigate the size of the perturbation strain, a multiscale test example according to Figure 4.4 is set up. A strip with a hole is coupled in each integration point to only one single homogeneous voxel. The microstructure is modeled with the linear elastic damage model introduced in Section 2.3.2 ($E = 100\text{MPa}$, $H = 0.5$, $Y_0 = 0$). The macrostructure is subjected to a prescribed displacement load which is increased during five time steps. In Figures 4.5 and 4.6 the prescribed macro load and the stress-strain response are shown.

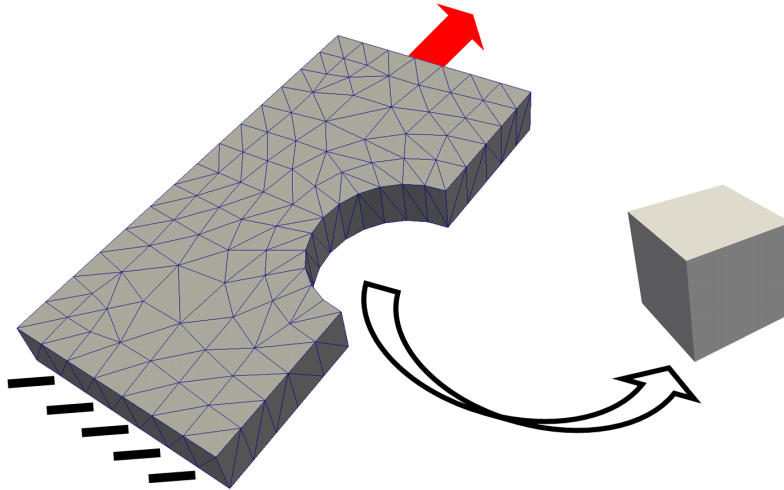


Figure 4.4: Multiscale simulation: Strip with a hole (macro) and a single homogeneous voxel (microscale).

In the case of this simplified example the analytical material tangent \mathfrak{c} of the simple homogeneous microstructure

$$\mathfrak{c} = (1 - d)\mathfrak{c}_e - H e^{-H(\tilde{\varepsilon}(Y) - Y_0)} \frac{1}{\tilde{\varepsilon}(Y)} \boldsymbol{\sigma}_e \otimes \boldsymbol{\sigma}_e, \quad (4.22)$$

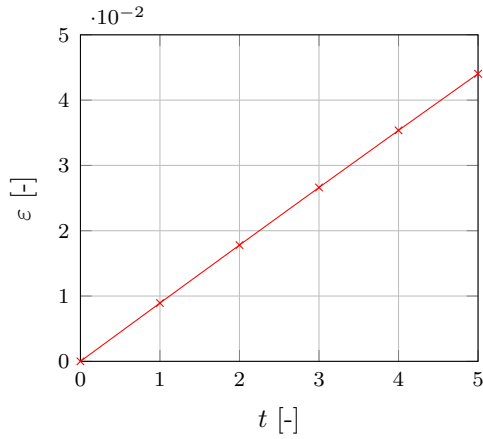


Figure 4.5: Prescribed macroscopic strain applied in five time steps.

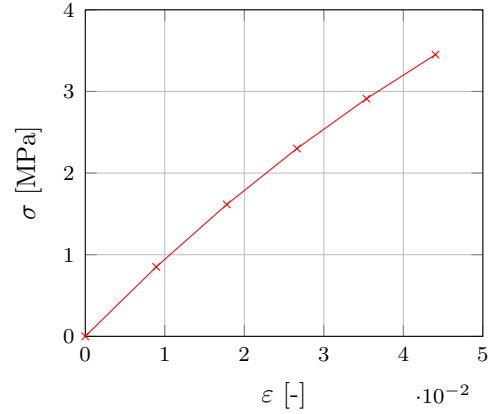


Figure 4.6: Macroscopic stress-strain response.

equals to the effective macroscopic tangent obtained by a homogenization process of the microstructural problem

$$\mathbf{C} = \frac{\partial \Sigma}{\partial \mathbf{E}}. \tag{4.23}$$

Choosing an infinitesimal small perturbation strain $\delta \mathbf{E}$, the numerical tangent $\mathbf{C}_{\delta \mathbf{E}}$ is equal to the microscopic material tangent \mathfrak{c} . In Table 4.1 the macroscopic convergence behavior during the five macroscopic load increments is investigated for different sizes of the perturbation strain. The results are compared to a single scale simulation, where the constitutive equation is directly defined on the macroscale. In this case, the analytical tangent is obtained from the material law itself, instead of using a numerical tangent obtained from an underlying microstructure. The rel-

Load step	Newton Iterations				
	analytical	$\ \delta \mathbf{E}\ = 10^{-6}$	$\ \delta \mathbf{E}\ = 10^{-4}$	$\ \delta \mathbf{E}\ = 10^{-2}$	$\ \delta \mathbf{E}\ = 10^{-1}$
1	4	4	4	5	24
2	4	4	4	5	24
3	4	4	4	5	26
4	4	4	4	5	28
5	4	4	4	5	38

Table 4.1: Number of macro Newton iterations for different perturbation strains $\|\delta \mathbf{E}\|$. Macroscopic convergence criterion: relative residuum $R < 10^{-6}$.

ative residuum of the macroscale problem is shown in Table 4.2 during the last macroscopic load step.

The first component \mathbb{C}_{11} of the homogenized stiffness matrix \mathbf{C} is illustrated in Figure 4.7 in comparison to the value of the analytical one obtained from the micro-

NR iter.	analytical	$\ \delta\mathbf{E}\ = 10^{-6}$	$\ \delta\mathbf{E}\ = 10^{-4}$	$\ \delta\mathbf{E}\ = 10^{-2}$	$\ \delta\mathbf{E}\ = 10^{-1}$
1	$3.85 \cdot 10^{-1}$	$3.60 \cdot 10^{-1}$	$3.60 \cdot 10^{-1}$	$3.50 \cdot 10^{-1}$	$2.63 \cdot 10^{-1}$
2	$1.66 \cdot 10^{-3}$	$4.94 \cdot 10^{-4}$	$4.94 \cdot 10^{-4}$	$5.75 \cdot 10^{-4}$	$1.99 \cdot 10^{-3}$
3	$1.46 \cdot 10^{-5}$	$1.62 \cdot 10^{-5}$	$1.62 \cdot 10^{-5}$	$3.26 \cdot 10^{-5}$	$5.67 \cdot 10^{-4}$
4	$1.12 \cdot 10^{-9}$	$2.86 \cdot 10^{-7}$	$2.94 \cdot 10^{-7}$	$2.34 \cdot 10^{-6}$	$2.83 \cdot 10^{-4}$
5				$2.55 \cdot 10^{-7}$	$1.70 \cdot 10^{-4}$
6					$1.10 \cdot 10^{-4}$
...					...
38					$4.98 \cdot 10^{-7}$

Table 4.2: Relative macroscale residuum R for the last load increment over Newton iterations for different perturbation strains $\|\delta\mathbf{E}\|$. Macroscopic criterion: $R < 10^{-6}$.

scopic constitutive law \mathfrak{c} . The matrix component \mathbb{C}_{11} is shown for different values of the perturbation strain during the last (fifth) macro load step. In Figure 4.8 the relative error of the numerical tangent is depicted in relation to the analytical material tangent.

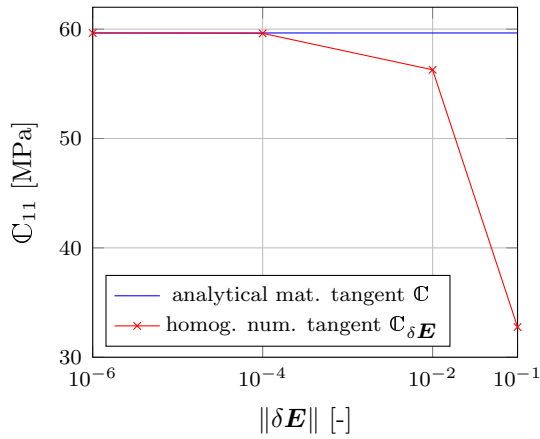


Figure 4.7: Homogenized Voigt matrix component \mathbb{C}_{11} for different perturbation sizes compared to the analytical material stiffness value.

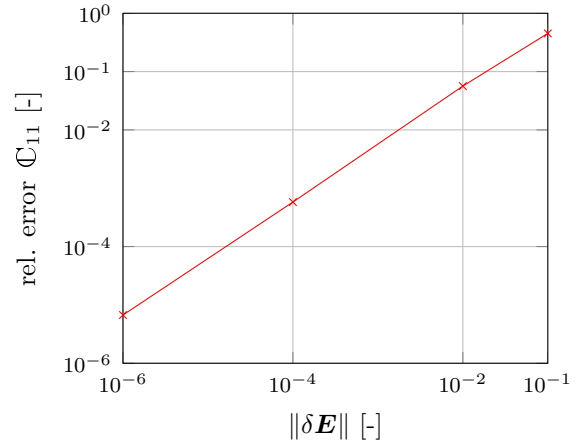


Figure 4.8: Relative error $|(\mathbb{C}_{11} - \mathbb{C}_{11 \delta E}) / \mathbb{C}_{11}|$ for different perturbation sizes.

In the following the analytical material tangent \mathfrak{c} and the homogenized macro tangent \mathbf{C} obtained with a perturbation size of $\|\delta\mathbf{E}\| = 10^{-6}$ during the last load step are shown.

$$\mathfrak{c} = \begin{bmatrix} 59.6480 & 0.0000 & 0.0193 & 0.0164 & 0.1226 & 0.9617 \\ 0.0000 & 78.5573 & 0.0000 & 0.0000 & 0.0000 & 0.0000 \\ 0.0193 & 0.0000 & 78.5573 & 0.0000 & 0.0001 & 0.0010 \\ 0.0164 & 0.0000 & 0.0000 & 39.2787 & 0.0001 & 0.0008 \\ 0.1226 & 0.0000 & 0.0001 & 0.0001 & 39.2779 & 0.0062 \\ 0.9617 & 0.0000 & 0.0010 & 0.0008 & 0.0062 & 39.2298 \end{bmatrix}$$

$$\mathbf{C}_{\delta E} = \begin{bmatrix} 59.6476 & 0.0000 & 0.0193 & 0.0164 & 0.1226 & 0.9617 \\ 0.0000 & 78.5573 & 0.0000 & 0.0000 & 0.0000 & 0.0000 \\ 0.0193 & 0.0000 & 78.5573 & 0.0000 & 0.0001 & 0.0010 \\ 0.0164 & 0.0000 & 0.0000 & 39.2787 & 0.0001 & 0.0004 \\ 0.1226 & 0.0000 & 0.0001 & 0.0001 & 39.2783 & 0.0031 \\ 0.9617 & 0.0000 & 0.0010 & 0.0004 & 0.0031 & 39.2542 \end{bmatrix}$$

The value for the perturbation strain $\|\delta\mathbf{E}\| = 10^{-6}$ yield sufficiently accurate results for obtaining an efficient algorithm on the macroscale and was used for computing the multiscale examples in this work.

4.4 Onset of Macroscopic Failure

In some cases, e.g. in the case of softening material behavior, the assumption of the separation of the geometrical scales and thus, the basic theory of homogenization is no longer valid. Microscopic failure leads to the loss of ellipticity of the governing macroscopic differential equation and consequently the macroscopic problem becomes ill-posed (see Hill [1962] and Rice and Rudnicki [1980]). Occurring localized micro cracks lead to evolving macro cracks and special scale coupling techniques are necessary to describe failure evolution on the coarse scale. For instance, Belytschko et al. [2008] proposed a method, called multiscale aggregating discontinuities, which allows to transport a discontinuity between the scales. The latter is injected at the macroscale by the extended finite element method. Coenen et al. [2012] established a special multiscale framework which enables the incorporation of a shear band into the microstructural sample and an effective displacement jump is transported to the macroscale. The failed micro material sample isn't any more representative for the whole microstructural behavior and consequently it is denoted as microstructural volume element. In this context, Linder and Raina [2013] used the embedded strong discontinuity approach (see Linder and Armero [2007]) to model solids at failure on multiple scales.

This work is only related to pre-failure material behavior i.e. the state before localization of the macroscale occurs and consequently the separation of scales remains valid. The micro samples can be regarded as RVEs. The point when the microscopic boundary value problem loses its ellipticity can be regarded as the onset of macro-

scopic failure. According to Hill [1962] and Rice and Rudnicki [1980] the failure onset is detected by an analysis of the acoustic tensor of the current homogenized tangent stiffness tensor. The acoustic tensor $\mathbf{A}(\mathbf{n})$ is calculated by the macroscopic tangent stiffness \mathbf{C} and all possible orientations \mathbf{n} (see de Borst et al. [1993], Han et al. [2009])

$$A_{jk}(\mathbf{n}) = \mathbb{C}_{ijkl} n_i n_l \quad (4.24)$$

$$\mathbf{n} = \mathbf{n}(\varphi, \theta) \quad (4.25)$$

$$\|\mathbf{n}\| = 1, \quad (4.26)$$

where the definition of the acoustic tensor \mathbf{A} is given in index notation. The orientations \mathbf{n} can be expressed in spherical coordinates by two angles φ and θ . Localization occurs, if the following criterion is fulfilled for any direction \mathbf{n} :

$$\det \mathbf{A}(\mathbf{n}) = 0. \quad (4.27)$$

We demonstrate this analysis on a cubic RVE containing a single linear elastic fiber inclusion (see Figure 4.9). The matrix material is modeled with the linear elastic damage model introduced in Section 2.3.2 ($E = 2.8\text{GPa}$, $\nu = 0.3$, $H = 0.5$, $Y_0 = 0$) and the fibers behave linear elastic ($E = 72\text{GPa}$, $\nu = 0.2$). The structure is discretized by $75^3=421,875$ voxel cells and loaded during 10 time steps with a uniaxial macroscopic strain perpendicular to the fiber direction.

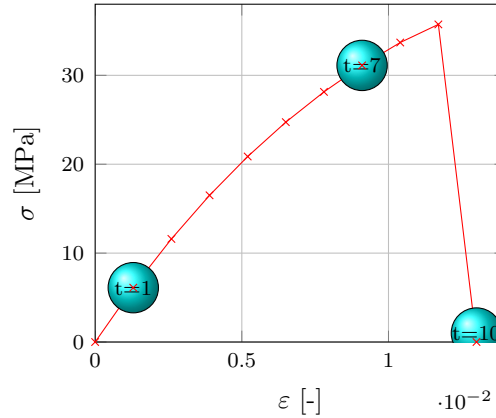
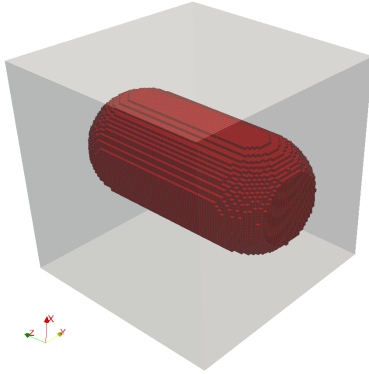


Figure 4.9: Unit cell containing a single elastic fiber.

Figure 4.10: Stress-strain plot of the failed micro structure.

In each time step the homogenized macroscopic tangent is computed by numerical linearization. Subsequently, the determinant of the acoustic tensor is calculated for all directions. In practice, the determinant is calculated for discrete angles φ and θ with an increment of 1° to 5° . In Figure 4.11, at the bottom, the normalized determinant of the acoustic tensor is plotted in all directions using spherical coordinates (r, φ, θ) . Thereby the value of the determinant is illustrated as the spherical radius. The initial value of the radius $r = 1$ in each direction at $t = 0$ decreases

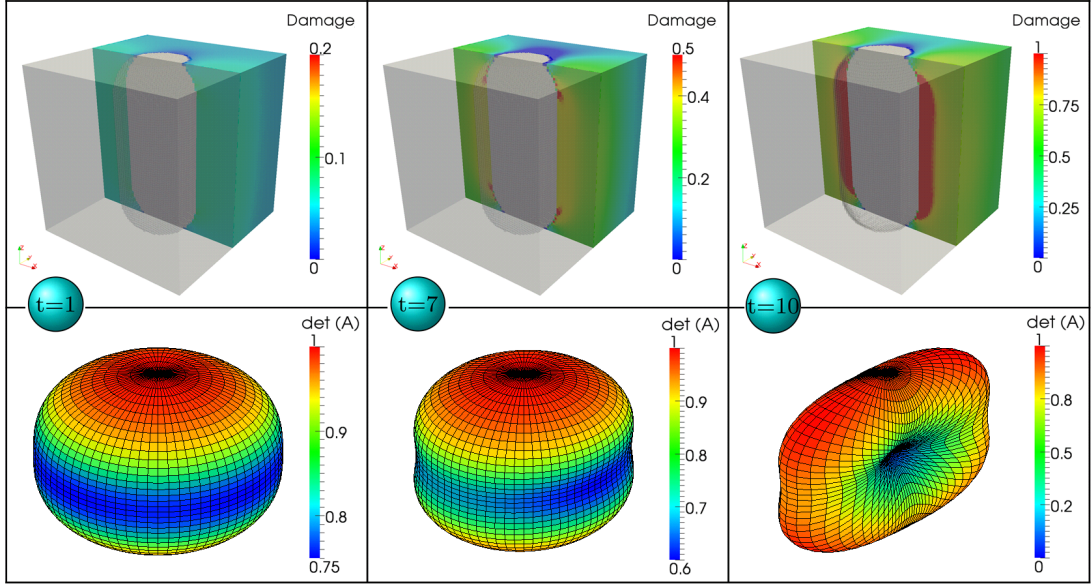


Figure 4.11: Detection of the onset of macroscopic failure with the acoustic tensor (below) and corresponding micro damage fields (above).

with growing damage in the direction which is perpendicular to the failure direction. The corresponding damage field of the microstructure is shown on the top in Figure 4.11 for the selected time steps.

Furthermore, similar to the investigation described in the previous section, the influence of the perturbation size is analyzed for this example. In Figure 4.12 the component \mathbb{C}_{11} of the homogenized Voigt matrix obtained after load step $t = 1$, $t = 6$ and $t = 7$ is illustrated for different perturbation sizes.

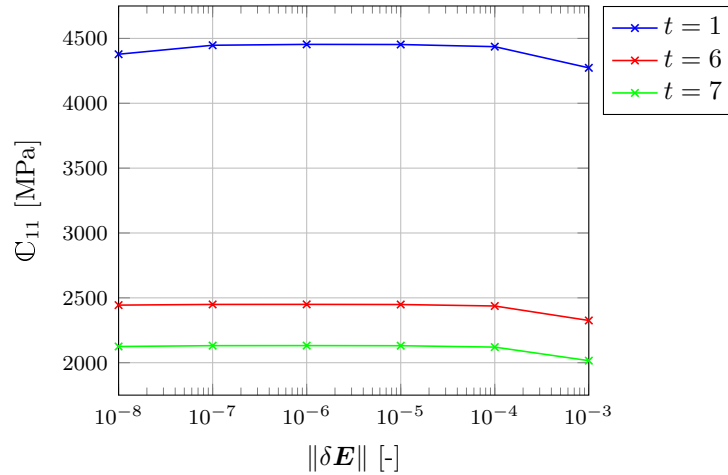


Figure 4.12: Component \mathbb{C}_{11} of the homogenized Voigt matrix for different perturbation sizes after load step $t = 1$, $t = 6$ and $t = 7$.

The value increases for smaller perturbation sizes, because the analytical macro tangent is met more precisely. In the range between $\|\delta\mathbf{E}\| = 10^{-5}$ and $\|\delta\mathbf{E}\| = 10^{-7}$ the stiffness remains stable and decreases again for $\|\delta\mathbf{E}\| = 10^{-8}$, due to the limitation in the existing machine precision. Hence, best results are obtained by choosing perturbation sizes in a stable range $10^{-5} \leq \|\delta\mathbf{E}\| \leq 10^{-7}$.

Chapter 5

Numerical Examples

5.1 Microscale Computations

The microscopic problem is solved using the FFT code FeelMath developed at the Fraunhofer ITWM. In some numerical examples the convergence behavior of the numerical method and the micromechanical damage behavior of fiber reinforced composite materials are investigated. The numerical results are validated with experimental data. Furthermore, in the second part of this chapter, the scale coupling technique is illustrated by some numerical multiscale examples.

5.1.1 Convergence Microscale Model

In the following example the convergence behavior of the microscopic model is shown. The cubic microstructure depicted in Figure 5.1 contains an elastic spherical inclusion and is discretized by 10^6 voxel cells. The behavior of the inclusion is assumed to be linear elastic, while for the polymer matrix the elastic isotropic damage model described in Section 2.3.2 is used. The structure is subjected to a periodic deformation load which is applied in x -direction. The problem is solved numerically using

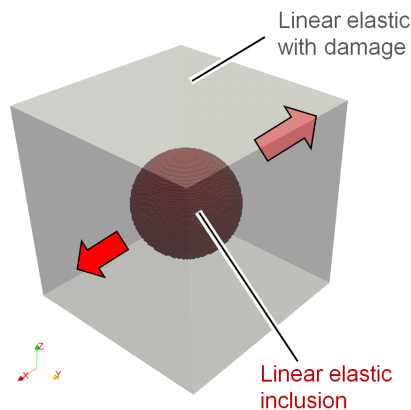


Figure 5.1: Microscopic setup of the single inclusion test.

the Lippmann-Schwinger equation and the FFT based basic scheme described in Section 3.2.6. During one nonlinear load step the two different convergence criteria according to (3.107) and (3.108) are analyzed. Furthermore, a third criterion is demonstrated, which is calculated by the difference between the norm of the strain

fields of two successive iterations

$$\frac{|\|\boldsymbol{\epsilon}^{i+1}\|^2 - \|\boldsymbol{\epsilon}^i\|^2|}{\|\mathbf{E}\|^2} \leq \text{tol} . \quad (5.1)$$

This criterion is very efficient in terms of memory consumption, because only the norm of the strain field has to be stored in each iteration instead of the entire field of the solution. As illustrated in Figure 5.3 the two conventional criteria behave very stable, while the strain error (Equation (3.108), red curve) decreases faster than the error of the equilibrated stress field (Equation (3.107), blue curve). For this reason the typical tolerance value of 10^{-10} is much smaller in comparison to 10^{-5} for the error of the stress field. The memory optimized criterion (Equation (5.1), green curve) seems to be unstable in some areas and has to be used with caution. The resulting damage field is shown in Figure 5.2.

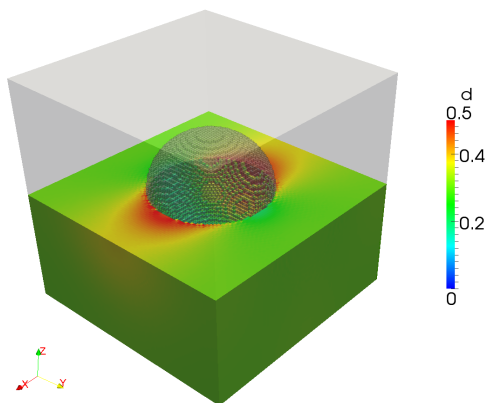


Figure 5.2: Microscopic damage field of the single inclusion test.

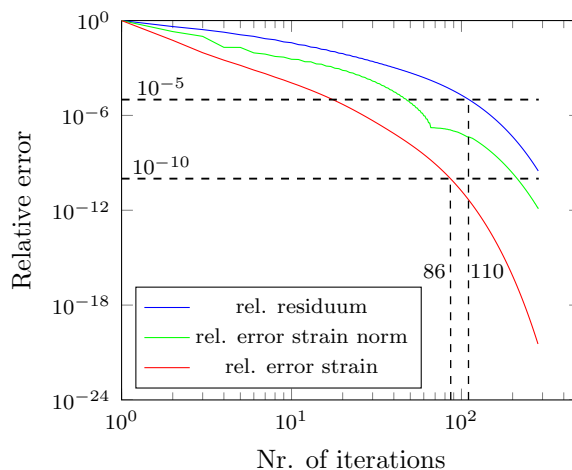


Figure 5.3: Relative error of the inclusion problem over the number of FFT iterations.

5.1.2 Microscopic Failure Mechanisms in Fiber Reinforced Composites

Fracture and progressive damage of fiber reinforced composite materials occur as a result of complex microstructural damage mechanisms. It is important to consider these microstructural effects in order to be able to understand and to predict macroscopic damage evolution. Several authors investigated micromechanical failure mechanisms in short glass fiber reinforced thermoplastic materials using microscopic image processing techniques, like computer tomography (CT) or scanning electron microscopy (SEM). In this regard, polypropylene (see Michler [2008] and Schossig [2011]), polyamide (see Horst and Spoormaker [1997], Horst et al. [1998] and Sato et al. [1991]) or polybutylene terephthalate (see Hoffmann [2012]) are considered. The main mechanisms are damage in the matrix material, fiber pull out and fiber

breakage. The dominating micromechanical mechanism strongly depends on the adhesion between fibers and matrix material. Horst and Spoormaker [1996, 1997] investigated the influence of moisture and different loading conditions on the adhesion. They observed that monotonic tensile loads applied in fiber direction lead to pure shear stresses in the fiber matrix interface and consequently, the matrix material fails. Conversely, cyclic fatigue loads cause in addition to the above-mentioned shear stresses additional tensile stresses on the interface, due to ductile contraction of the matrix material. These additional normal tensile stress components lead to classical fiber debonding and the composite fails directly in the interface.

The fiber matrix bond quality can be analyzed by considering micrographs of pulled out fibers. Sato et al. [1991] observed that the fibers are still covered with matrix material, which implies that the adhesion of the matrix material and the fibers at the interface is quite good. The same observations are made by Hoffmann [2012]. Figure 5.4 shows adhered matrix material in a SEM micrograph of a pulled out fiber. Injection molded composite materials are treated with additives to increase

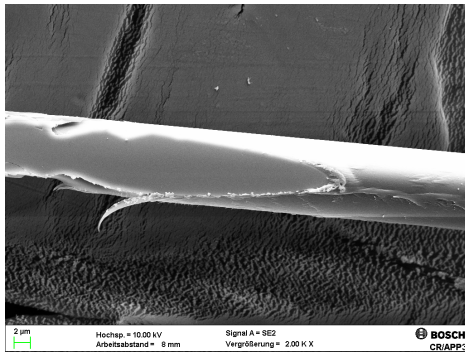


Figure 5.4: Pulled out glass fiber still covered with PBT matrix material. SEM micrograph from Hoffmann [2012].

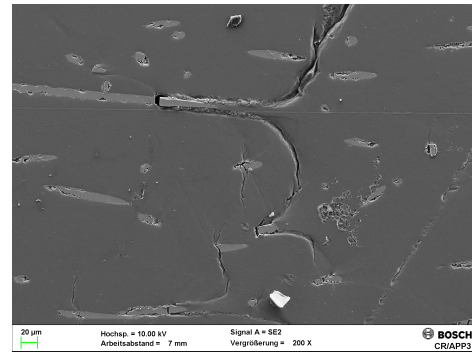


Figure 5.5: SEM analysis of evolving microcracks in PBT GF10. Micrograph from Hoffmann [2012].

the bonding between fibers and matrix material. The analyses of the micrograph shows that by the use of modern coating technologies the adhesion of glass fibers and thermoplastic matrix materials is basically sufficient for transferring the existing loads through the interface into the fibers.

In the following, different mechanisms occurring on the micromechanical level are considered. The microstructure shown in Figure 5.6 contains two single fibers and is subjected to a periodic deformation load applied in fiber direction. In Figure 5.7, micromechanical simulations are compared with micrographs obtained by scanning electron microscopy analyses of an injection molded short fiber reinforced thermoplastic composite. The micrographs are taken from Sato et al. [1991] and Hoffmann [2012], the latter are provided by the Robert Bosch GmbH. Damage starts growing at the fiber tips (Figure 5.7 a). This can be explained by the fact that the pre-coated fibers are broken during the compounding and injection molding process. These broken ends are usually not covered with adhesion agent any more and, therefore, are not well bonded to the matrix material. Furthermore, due to the applied tensile

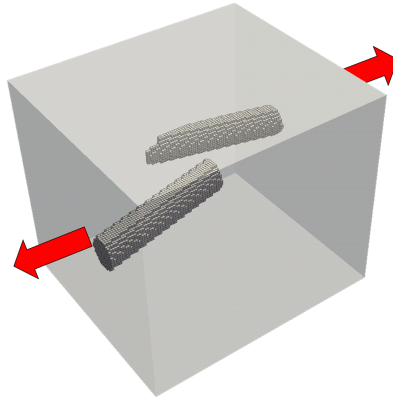
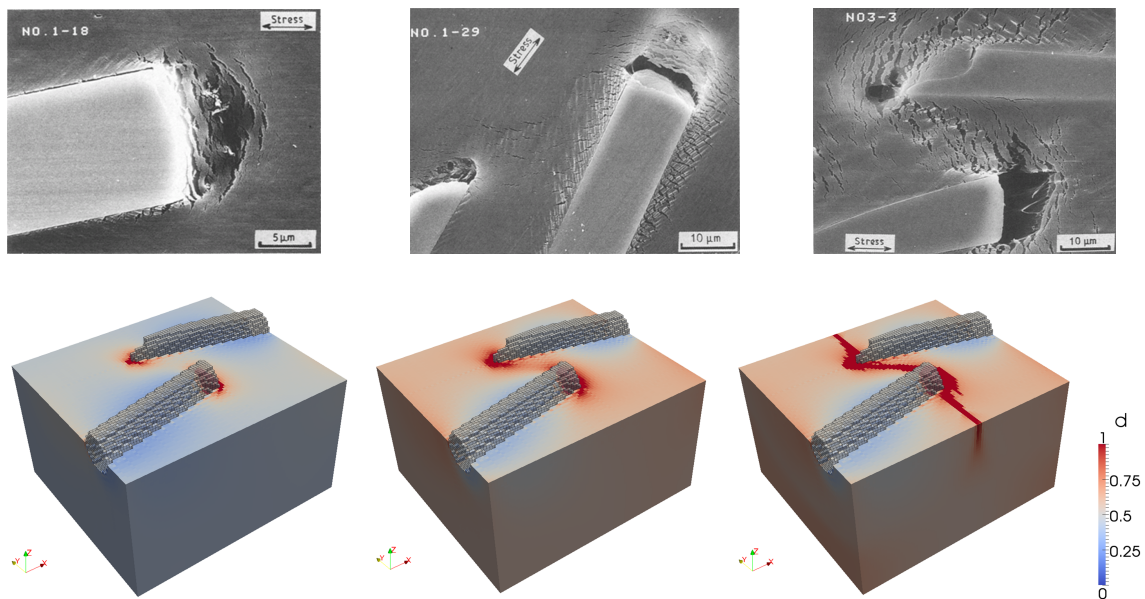


Figure 5.6: Boundary conditions for single fiber RVE computations.



(a) Microcracks in the matrix around the fiber tips.

(b) Microvoids at fiber tips and damage propagation along the interface.

(c) Evolving shear bands between fiber tips.

Figure 5.7: Microscopic damage evolution observed in scanning electron microscopy analyses for PA GF (top) and micro simulations (bottom). Micrographs from Sato et al. [1991].

load along the fiber axes stress concentrations occur at the sharp edges of the fiber ends. Voids grow at the fiber tips and the damage zone propagates along the fiber axes in the interface area between fiber and matrix material (Figure 5.7 b). This cohesive failure occurs in the matrix material close to the fiber interface due to shear stress concentrations along the fiber sides. The interface itself does not fail by simple debonding, which indicates a good fiber matrix adhesion. Damage effects are localized around the interface area and develop in isolated zones. With increasing load shear bands evolve connecting the isolated zones until global failure of the composite occurs (Figure 5.7 c). Within the SEM image depicted in Figure 5.5 evolving micro cracks are shown in a thermoplastic PBT material reinforced with 10 per cent glass fibers.

Generally, the mechanisms observed by SEM analyses of glass fiber reinforced polymers are captured very well by the micromechanical simulation. The simulation can further be used to identify the local mechanisms up to global composite failure in dependence of the microstructural setting and applied loading conditions. The computed effective composite response can be applied in a coupled multiscale simulation to predict the macroscopic structural failure behavior.

5.1.3 Experimental Validation with a Short Fiber Reinforced Thermoplastic Material

Within this example an experimental validation of the microscopic numerical method applied in this work is demonstrated. Therefore, a modified form of the elastoplastic damage model of Ju [1989] introduced in Section 2.3.3 is used to simulate the mechanical behavior of a short fiber reinforced injection-molded composite material. The experimental data are taken from Hoffmann [2012] and kindly provided by the Robert Bosch GmbH in digital form. In the first section the experimental parameter identification and the validation of the matrix material are shown. Furthermore, monotonic and cyclic tensile tests on the composite material with different fiber orientation distributions are compared with unit cell computations.

The material under consideration is polybutylene terephthalate (PBT) and E-glass fibers of 30 % mass fraction. The material parameters listed in Table 5.1 are either obtained by experimental results (see Hoffmann [2012]) or taken from the particular indicated source.

	PBT	E-glass fibers	PBT-GF30
Fiber mass / volume fraction [%]			30.0 / 18.2
Fiber diameter / av. length [μm]			10 / 250
Young's modulus [MPa]	2500	72000	9800 ⁶
Poisson ratio [MPa]	0.35	0.2	
Strain at breakage [%]	20-50 ⁶	3-4.8 ⁶	2.5 ⁶
Maximum strength [MPa]	50-60 ⁶	2000-3500 ⁶	130-150 ⁶

Table 5.1: Material parameters of PBT, glass fibers and composite material.

Matrix Material - Experimental Parameter Identification

The parameters of the matrix material model, namely σ_Y , ε_p and d , are obtained by the 1D stress-strain response of a uniaxial cyclic tensile test. Therefore an injection-molded standard tensile bar is loaded with gradual increasing prescribed strain according to Figure 5.8. The tests are performed at room temperature and a strain rate of $\dot{\varepsilon} = 10^{-3}/\text{min}$. In the unloading phase the load is decreased until the stress in the sample equals zero. Within the resulting stress strain diagram shown in

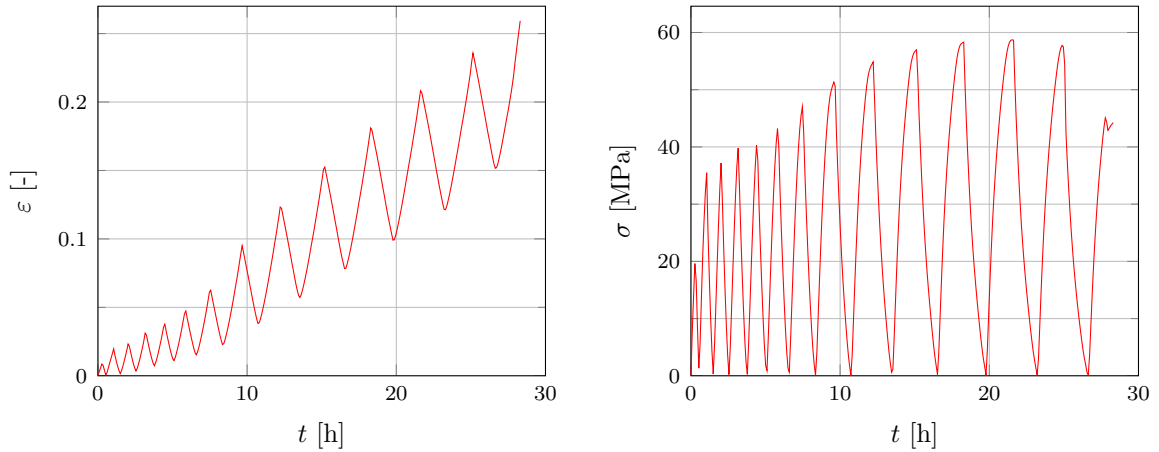


Figure 5.8: Experimental applied cyclic strain and stress response of the thermoplastic matrix material.

Figure 5.9 the parameters can be obtained for each load cycle. Thereby the yield stress σ_Y corresponds to the maximal stress point reached during a cycle. After subsequent unloading the residual strain at zero stress equals the irreversible plastic strain ε_p . The elastic strain ε_e is the reversible strain that is required to obtain the zero stress point during the unloading path, it is calculated by the difference of the total strain ε_{tot} and the plastic strain ε_p . Finally, the decreased Young's modulus E_d is obtained by the slope of the unloading path, setting the elastic strain to relation with the corresponding yield stress. The decrease of the elastic stiffness gives the damage variable d with the following expression:

$$d = 1 - \frac{E_d}{E_0} \quad E_d = \frac{\sigma_Y}{\varepsilon_{tot} - \varepsilon_p} = \frac{\sigma_Y}{\varepsilon_e} . \quad (5.2)$$

The decrease of the Young's modulus E_d results in an increase of the damage variable d during each cycle. The obtained parameters of the matrix material for each load cycle are listed in Table 5.2.

⁶see Baur et al. [2013]

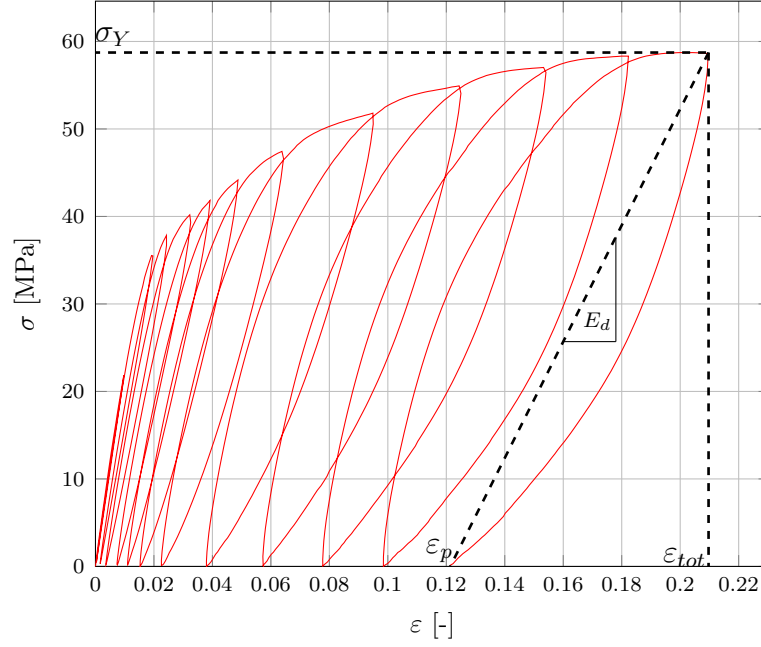


Figure 5.9: Material parameter identification with the experimental cyclic stress strain response of the thermoplastic matrix material.

cycle	σ_Y [MPa]	ε_p [-]	d [-]	ε_{tot} [-]
1	44.64	0.0065	0.322	0.0328
2	51.36	0.0218	0.519	0.0645
3	56.34	0.0391	0.599	0.0953
4	58.78	0.0562	0.659	0.1252
5	60.38	0.0779	0.683	0.1542
6	61.88	0.1001	0.699	0.1823
7	62.68	0.1224	0.713	0.2097

Table 5.2: Identified material parameters of the matrix material model.

Matrix Material - Validation

The material behavior is defined by the elasto-plastic material law introduced in Section 2.3.3 and implemented into the FFT-based solver FeelMath. Finding suitable analytical functions and material parameters which describe the damage and hardening evolution of the plastic matrix material is in general a difficult task. Defining the material behavior by linear interpolation between the measured tabular values proved to be a more simple and accurate way to reproduce the experimental results. Thereby current values of damage variable and yield stress are interpolated between discrete points by piecewise linear functions of the current plastic and total strain. The measured tabular values and the corresponding strains are listed in Table 5.2. According to the effective stress concept introduced in Section 2.3.3 the yield stress is recognized in the material model by its undamaged effective value. Consequently, the plastic return mapping is performed in the effective stress space. The damage step follows subsequently without any additional iteration.

Similar to the experimental tensile test the cyclic strain load is applied on the structure by increasing the macroscopic strain tensor \mathbf{E} in one direction. For obtaining an uniaxial stress state, according to the experimental setting, mixed BCs with stress free conditions on the remaining boundaries are chosen. The resulting stress

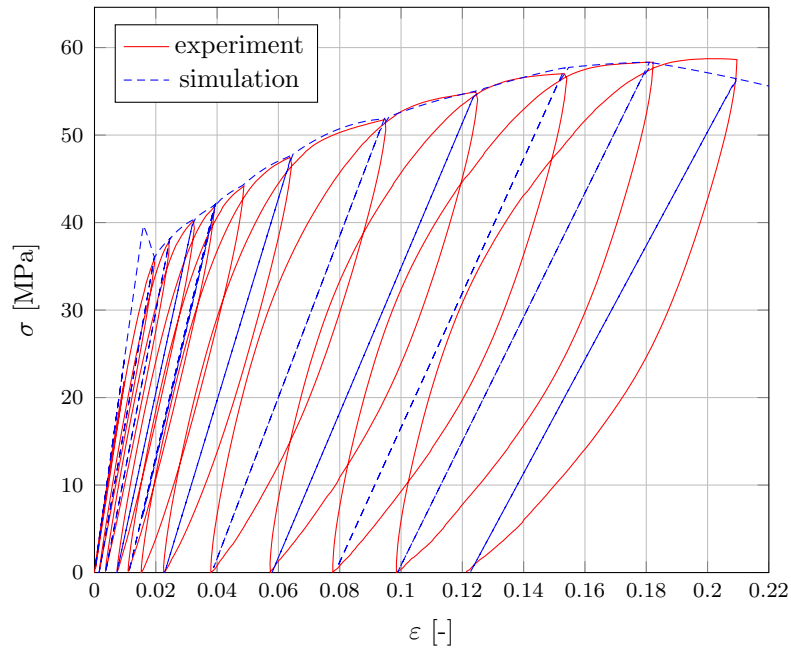


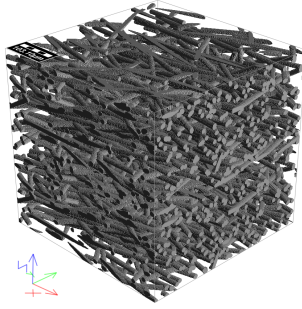
Figure 5.10: Experimental and simulated cyclic stress strain response of the matrix material.

strain curve and the experimental curve are depicted in Figure 5.10. The nonlinear stress strain behavior, the residual plastic strain as well as the degraded Young's modulus are well predicted by the computational model. Due to the fact that kinematic hardening is neglected in the plastic material law, the hysteresis loops of the experimental curves are not captured.

Remark: Due to the high relaxation times of PBT the experimental results are also influenced by time dependent viscoelastic effects. Despite the very low strain rate of $\dot{\epsilon} = 0.1\%/min$ the hysteresis is reduced to an acceptable level, but the equilibrium stress and strain state is not finally reached.

Composite Material - RVE generation

For the simulation of the composite material behavior, representative unit cells are created. With the software Geodict [2014] realizations of stochastic micro structures are generated characterized by the orientation, content, and geometry of their inclusions. Length, diameter, and volume fraction of the fibers are chosen according to the measured data listed in Table 5.1. Concerning the fiber orientation, injection molded parts are characterized by a certain symmetrical layer structure. Hence, the RVEs are divided in three layers with different fiber orientations. The measured components of the fiber orientation tensor over the sample thickness ($t = 2mm$) are listed in Table 5.3. The second order tensor a_{ij} is obtained from the distribution



Layer	t [mm]	a_{xx}	a_{yy}	a_{zz}
1	0.89	0.755	0.204	0.041
2	0.22	0.454	0.505	0.041
3	0.89	0.755	0.204	0.041

Figure 5.11: RVE structure with three fiber orientation layers through the thickness.

Table 5.3: Diagonal components of the measured fiber orientation tensor a_{ij} in the layers.

function $\Psi(\mathbf{n})$ that describes the probability of fibers being oriented in a particular direction n_i

$$a_{ij} = \oint n_i n_j \Psi(\mathbf{n}) . \quad (5.3)$$

In the RVE realization illustrated in Figure 5.11 the fibers are mainly aligned in x -direction. The thinner middle layer also contains a significant portion of fibers which are oriented in y -direction. This layer structure is usually observed in injection molded samples with x as the melt flow direction during the manufacturing process. In the following tensile tests are shown in variation of the loading direction \mathbf{n}

$$\mathbf{n} = \begin{pmatrix} \cos \varphi \\ \sin \varphi \\ 0 \end{pmatrix} , \quad (5.4)$$

namely in $\varphi = 0^\circ, 45^\circ$ and 90° with respect to the main fiber orientation. Therefore three experimental specimens are cut from an injection molded plate relative to the

melt flow direction. For simulating the elastic properties the same RVE is used and the anisotropic properties are obtained by simply rotating the loading direction.

Composite Material - Elastic Properties

In the first validation step the elastic properties of the RVE are tested. Therefore, the geometrical fiber properties as well as the linear elastic material parameters of fibers and matrix according to Table 5.1 are chosen. The cubic RVE is discretized by 127 voxel cells in each spatial direction. Assuming a voxel edge length of $2.5 \mu\text{m}$ the total length of the RVE is $L=317.5 \mu\text{m}$. Choosing an average fiber length of $l=250 \mu\text{m}$ yields the ratio for fiber length to RVE edge length of $l/L=0.79$. The elastic stiffness and compliance tensor, respectively, are obtained during a numerical homogenization process, by applying six mechanical load cases according to Section 4.3 at a single RVE structure. Hence, the directional dependent Young's modulus $E(\mathbf{n})$ can be represented as a function of the loading direction \mathbf{n} , see Figure 5.12. According to Böhlke and Brüggemann [2001], Böhlke [2001] and Müller [2001] $E(\mathbf{n})$ is obtained by decomposing the homogenized compliance tensor \mathbf{S} in the spatial directions \mathbf{n}

$$\frac{1}{E(\mathbf{n})} = (\mathbf{n} \otimes \mathbf{n}) : (\mathbf{S}(\mathbf{n} \otimes \mathbf{n})) . \quad (5.5)$$

The spatial distribution of the simulated RVE is plotted in Figure 5.12. The Young's

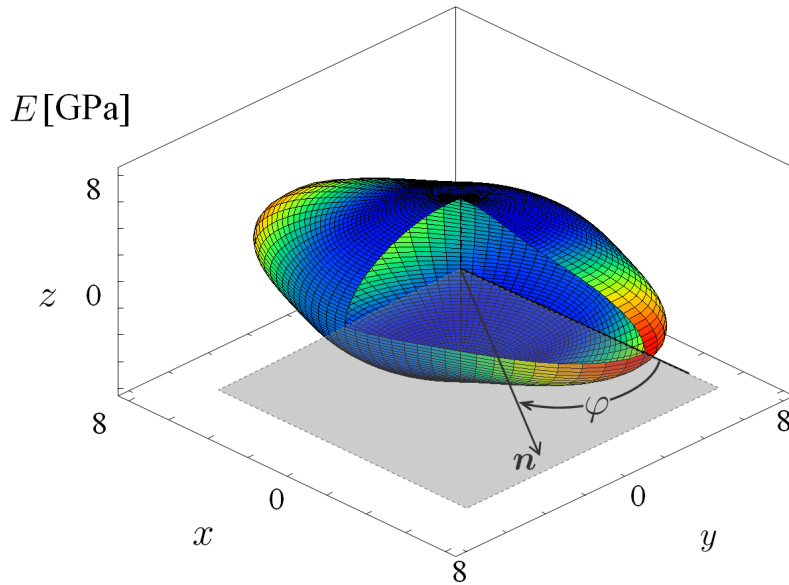


Figure 5.12: Graphical representation of the directional dependent Young's modulus $E(\mathbf{n})$.

moduli for the three loading directions can be identified by the corresponding spatial directions in the distribution. Whereby the values for the 0° and 90° direction correspond to the values in the x - and y -direction in the xy -plane of the distribution, and the 45° , to the bisector of x - and y -axes, respectively.

Simulated and measured values of the Young's modulus for different directions in the xy -plane are illustrated in Figures 5.13 and 5.14. Both values show very good

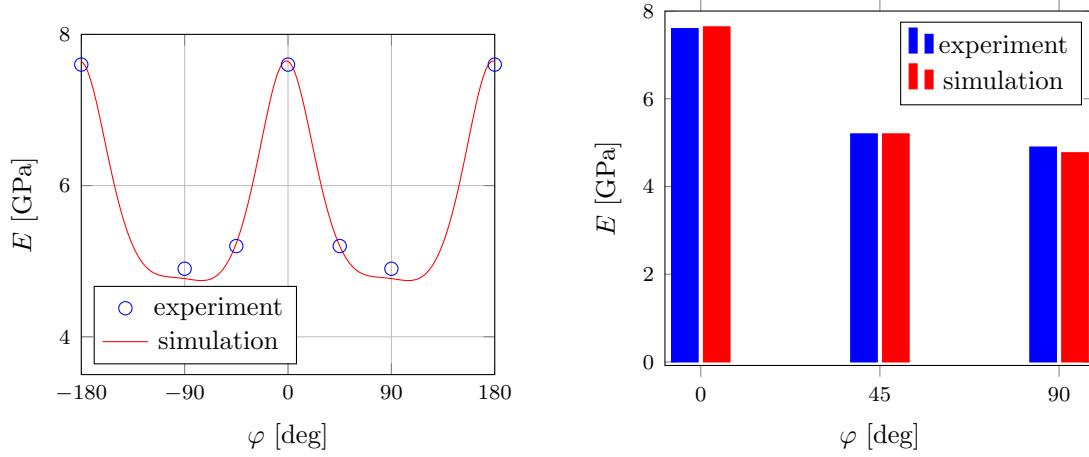


Figure 5.13: Experimental and simulated Young's modulus over angle φ in xy -plane.

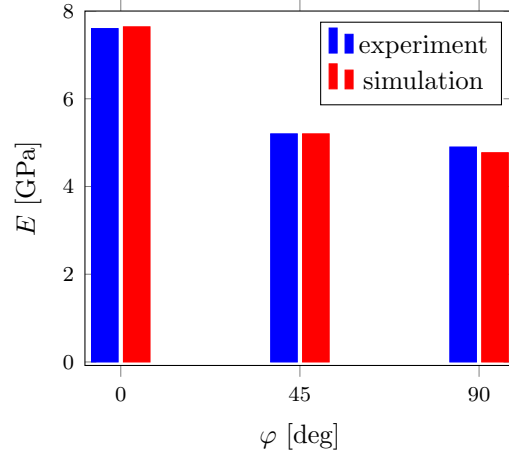


Figure 5.14: Experimental and simulated Young's modulus for different angles φ in xy -plane.

agreement which indicates that the anisotropy of the elastic constants are captured very accurately by the microstructural setting. The results show, that the linear elastic properties of complicated micro structures can be predicted very well with the applied numerical homogenization method. Simply the elastic material parameters for fiber and matrix material have to be known. Concerning the micro structural setting only the diagonal components of the second order fiber orientation tensor as well as length and diameter of the fibers are known. In this work an average fiber length is chosen. However, in real micro structures the fibers length would vary locally in dependence of the manufacturing process. Furthermore, the tensor components do not contain the complete information about the orientation as it would be the case for a CT scan of the real micro structure. Thus, several statistically similar realizations of the micro structural models are possible. However, even if not the complete geometrical information of the micro structural setting is available, the anisotropic stiffness could be predicted very well. The elastic properties are determined for different realizations and sample sizes and the smallest representative micro structure consisting of approximately two million voxels is chosen for the following nonlinear simulations.

Composite Material - Monotonic Nonlinear Properties

In the following, monotonic tensile tests ($\dot{\varepsilon} = 10^{-3}/\text{min}$) for the different loading directions are compared to experimental results. While the nonlinear material behavior of the thermoplastic matrix material is modeled with the elasto-plastic material model, the fibers are assumed to behave linear elastic. Thus, fiber breakage is not considered in these simulations. The 0° and 90° simulations are performed on the same RVE sample which is used for the elastic simulations. The 0° test is

given by the effective stress-strain response in x -direction, which corresponds to the direction of the main fiber alignment. The 90° response is obtained by applying the load in y -direction, perpendicular to the main fiber orientation. The load is applied in several time steps in x - and y -direction, respectively. For obtaining the 45° results the fiber orientation tensors are rotated by 45° and a second RVE is generated with the same layer structure. The load is applied in x -direction. Experimental and simulated results for each direction are illustrated in Figure 5.15.

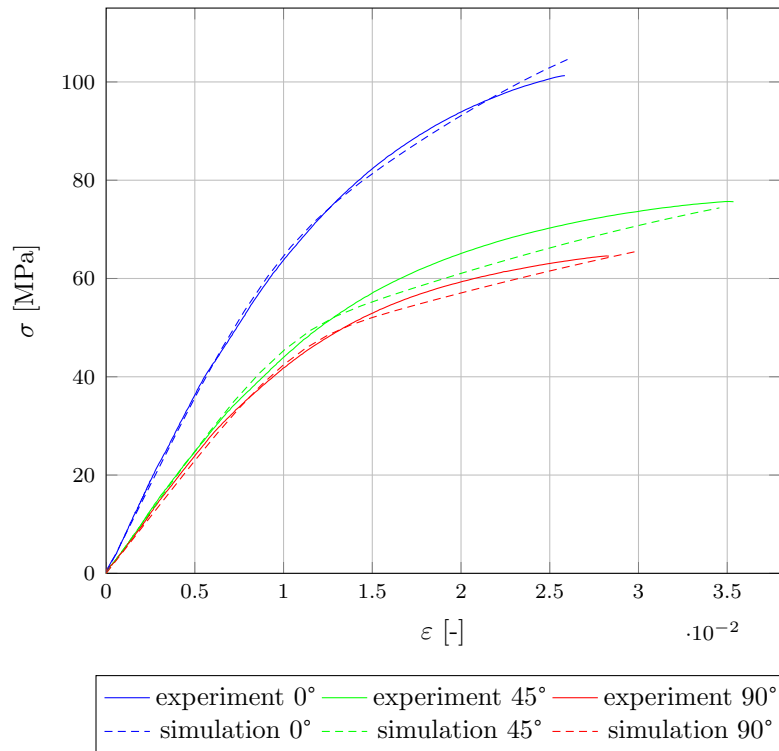


Figure 5.15: Experimental and simulated stress-strain curves for different loading angles φ .

Basically, the simulated stress-strain curves agree well with the measured data. The linear elastic behavior and the transition to a nonlinear stress-strain regime are captured almost perfectly. At higher strains the local values of the plastic strain and damage exceed the measured values and are interpolated linear. Furthermore, fiber breakage is not taken into account and hence, the slope of the curve for the 0° simulation is too high at the very end. In Figures 5.16 and 5.17 the distribution of the damage variable and plastic strain are shown for the different loading directions.

The von Mises stress is depicted in Figure 5.18. One can observe that in each loading direction the maximum stress in some fibers is close to the critical value of 2000 MPa. Thus, fiber breakage is possible in each structure. The highest stresses are reached in fibers which are aligned in the particular load direction. Consequently, fiber breakage will affect mainly the results in the 0° direction, because here most of the fibers are aligned in load direction. In the 90° direction most of the fibers in

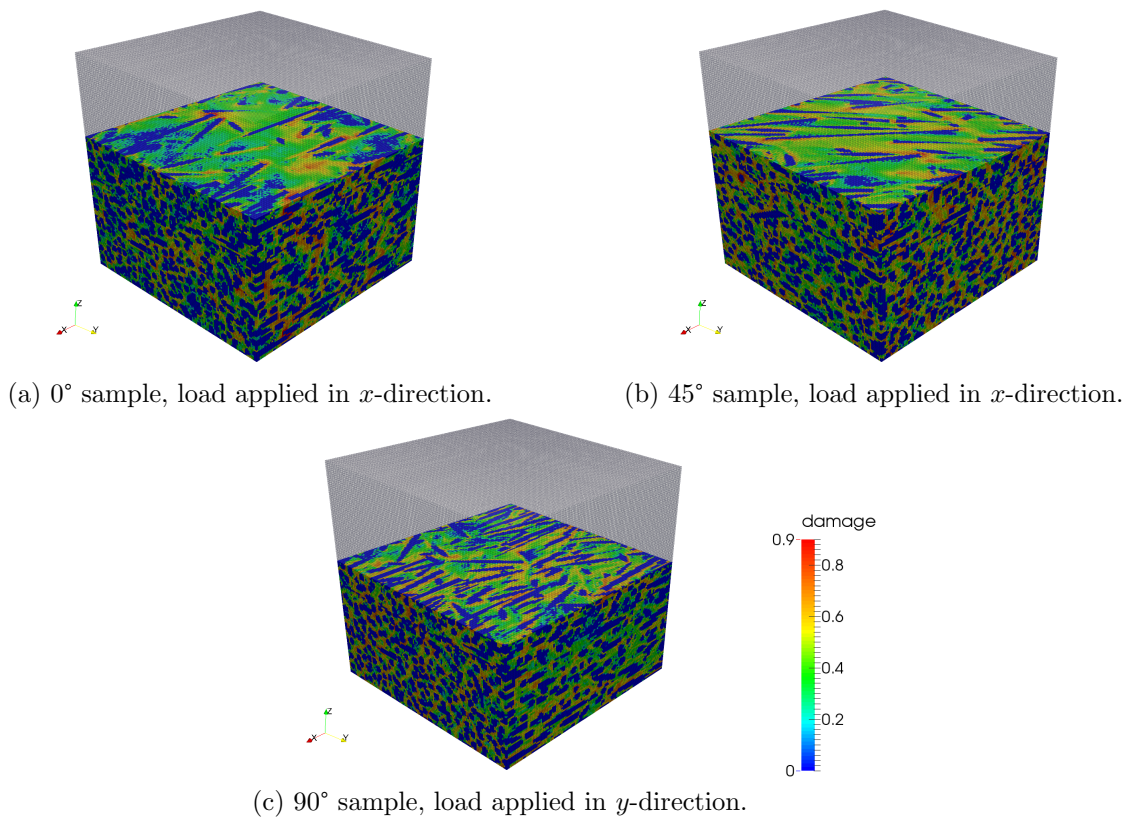


Figure 5.16: Microscopic damage fields in different samples after monotonic loading.

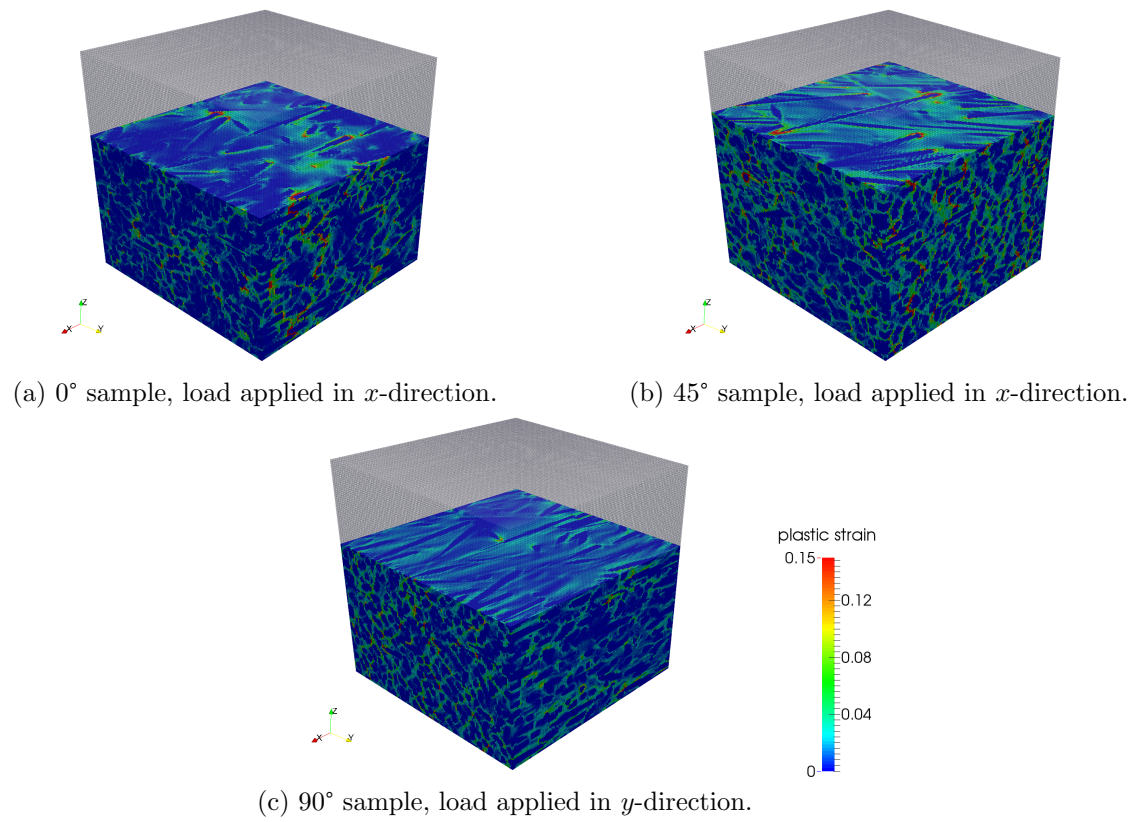


Figure 5.17: Distribution of the equivalent plastic strain in different samples after monotonic loading.

the middle layer are aligned in load direction. Thus, the highly stressed fibers are located there.

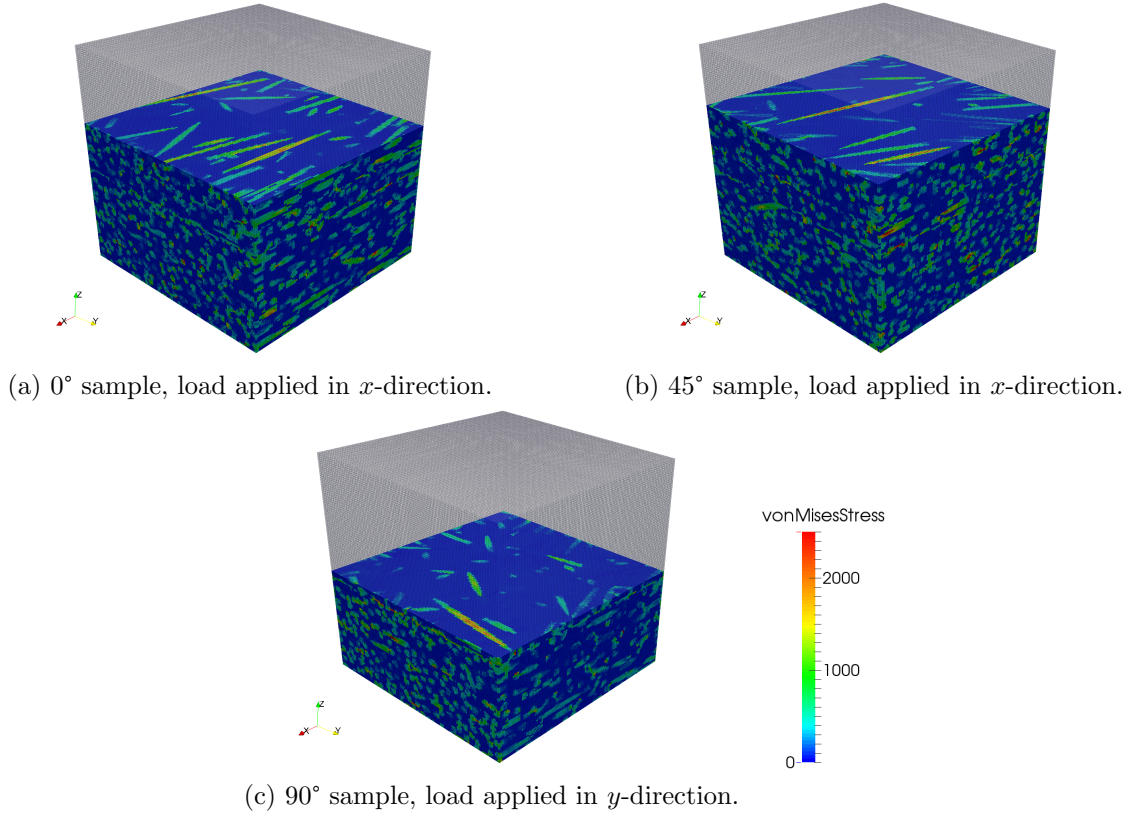


Figure 5.18: Von Mises stress in the fibers after monotonic loading in different samples.

In Figures 5.19 and 5.20 the maximum values of the damage variable and the equivalent plastic strain are shown. Both are located in the surrounding of the sharp fiber edges, in the fiber-matrix interface region.

Composite Material - Cyclic Nonlinear Properties

During a last test the quasi-static loading/unloading behavior of the composite material is simulated. Therefore cyclic tensile tests are performed for the three different loading directions with a strain rate of $\dot{\epsilon} = 10^{-3}/\text{min}$. The experimental and simulated curves are compared to each other. In Figure 5.21 the resulting stress-strain curves are displayed. The simulated curves show a very good agreement with the experimental data. Residual strain and the degraded stiffness are captured very well, especially in the 0° and 45° directions. The enveloping stress-strain curves, particularly the ones of the 0° and 90° samples, present a very similar behavior as the experimental results. Due to the negligence of fiber breakage, the model behavior is always too stiff in the regime of pronounced strains near fracture.

In summary, the results show that it is possible to predict the nonlinear composite behavior based on the validated microstructural model and the related resulting

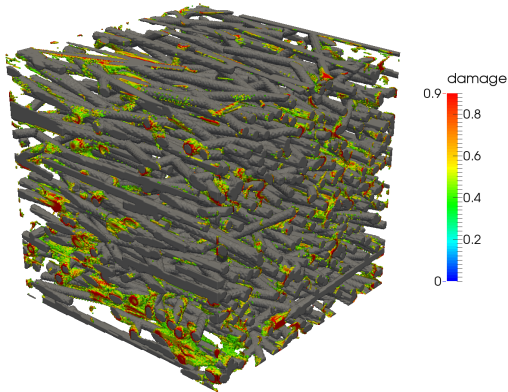


Figure 5.19: Maximum damage values in the 90° sample after monotonic loading.

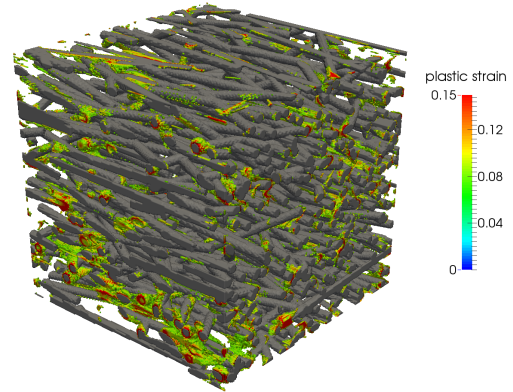


Figure 5.20: Maximum equiv. plastic strain in the 90° sample after monotonic loading.

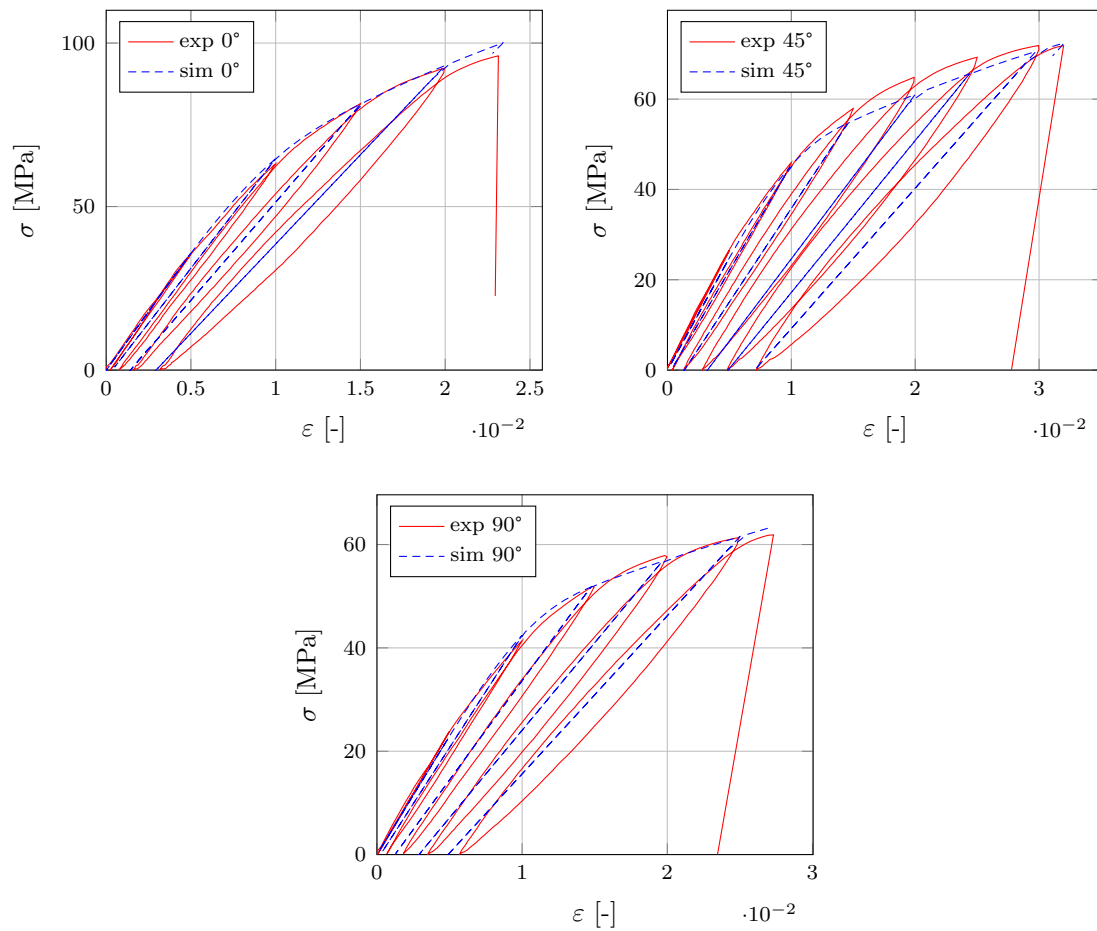


Figure 5.21: Experimental and simulated cyclic stress strain curves for different loading angles φ .

linear elastic effective properties. This is achieved by defining separately suitable material properties for both constituents. Using tabular material parameters for the matrix material obtained from a standard cyclic tensile test, the matrix material behavior can be reproduced easily. Besides the elastic parameters for the glass fibers no further material parameters had been defined. The effective response of the composite follows directly from the material laws of the constituents, and the geometry of the microstructural model. With this effective numerical method even the unloading tests could be reproduced correctly for different micro structures. Reproducing these results would be hardly possible with analytical or semi-analytical homogenization approaches. Especially when non-proportional load paths are taken into consideration, as already indicated in the introductory example of this work.

5.2 Multiscale Computations

5.2.1 Strip with a Hole and Spherical Inclusion

In Figure 5.22 an example for a fully coupled multiscale approach is demonstrated. A strip with a hole modeled with 516 tetrahedral finite elements is coupled to a RVE structure containing a single spherical inclusion and discretized by 20^3 (8000) voxel cells. All macroscopic integration points are fully coupled with the same RVE. The matrix material of the RVE is modeled by the isotropic damage model described in Section 2.3.2 and the behavior of the inclusion is assumed to be linear elastic.

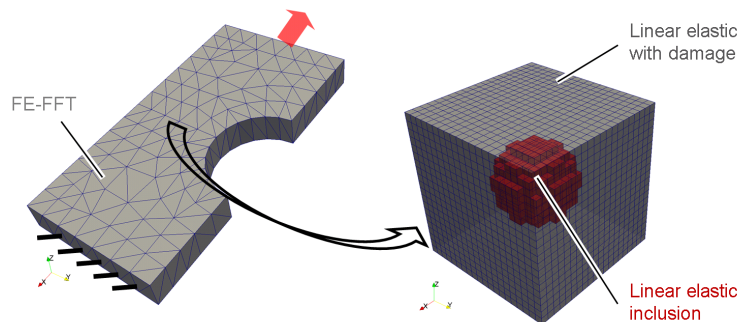


Figure 5.22: Multiscale simulation strip with a hole (macro) and a cubic RVE containing a single spherical inclusion (microscale).

Growing damage on the fine scale with an increasing macroscopic load results in macroscopic reduction of stiffness. Consequently, the macroscopic stress-strain response shows a nonlinear material behavior. The damage distribution of the macroscale and the stress-strain response is illustrated in Figure 5.24.

In Figure 5.25 and 5.26 the convergence behavior of the macroscopic Newton algorithm is illustrated over the load step history. In Figure 5.26 the relative residuum is plotted against the total number of macro Newton iterations. As a second measure of the macroscopic error the norm of the update of the solution relative to the norm of the solution, i.e. $\|\Delta\mathbf{U}\| / \|\mathbf{U}\|$ is shown in Figure 5.25.

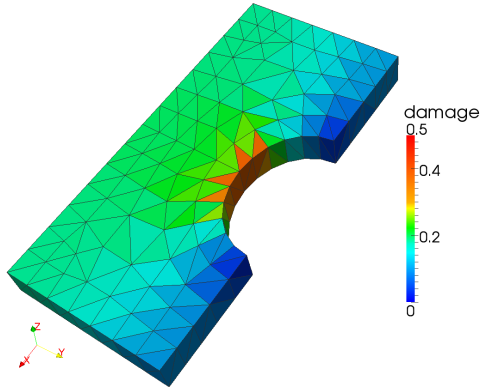


Figure 5.23: Damage distribution of the macroscale.

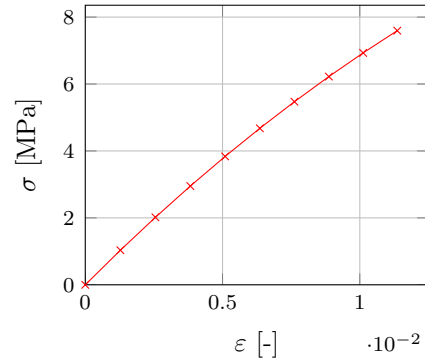


Figure 5.24: Stress-strain response of the macroscale.

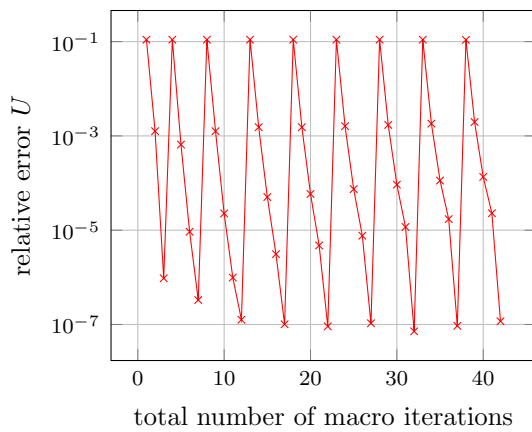


Figure 5.25: Relative error of the solution $\|\Delta U\| / \|U\|$ of the macroscale over the total number of Newton iterations.

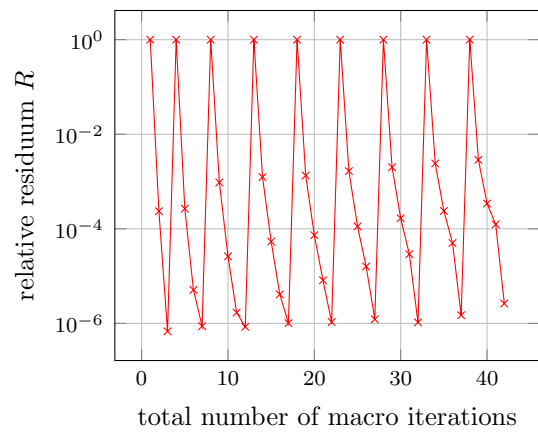


Figure 5.26: Relative residuum R of the macroscale problem over the total number of Newton iterations.

Quadratic convergence is observed for all load steps. The CPU time of the entire problem is around 13 hours on a standard workstation, while a single RVE computation took only a few seconds. For this and the following simulations illustrated in this work, a convergence criterion by means of the relative error of the solution \mathbf{U} of 10^{-6} is chosen.

5.2.2 Strip with a Hole and Fiber Composite

In Figure 5.27 an example for a fully coupled multiscale approach with a more realistic microstructure is demonstrated. The strip with a hole discretized by 516 tetrahedral finite elements is coupled to short fiber reinforced RVE structures which are modeled with 64^3 (262,144) voxel cells. RVEs with 45° fiber orientation with respect to the macro loading direction are associated to the macroscopic integration points. However, for each different macroscopic point any arbitrary RVE structure could be chosen. The polymer matrix of the RVE is modeled with the isotropic damage model and the behavior of the fibers is assumed to be linear elastic.

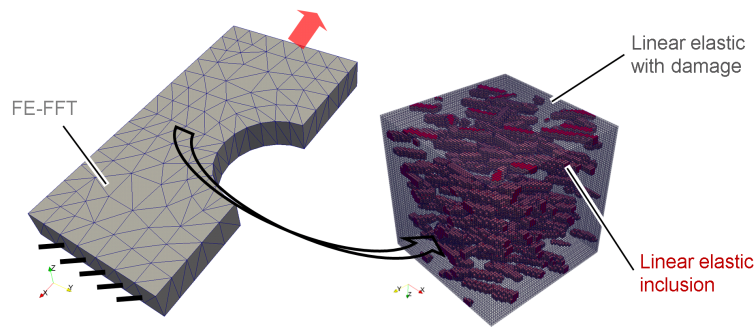


Figure 5.27: Fully coupled micro-macro computation of a strip with a hole (left) and a short fiber reinforced composite structure (right).

An exemplary micro field computed during the multiscale simulation is monitored in Figure 5.29. At the right the relative error of the macroscopic solution field is plotted over the total number of macro iterations. Quadratic convergence can be observed clearly.

During the computation of this example approximately 20,000 unit cell calculations consisting each of 262,144 voxel cells have to be performed. The computational time of the entire problem is around 240 hours on single CPU of a standard workstation. The computation of a single micro problem including the macroscopic load case and six homogenization load cases is distributed over five threads and took on average approximately 40 seconds. The last value strongly depends on the nonlinearity of the micro problem.

In a first attempt the macroscopic problem is parallelized. The self-contained RVE computations are performed sequentially using message passing interface (MPI). The microscopic problems are distributed over five cores and one core is used to control the global process. Thus, the total computational time could be reduced to

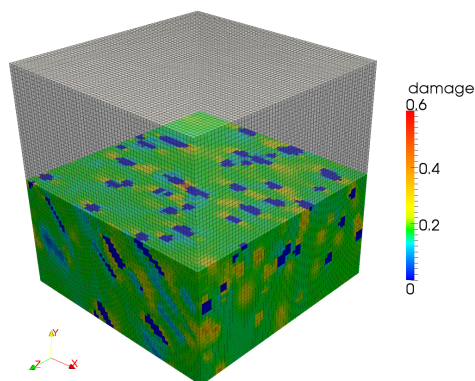


Figure 5.28: Damage distribution of an exemplary micro sample.

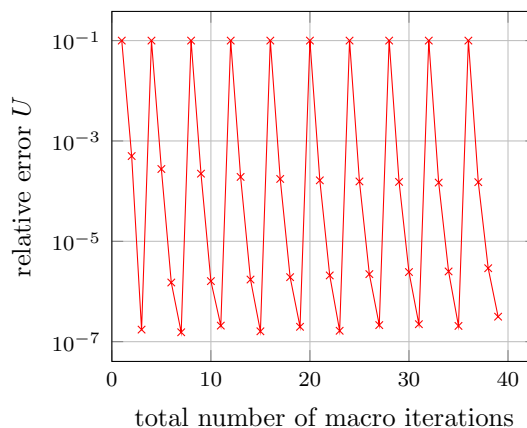


Figure 5.29: Relative error of the solution $\|\Delta \mathbf{U}\| / \|\mathbf{U}\|$ of the macroscale over the total number of Newton iterations.

155 hours. It should be mentioned that the parallelization technique has not been optimized. Each core has to wait until the last process is finished and macroscopic points are computed. A better algorithm would be useful to distribute the micro processes in a more intelligent way. A significant improvement could be achieved if the critical microstructures that are subjected to high macroscopic loads are distributed on different cores and, thus, the most time consuming microstructures are computed sequentially.

5.2.3 L-Profile and Fiber Composite

In the last example a very challenging macrostructural example is demonstrated. An L-shaped structure is discretized with 1650 tetrahedral finite elements of which 93 in the most critical region are coupled to the short fiber reinforced RVE structure already used in the example above, see Figure 5.30. Linear elastic material behavior is assigned to the remaining area of the macroscopic structure. The polymer matrix of the RVE is modeled by the isotropic damage model and the behavior of the fibers is assumed to be linear elastic.

The damage distribution of the L-profile computed during the multiscale simulation is illustrated in Figure 5.32. At the right the relative error of the macroscopic solution field is plotted over the total number of macro iterations. The simulation is stopped when the relative error of the macro solution \mathbf{U} falls below a value of 10^{-6} . The simulation is aborted at the fifth load step due to convergence problems, because the microscale started to localize at this point. The CPU time amounts to approximately 17 hours on standard workstation.

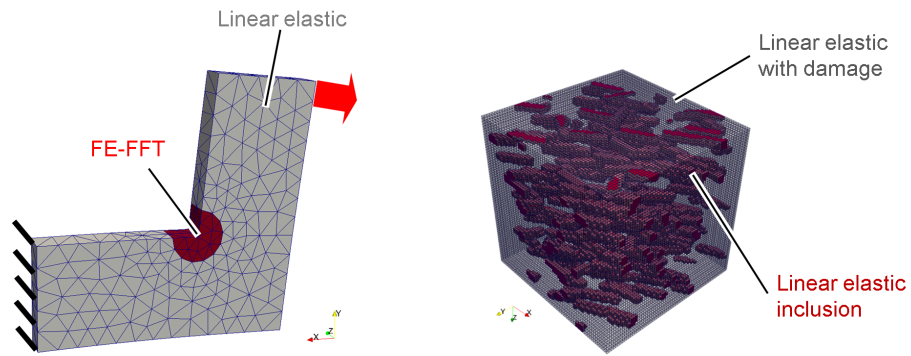


Figure 5.30: Coupled micro-macro computation of an L-profile (left) and a short fiber reinforced composite structure (right). The constitutive equation of the macroscale is replaced in the most critical regions by a multiscale approach.

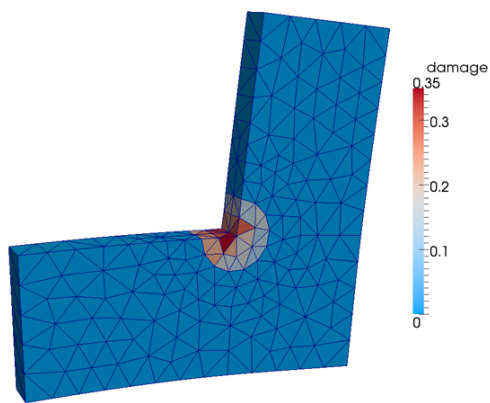


Figure 5.31: Macroscopic damage field in the vertex of the L-profile.

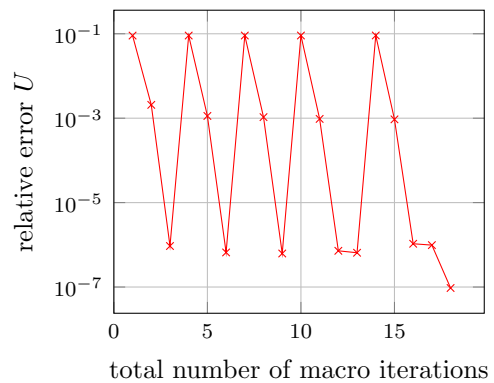


Figure 5.32: Relative error of the solution $\|\Delta U\| / \|U\|$ of the macroscale over the total number of Newton iterations.

Remark: The examples shown in this work were considered until material softening appeared. This means the simulations were stopped when localization on the material scale occurred, so that the governing equation keeps its ellipticity and the assumption of separation of scales remains valid. In the opinion of the authors this should be satisfactory in this case, due to the brittle fracture characteristics of the considered fiber reinforced composite materials.

Chapter 6

Conclusion and Outlook

6.1 Conclusion and Main Results

The main results achieved in this work can be divided in two parts. The first part covers the computations of nonlinear composite materials at the microscale level, with a particular focus on progressive damage of short fiber reinforced polymers. This includes the physical and geometrical modeling of heterogeneous microstructures, the homogenization technique in order to form effective quantities of the microstructural models, and the numerical framework for solving the related differential equations. The second part addresses the efficient multiscale approach established in this work.

With regard to the first part, suitable constitutive laws for the microscopic constituents have been defined, see Chapter 2. For modeling brittle damage, as it occurs for instance in reinforced concrete or resin matrix composite materials, the reinforcements are assumed to be linear elastic and the matrix material is modeled by an elastic isotropic damage law. In order to predict ductile damage of thermoplastic polymer materials it is shown that a constitutive law describing the interaction between the physical effects of damage and plastic deformation is necessary. Some general differences in the thermodynamic framework of elastoplastic damage models are discussed. The main differences are the state law which is derived from a free energy, the form of the elastic limit criterion, and the coupling and evolution of internal variables. In experimental data of thermoplastic polymers a damage saturation effect over the plastic strain is observed. It has been recognized that many common models could not reproduce the material behavior. The model of Ju [1989] treats the evolution of plasticity and damage effects in a separate way which enables one to model the interaction specifically. Furthermore, the separate treatment reduces the complexity of the numerical system. Besides the definition of the physical behavior of the particular material phases, a geometrical model is generated that represents the materials microstructure. Representative volume elements (RVE) are generated using information of fiber diameter, solid volume fraction and orientation of measured data. Size and resolution of the RVEs are tested and validated with experimental data. Periodic boundary conditions are proven to be the most accurate for computing effective properties and have been chosen to incorporate the boundary conditions in the numerical simulation. Effective homogenized quantities are calculated as volume averages over the entire unit cell and the homogenized stiffness is obtained using Hill's energy criterion.

An efficient numerical framework is used to solve the periodic micromechanical problems, see Chapter 3. The governing differential equation that describes the static equilibrium at the microscopic level is reformulated into an integral equation of Lippmann-Schwinger type and the overall material response of composite materials is computed by an efficient numerical algorithm based on fast Fourier transforms. Besides its benefits in terms of memory consumption and computational time, the method does not require the assembly and storage of a global stiffness matrix. Thus, larger and more realistic microstructures can be computed efficiently. Furthermore, the unit cell computations are carried out on regular voxel grids. Therefore, the method can be applied directly to compute homogenized quantities on three dimensional images like tomographies without using any complicated mesh generation. A detailed description for the entire algorithm of the numerical method is given. Several authors proposed extended algorithms dealing with nonlinear material behavior, in order to improve the convergence behavior. In this work, fixed point iteration is applied to solve the nonlinear equations directly, as proposed in the original algorithm of Moulinec and Suquet [1998]. In terms of accuracy and numerical robustness, it turned out to be the best way to deal with the issues related to this work. The convergence of the method is examined on a unit cell computation, which contains a spherical inclusion.

The mechanisms of growing damage which can be observed in short fiber reinforced composites are shown in Chapter 5.1. Microscans of failed structures compared with simulated results show that within the numerical simulation the micromechanical damage mechanisms are captured. Furthermore, the microstructural model has been validated with experimental data of a short fiber reinforced thermoplastic material. In order to reproduce the matrix material behavior the coupled constitutive law of Ju [1989] has been modified using linear interpolation of the measured tabular values obtained from standard cyclic tensile tests. For simulating the effective composite response, a microstructural model is generated with geometrical data obtained from micrograph analysis. Standard values for the elastic parameters of the glass fibers have been chosen and size and resolution of the RVE have been validated with measured anisotropic stiffness properties. Comparison with experimental results show that the effective linear and nonlinear response of the composite is predicted precisely. It follows directly from the material laws of the constituents, and the geometry of the microstructural model. Using this efficient numerical homogenization approach, also unloading tests in different loading directions are reproduced correctly. Reproducing these results would be hardly possible with analytical or semi-analytical homogenization approaches, especially when non proportional load paths are taken into consideration.

In regard to the second part of this conclusion an efficient multiscale approach has been established. The macroscopic behavior of nonlinear composite materials is investigated in Chapter 4. The numerical methods which are used to solve the boundary value problems related to the spatial scales considered in this work are coupled by

a procedure similar to the FE^2 approach proposed by Feyel and Chaboche [2000] and Smit et al. [1998]. The constitutive equation at the coarse scale is replaced by an associated boundary value problem at the microscopic level and progressive damage is transported between the scales. Due to the increased computational costs involved with the application of a fully coupled multiscale framework, the efficient microscopic homogenization method is used to compute the micro BVP. The macroscopic scale is solved by the finite element method. Hence, arbitrary shaped macroscopic components can be treated in a standard manner. The multiscale approach enables to capture nonlinear material effects caused by microscopic physical effects directly on a finer length scale. Hence, within this method, the exact physical response under different loading conditions is obtained for arbitrary microstructures. Moreover, simple (isotropic) constitutive laws can be used to define the material behavior of the microstructural constituents and the required parameters can be measured directly in physical experiments. Besides the isotropic damage model used in this work basically any arbitrary (anisotropic) material model can be implemented.

The scale coupling technique and the computation of the macroscopic tangent by numerical perturbation is shown. Details about the algorithmic implementation and the storage and evolution of internal variables are assessed. In a numerical example, the size of the perturbation strain and its influence on the convergence behavior of the macroscopic Newton algorithm is investigated. Furthermore, the onset of macroscopic failure is studied in a numerical analysis of the acoustic tensor of the current homogenized tangent stiffness tensor. Within the established procedure failure of microstructures can be detected efficiently. Finally, some multiscale examples of realistic structures are shown in Chapter 5.2. Growing damage among the material constituents at the micro scale results in a macroscopic reduction of stiffness and a redistribution of macroscopic stresses. The convergence behavior of the macroscopic Newton algorithm and the computational times are investigated. Quadratic convergence for all load steps is observed. In order to reduce the computational time the macroscopic problem is parallelized. The self-contained RVE computations are performed simultaneously using message passing interface (MPI).

6.2 Outlook and Future Work

In summary, the established multiscale method presents an accurate and efficient tool for computing the effective nonlinear response of composite materials. The microscale problem can easily be implemented in commercial software codes. In Sliseris et al. [2014a,b] the microscopic problem has been implemented in the implicit FEM code Abaqus by using a user defined material subroutine. Scripting interfaces can be used to manage the micro computations, in order to read and write input and output parameters from files and to execute computations. The decoupled microscopic problems can be solved simultaneously. With increasing computational power the method will become more and more interesting for future industrial applications.

The microscopic computational homogenization framework can be used as a kind of virtual material laboratory for computing effective material quantities of varying microstructures and loading situations. In this regard, the computation of failure or plastic yield surfaces for particular microstructures represents a highly interesting application. The point of failure of some selected micro structures is precomputed for a certain amount of loading situations. The onset of macroscopic failure can be detected using the acoustic tensor of the computed homogenized stiffness matrix. Technical details concerning the determination of effective plastic yield and failure surfaces of composite materials using the finite element method are presented in the works of Hoffmann [2012] and Schmidt [2011]. Furthermore, with the micromechanical approach, conventional macroscopic failure criteria can be parameterized. The material parameters are identified by precomputing selected loading situations on representative volume elements. The macroscopic criteria can be applied for failure investigations at the macroscopic scale, when simple proportional macroscopic loading situations and uniform microstructures over the macroscopic domain are expected. Otherwise, the parameters for the failure criteria have to be precomputed for each microstructure and each macroscopic loading situation again. Precomputed failure surfaces or conventional failure criteria can be used in order to obtain a first estimation of the onset of macroscopic failure. For a more precise prediction of the macromechanical material behavior including progressive damage, a coupled simulation has to be performed. In particular, a coupled simulation becomes essential when complex macroscopic loading situations and even unloading occurs.

Despite the use of an efficient algorithm for solving the microscopic problem, the high computational time of the multiscale approach represents still the main shortcoming of the coupled method. In future work, the efficiency of the multiscale approach can be increased by parallel computing and hence, growing computational resources can be used more efficiently. Nevertheless, due to the expensive coupled simulation, the quantity of microscopic computations should be minimized. The number can be reduced by interpolating database values obtained from previous computed similar macroscopic loading situations. A new microscopic simulation is only performed if the macroscopic load changes significantly in a particular macroscopic

point. Furthermore, coupled full-field simulations should only be accomplished in critical macroscopic points. Homogenization techniques can be combined, and at less critical points, coupled analytical or semi-analytical interpolation methods can be used. Critical macroscopic points can be identified for instance, using configurational forces [Kuhn, 2013, Müller et al., 2002] or principal stress criteria [Linder and Zhang, 2013].

Furthermore, the proposed multiscale method can be extended to deal with the propagation of macroscopic cracks. The method can be used to analyze the nucleation of macroscopic cracks by detecting failure in microstructures at specific macroscopic points. In order to be able to transport evolving cracks between the scales, special coupling techniques are necessary. Cracks, considered as discontinuities in the displacement field, can be incorporated in the macroscale simulation by the extended finite element method [Belytschko et al., 2008, Holl et al., 2013] or the embedded strong discontinuity approach [Linder and Raina, 2013].

Bibliography

- Aboudi, J., 1989. Micromechanical analysis of composites by the method of cells. *Applied Mechanics Reviews* 42, 193.
- Aboudi, J., 1996. Micromechanical analysis of composites by the method of cells-update. *Applied Mechanics Reviews* 49, 83.
- Abu Al-Rub, R. K., Voyiadjis, G. Z., 2003. On the coupling of anisotropic damage and plasticity models for ductile materials. *International Journal of Solids and Structures* 40 (11), 2611–2643.
- Armero, F., Garikipati, K., 1996. An analysis of strong discontinuities in multiplicative finite strain plasticity and their relation with the numerical simulation of strain localization in solids. *International Journal of Solids and Structures* 33 (20), 2863–2885.
- Axelsson, O., Barker, V. A., 1984. Finite element solution of boundary value problems: theory and computation. Vol. 35. Siam.
- Bakhvalov, N., Panasenko, G. P., 1989. Homogenisation: averaging processes in periodic media: mathematical problems in the mechanics of composite materials. Kluwer Academic Publishers.
- Balzani, D., Brands, D., Schröder, J., 2014. Construction of statistically similar representative volume elements. In: *Plasticity and Beyond*. Springer, pp. 355–412.
- Baur, E., Osswald, T. A., Rudolph, N., 2013. *Saechtling Kunststoff Taschenbuch*. Hanser Verlag.
- Bayreuther, C., 2005. Mehrskalenmodelle in der Festkörpermechanik und Kopplung von Mehrgittermethoden mit Homogenisierungsverfahren. Ph.D. thesis, Universität Stuttgart.
- Belytschko, T., Fish, J., Bayliss, A., 1990. The spectral overlay on finite elements for problems with high gradients. *Computer Methods in Applied Mechanics and Engineering* 81 (1), 71–89.
- Belytschko, T., Liu, W. K., Moran, B., Elkhodary, K., 2013. *Nonlinear finite elements for continua and structures*. John Wiley & Sons.
- Belytschko, T., Loehnert, S., Song, J.-H., 2008. Multiscale aggregating discontinuities: a method for circumventing loss of material stability. *International Journal for Numerical Methods in Engineering* 73 (6), 869–894.
- Bensoussan, A., Lions, J.-L., Papanicolaou, G., 2011. *Asymptotic analysis for periodic structures*. Vol. 374. American Mathematical Society.

- Bensoussan, A., Lions, J.-L., Papanicolau, G., 1978. Asymptotic analysis for periodic structures. North-Holland, Amsterdam.
- Benveniste, Y., 1987. A new approach to the application of mori-tanaka's theory in composite materials. *Mechanics of Materials* 6 (2), 147–157.
- Besson, J., Cailletaud, G., Chaboche, J.-L., Forest, S., 2010. Non-linear mechanics of materials. Vol. 167. Springer.
- Bilger, N., Auslender, F., Bornert, M., Moulinec, H., Zaoui, A., 2007. Bounds and estimates for the effective yield surface of porous media with a uniform or a nonuniform distribution of voids. *European Journal of Mechanics-A/Solids* 26 (5), 810–836.
- Böhlke, T., 2001. Crystallographic Texture Evolution and Elastic Anisotropy: Simulation, Modeling, and Applications. *Berichte aus der Mechanik*. Shaker.
- Böhlke, T., Brüggemann, C., 2001. Graphical representation of the generalized hooke's law. *Technische Mechanik* 21 (2), 145–158.
- Bonet, J., Wood, R., 2008. *Nonlinear Continuum Mechanics for Finite Element Analysis*. Cambridge University Press.
- Bonora, N., 1997. A nonlinear CDM model for ductile failure. *Engineering Fracture Mechanics* 58 (1), 11–28.
- Brisard, S., 2011. Analyse morphologique et homogénéisation numérique: application à la pâte de ciment. Ph.D. thesis, Université Paris-Est.
- Brisard, S., Dormieux, L., 2010. FFT-based methods for the mechanics of composites: A general variational framework. *Computational Materials Science* 49 (3), 663–671.
- Brisard, S., Dormieux, L., 2012. Combining galerkin approximation techniques with the principle of hashin and shtrikman to derive a new FFT-based numerical method for the homogenization of composites. *Computer Methods in Applied Mechanics and Engineering* 217, 197–212.
- Budiansky, B., 1965. On the elastic moduli of some heterogeneous materials. *Journal of the Mechanics and Physics of Solids* 13 (4), 223–227.
- Celentano, D. J., Chaboche, J.-L., 2007. Experimental and numerical characterization of damage evolution in steels. *International Journal of Plasticity* 23 (10), 1739–1762.
- Chaboche, J., 1977. Sur l'utilisation des variables d'état interne pour la description de la viscoplasticité cyclique avec endommagement. In: *Problemes non linéaires de mécanique*, Symposium Franco-Polonais de rhéologie et mécanique. pp. 137–159.

-
- Chaboche, J., 1988. Continuum damage mechanics. *Journal of Applied Mechanics* 55 (1), 59–64.
- Chaboche, J., 1996. Unified cyclic viscoplastic constitutive equations: development, capabilities, and thermodynamic framework. In: *Unified Constitutive Laws of Plastic Deformation*. Academic Press, pp. 1–68.
- Chaboche, J., Kruch, S., Maire, J., Pottier, T., 2001. Towards a micromechanics based inelastic and damage modeling of composites. *International Journal of Plasticity* 17 (4), 411–439.
- Chaboche, J.-L., 1979. The concept of effective strain applied to elasticity and viscoelasticity in the presence of anisotropic damage. In: *Colloque International sur le Comportement Mécanique des Solides Anisotropes*. No. 1979-77.
- Chow, C., Wang, J., 1987. An anisotropic theory of continuum damage mechanics for ductile fracture. *Engineering Fracture Mechanics* 27 (5), 547–558.
- Christensen, R., Lo, K., 1979. Solutions for effective shear properties in three phase sphere and cylinder models. *Journal of the Mechanics and Physics of Solids* 27 (4), 315–330.
- Christensen, R. M., 1990. A critical evaluation for a class of micro-mechanics models. *Journal of the Mechanics and Physics of Solids* 38 (3), 379–404.
- Christensen, R. M., 2012. *Mechanics of composite materials*. Dover Publications.
- Coenen, E., Kouznetsova, V., Geers, M., 2012. Multi-scale continuous-discontinuous framework for computational-homogenization-localization. *Journal of the Mechanics and Physics of Solids*.
- Cordebois, J., Sidoroff, F., 1982. Damage induced elastic anisotropy. In: *Comportement Mécanique des Solides Anisotropes*. Springer, pp. 761–774.
- Cuntze, R., 2006. Efficient 3D and 2D failure conditions for UD laminae and their application within the verification of the laminate design. *Composites Science and Technology* 66 (7), 1081–1096.
- de Borst, R., Sluys, L., Muhlhaus, H.-B., Pamin, J., 1993. Fundamental issues in finite element analyses of localization of deformation. *Engineering Computations* 10 (2), 99–121.
- de Souza Neto, E., 2002. A fast, one-equation integration algorithm for the lemaître ductile damage model. *Communications in Numerical Methods in Engineering* 18 (8), 541–554.
- de Souza Neto, E. A., Peric, D., Owen, D. R. J., 2011. *Computational methods for plasticity: theory and applications*. Wiley & Sons.

- Dederichs, P., Zeller, R., 1973. Variational treatment of the elastic constants of disordered materials. *Zeitschrift für Physik* 259 (2), 103–116.
- Dennis, J. E., Schnabel, R. B., 1987. Numerical methods for unconstrained optimization and nonlinear equations. Vol. 16. Society for Industrial and Applied Mathematics.
- Detrez, F., Cantournet, S., Seguela, R., 2011. Plasticity/damage coupling in semi-crystalline polymers prior to yielding: Micromechanisms and damage law identification. *Polymer* 52 (9), 1998–2008.
- Döbert, C., 2001. Meso-makromechanische modellierung von faserverbundwerkstoffen mit schädigung. Ph.D. thesis, Universität Hannover.
- Drugan, W., Willis, J., 1996. A micromechanics-based nonlocal constitutive equation and estimates of representative volume element size for elastic composites. *Journal of the Mechanics and Physics of Solids* 44 (4), 497–524.
- Dvorak, G., 1992. Transformation field analysis of inelastic composite materials. *Proceedings of the Royal Society of London. Series A: Mathematical and Physical Sciences* 437 (1900), 311–327.
- Eisenlohr, P., Diehl, M., Lebensohn, R., Roters, F., 2013. A spectral method solution to crystal elasto-viscoplasticity at finite strains. *International Journal of Plasticity* 46, 37–53.
- Eshelby, J., 1957. The determination of the elastic field of an ellipsoidal inclusion, and related problems. *Proceedings of the Royal Society of London. Series A. Mathematical and Physical Sciences* 241 (1226), 376–396.
- Eyre, D., Milton, G., 1999. A fast numerical scheme for computing the response of composites using grid refinement. *EPJ Applied Physics* 6, 41–48.
- Farhat, C., Lesoinne, M., Pierson, K., 2000. A scalable dual-primal domain decomposition method. *Numerical Linear Algebra with Applications* 7 (7-8), 687–714.
- FeelMath, 2014. Finite elements for elastic materials and homogenization.
URL <http://www.itwm.fraunhofer.de/en/departments/flow-and-material-simulation/mechanics-of-materials/feelmath/>
- Feyel, F., Chaboche, J., 2000. FE² multiscale approach for modelling the elastoviscoplastic behaviour of long fibre SiC/Ti composite materials. *Computer Methods in Applied Mechanics and Engineering* 183 (3), 309–330.
- FFTW, 2014. Fastest fourier transform in the west.
URL <http://www.fftw.org/>

-
- Fish, J., Shek, K., Pandheeradi, M., Shephard, M., 1997. Computational plasticity for composite structures based on mathematical homogenization: Theory and practice. *Computer Methods in Applied Mechanics and Engineering* 148 (1), 53–73.
- Fish, J., Yu, Q., Shek, K., 1999. Computational damage mechanics for composite materials based on mathematical homogenization. *International Journal for Numerical Methods in Engineering* 45 (11), 1657–1679.
- Fritzen, F., Boehlke, T., 2013. Reduced basis homogenization of viscoelastic composites. *Composites Science and Technology* 76, 84–91.
- Fritzen, F., Böhlke, T., 2010. Three-dimensional finite element implementation of the nonuniform transformation field analysis. *International Journal for Numerical Methods in Engineering* 84 (7), 803–829.
- Geers, M., Kouznetsova, V., Brekelmans, W., 2010. Multi-scale computational homogenization: Trends and challenges. *Journal of Computational and Applied Mathematics* 234 (7), 2175–2182.
- Geodict, 2014. The virtual material laboratory.
URL <http://www.geodict.de/>
- Ghosh, S., Lee, K., Moorthy, S., 1995. Multiple scale analysis of heterogeneous elastic structures using homogenization theory and voronoi cell finite element method. *International Journal of Solids and Structures* 32 (1), 27–62.
- Ghosh, S., Lee, K., Moorthy, S., 1996. Two scale analysis of heterogeneous elastic-plastic materials with asymptotic homogenization and voronoi cell finite element model. *Computer Methods in Applied Mechanics and Engineering* 132 (1), 63–116.
- Gitman, I., Askes, H., Sluys, L., 2007. Representative volume: existence and size determination. *Engineering Fracture Mechanics* 74 (16), 2518–2534.
- Gross, D., Seelig, T., 2011. *Fracture mechanics: with an introduction to micromechanics*. Springer.
- Gruttmann, F., Wagner, W., 2013. A coupled two-scale shell model with applications to layered structures. *International Journal for Numerical Methods in Engineering*.
- Guedes, J., Kikuchi, N., 1990. Preprocessing and postprocessing for materials based on the homogenization method with adaptive finite element methods. *Computer Methods in Applied Mechanics and Engineering* 83 (2), 143–198.
- Guidault, P.-A., Allix, O., Champaney, L., Cornuault, C., 2008. A multiscale extended finite element method for crack propagation. *Computer Methods in Applied Mechanics and Engineering* 197 (5), 381–399.

- Gurson, A. L., 1977. Continuum theory of ductile rupture by void nucleation and growth: Part I—yield criteria and flow rules for porous ductile media. *Journal of Engineering Materials and Technology* 99 (1), 2–15.
- Gusev, A. A., 1997. Representative volume element size for elastic composites: a numerical study. *Journal of the Mechanics and Physics of Solids* 45 (9), 1449–1459.
- Han, D., Dai, H., Qi, L., 2009. Conditions for strong ellipticity of anisotropic elastic materials. *Journal of Elasticity* 97 (1), 1–13.
- Hansen, N., Schreyer, H., 1994. A thermodynamically consistent framework for theories of elastoplasticity coupled with damage. *International Journal of Solids and Structures* 31 (3), 359–389.
- Hashin, Z., 1962. The elastic moduli of heterogeneous materials. *Journal of Applied Mechanics* 29 (1), 143–150.
- Hashin, Z., 1983. Analysis of composite materials. *Journal of Applied Mechanics* 50 (2), 481–505.
- Hashin, Z., Shtrikman, S., 1963. A variational approach to the theory of the elastic behaviour of multiphase materials. *Journal of the Mechanics and Physics of Solids* 11 (2), 127–140.
- Hazanov, S., Huet, C., 1994. Order relationships for boundary conditions effect in heterogeneous bodies smaller than the representative volume. *Journal of the Mechanics and Physics of Solids* 42 (12), 1995–2011.
- Hesebeck, O., 2000. Zur modellierung von schaedigungsprozessen in elastoplastischen materialien. Ph.D. thesis, Universität Karlsruhe.
- Hesebeck, O., 2001. On an isotropic damage mechanics model for ductile materials. *International Journal of Damage Mechanics* 10 (4), 325–346.
- Hill, R., 1962. Acceleration waves in solids. *Journal of the Mechanics and Physics of Solids* 10 (1), 1–16.
- Hill, R., 1963. Elastic properties of reinforced solids: some theoretical principles. *Journal of the Mechanics and Physics of Solids* 11 (5), 357–372.
- Hill, R., 1965. A self-consistent mechanics of composite materials. *Journal of the Mechanics and Physics of Solids* 13 (4), 213–222.
- Hill, R., 1972. On constitutive macro-variables for heterogeneous solids at finite strain. *Proceedings of the Royal Society of London. A. Mathematical and Physical Sciences* 326 (1565), 131–147.
- Hill, R., 1998. *The mathematical theory of plasticity*. Vol. 11. Oxford university press.

-
- Hoffmann, S., 2012. Computational homogenization of short fiber reinforced thermoplastic materials. Ph.D. thesis, Technische Universität Kaiserslautern.
- Holl, M., Loehnert, S., Wriggers, P., 2013. An adaptive multiscale method for crack propagation and crack coalescence. *International Journal for Numerical Methods in Engineering* 93 (1), 23–51.
- Holzappel, G. A., 2000. *Nonlinear solid mechanics: a continuum approach for engineering*. John Wiley & Sons.
- Horst, J., Salienko, N., Spoormaker, J., 1998. Fibre-matrix debonding stress analysis for short fibre-reinforced materials with matrix plasticity, finite element modelling and experimental verification. *Composites Part A: Applied Science and Manufacturing* 29 (5), 525–531.
- Horst, J., Spoormaker, J., 1996. Mechanisms of fatigue in short glass fiber reinforced polyamide 6. *Polymer Engineering & Science* 36 (22), 2718–2726.
- Horst, J., Spoormaker, J., 1997. Fatigue fracture mechanisms and fractography of short-glassfibre-reinforced polyamide 6. *Journal of materials science* 32 (14), 3641–3651.
- Hughes, T. J., 2012. *The finite element method: linear static and dynamic finite element analysis*. Dover Publications.
- Ibrahimbegović, A., Marković, D., 2003. Strong coupling methods in multi-phase and multi-scale modeling of inelastic behavior of heterogeneous structures. *Computer Methods in Applied Mechanics and Engineering* 192 (28), 3089–3107.
- Idiart, M., Moulinec, H., Ponte Castaneda, P., Suquet, P., 2006. Macroscopic behavior and field fluctuations in viscoplastic composites: Second-order estimates versus full-field simulations. *Journal of the Mechanics and Physics of Solids* 54 (5), 1029–1063.
- Ju, J., 1989. On energy-based coupled elastoplastic damage theories: constitutive modeling and computational aspects. *International Journal of Solids and Structures* 25 (7), 803–833.
- Kabel, M., Andrä, H., 2012. Numerical bounds of effective elastic moduli. *Berichte des Fraunhofer ITWM* 224 (1), 1–13.
- Kabel, M., Böhlke, T., Schneider, M., 2014. Efficient fixed point and newton–krylov solvers for FFT-based homogenization of elasticity at large deformations. *Computational Mechanics* 54 (6), 1497–1514.
- Kachanov, L., 1958. Time of the rupture process under creep conditions. *Isv. Akad. Nauk. SSR. Otd Tekh. Nauk* 8, 26–31.
- Kachanov, L., 1986. *Introduction to continuum damage mechanics*. Vol. 10. Springer.

- Kanit, T., Forest, S., Galliet, I., Mounoury, V., Jeulin, D., 2003. Determination of the size of the representative volume element for random composites: statistical and numerical approach. *International Journal of Solids and Structures* 40 (13), 3647–3679.
- Kanouté, P., Boso, D., Chaboche, J., Schrefler, B., 2009. Multiscale methods for composites: a review. *Archives of Computational Methods in Engineering* 16 (1), 31–75.
- Klusemann, B., Böhm, H., Svendsen, B., 2012. Homogenization methods for multi-phase elastic composites with non-elliptical reinforcements: Comparisons and benchmarks. *European Journal of Mechanics-A/Solids* 34, 21–37.
- Kouznetsova, V., 2002. Computational homogenization for the multi-scale analysis of multi-phase materials. Ph.D. thesis, Technische Universiteit Eindhoven.
- Kouznetsova, V., Brekelmans, W., Baaijens, F., 2001. An approach to micro-macro modeling of heterogeneous materials. *Computational Mechanics* 27 (1), 37–48.
- Kouznetsova, V., Geers, M., Brekelmans, W., 2004. Multi-scale second-order computational homogenization of multi-phase materials: a nested finite element solution strategy. *Computer Methods in Applied Mechanics and Engineering* 193 (48), 5525–5550.
- Kouznetsova, V., Geers, M. G., Brekelmans, W. M., 2002. Multi-scale constitutive modelling of heterogeneous materials with a gradient-enhanced computational homogenization scheme. *International Journal for Numerical Methods in Engineering* 54 (8), 1235–1260.
- Krajcinovic, D., 1985. Continuous damage mechanics revisited: basic concepts and definitions. *Journal of Applied Mechanics* 52 (4), 829–834.
- Krajcinovic, D., 1989. Damage mechanics. *Mechanics of Materials* 8 (2), 117–197.
- Krajcinovic, D., 1996. Damage mechanics. Vol. 41. Elsevier.
- Kröner, E., 1958. Berechnung der elastischen konstanten des vielkristalls aus den konstanten des einkristalls. *Zeitschrift für Physik A Hadrons and Nuclei* 151 (4), 504–518.
- Kröner, E., 1977. Bounds for effective elastic moduli of disordered materials. *Journal of the Mechanics and Physics of Solids* 25 (2), 137–155.
- Kröner, E., 1990. Modified green functions in the theory of heterogeneous and/or anisotropic linearly elastic media. In: *Micromechanics and inhomogeneity*. Springer, pp. 197–211.
- Kuhl, E., 2000. Numerische modelle für kohäsive reibungsmaterialien. Ph.D. thesis, Universität Stuttgart.

-
- Kuhn, C., 2013. Numerical and analytical investigation of a phase field model for fracture. Ph.D. thesis, Technische Universität Kaiserslautern.
- Lahellec, N., Michel, J., Moulinec, H., Suquet, P., et al., 2003. Analysis of inhomogeneous materials at large strains using fast fourier transforms. *Solid Mechanics and Its Applications* 108, 247–258.
- Largenton, R., Michel, J.-C., Suquet, P., 2014. Extension of the nonuniform transformation field analysis to linear viscoelastic composites in the presence of aging and swelling. *Mechanics of Materials* 73, 76–100.
- Lebensohn, R. A., Kanjarla, A. K., Eisenlohr, P., 2012. An elasto-viscoplastic formulation based on fast fourier transforms for the prediction of micromechanical fields in polycrystalline materials. *International Journal of Plasticity* 32, 59–69.
- Lemaitre, J., 1984. How to use damage mechanics. *Nuclear Engineering and Design* 80 (2), 233–245.
- Lemaitre, J., 1985a. A continuous damage mechanics model for ductile fracture. *Journal of Engineering Materials and Technology* 107, 83.
- Lemaitre, J., 1985b. Coupled elasto-plasticity and damage constitutive equations. *Computer Methods in Applied Mechanics and Engineering* 51 (1), 31–49.
- Lemaitre, J., Desmorat, R., 2005. *Engineering damage mechanics: ductile, creep, fatigue and brittle failures*. Springer.
- Lemaitre, J., Lippmann, H., 1996. *A course on damage mechanics*. Vol. 2. Springer.
- Li, J., Meng, S., Tian, X., Song, F., Jiang, C., 2012. A non-local fracture model for composite laminates and numerical simulations by using the FFT method. *Composites Part B: Engineering* 43 (3), 961–971.
- Lielens, G., 1999. *Micro-macro modeling of structured materials*. Ph.D. thesis, Université Catholique de Louvain.
- Linder, C., Armero, F., 2007. Finite elements with embedded strong discontinuities for the modeling of failure in solids. *International Journal for Numerical Methods in Engineering* 72 (12), 1391–1433.
- Linder, C., Raina, A., 2013. A strong discontinuity approach on multiple levels to model solids at failure. *Computer Methods in Applied Mechanics and Engineering* 253, 558–583.
- Linder, C., Zhang, X., 2013. A marching cubes based failure surface propagation concept for three-dimensional finite elements with non-planar embedded strong discontinuities of higher-order kinematics. *International Journal for Numerical Methods in Engineering* 96 (6), 339–372.

- Lippmann, B., Schwinger, J., 1950. Variational principles for scattering processes. I. *Physical Review* 79 (3), 469–480.
- Loehnert, S., Belytschko, T., 2007. A multiscale projection method for macro/microcrack simulations. *International Journal for Numerical Methods in Engineering* 71 (12), 1466–1482.
- Maimí, P., Camanho, P., Mayugo, J., Dávila, C., 2007. A continuum damage model for composite laminates: Part I—constitutive model. *Mechanics of Materials* 39 (10), 897–908.
- Massart, T., Peerlings, R., Geers, M., 2007. An enhanced multi-scale approach for masonry wall computations with localization of damage. *International Journal for Numerical Methods in Engineering* 69 (5), 1022–1059.
- Mazars, J., Boerman, D., Piatti, G., 1981. Mechanical damage and fracture of concrete structures. In: *ICF5, Cannes (France) 1981*. Vol. 4. pp. 1499–1506.
- Mazars, J., Pijaudier-Cabot, G., 1989. Continuum damage theory-application to concrete. *Journal of Engineering Mechanics* 115 (2), 345–365.
- McLaughlin, R., 1977. A study of the differential scheme for composite materials. *International Journal of Engineering Science* 15 (4), 237–244.
- Michel, J., Moulinec, H., Suquet, P., 1999. Effective properties of composite materials with periodic microstructure: a computational approach. *Computer Methods in Applied Mechanics and Engineering* 172 (1), 109–143.
- Michel, J., Moulinec, H., Suquet, P., 2000. A computational method based on augmented lagrangians and fast fourier transforms for composites with high contrast. *CMES(Computer Modelling in Engineering & Sciences)* 1 (2), 79–88.
- Michel, J., Moulinec, H., Suquet, P., 2001. A computational scheme for linear and non-linear composites with arbitrary phase contrast. *International Journal for Numerical Methods in Engineering* 52 (1-2), 139–160.
- Michel, J.-C., Suquet, P., 2003. Nonuniform transformation field analysis. *International Journal of Solids and Structures* 40 (25), 6937–6955.
- Michel, J.-C., Suquet, P., 2004. Computational analysis of nonlinear composite structures using the nonuniform transformation field analysis. *Computer Methods in Applied Mechanics and Engineering* 193 (48), 5477–5502.
- Michler, G. H., 2008. *Electron microscopy of polymers*. Springer.
- Miehe, C., 1996. Numerical computation of algorithmic (consistent) tangent moduli in large-strain computational inelasticity. *Computer Methods in Applied Mechanics and Engineering* 134 (3), 223–240.

-
- Miehe, C., Koch, A., 2002. Computational micro-to-macro transitions of discretized microstructures undergoing small strains. *Archive of Applied Mechanics* 72 (4), 300–317.
- Miehe, C., Schröder, J., Schotte, J., 1999. Computational homogenization analysis in finite plasticity simulation of texture development in polycrystalline materials. *Computer Methods in Applied Mechanics and Engineering* 171 (3), 387–418.
- Monchiet, V., Bonnet, G., 2012. A polarization-based FFT iterative scheme for computing the effective properties of elastic composites with arbitrary contrast. *International Journal for Numerical Methods in Engineering* 89 (11), 1419–1436.
- Moos, C., 2013. An algorithm for damage mechanics based on the fast fourier transform. Ph.D. thesis, Universität Bochum.
- Mori, T., Tanaka, K., 1973. Average stress in matrix and average elastic energy of materials with misfitting inclusions. *Acta Metallurgica* 21 (5), 571–574.
- Moulinec, H., Silva, F., 2014. Comparison of three accelerated FFT-based schemes for computing the mechanical response of composite materials. *International Journal for Numerical Methods in Engineering* 97 (13), 960–985.
- Moulinec, H., Suquet, P., 1994. A fast numerical method for computing the linear and nonlinear mechanical properties of composites. *Comptes rendus de l'Académie des sciences. Série II, Mécanique, physique, chimie, astronomie* 318 (11), 1417–1423.
- Moulinec, H., Suquet, P., 1998. A numerical method for computing the overall response of nonlinear composites with complex microstructure. *Computer Methods in Applied Mechanics and Engineering* 157 (1), 69–94.
- Müller, R., 2001. Drei-D-Simulation der Mikrostrukturentwicklung in Zwei-Phasen-Materialien. Ph.D. thesis, Technische Universität Darmstadt.
- Müller, R., Kolling, S., Gross, D., 2002. On configurational forces in the context of the finite element method. *International Journal for Numerical Methods in Engineering* 53 (7), 1557–1574.
- Müller, W., 1996. Mathematical vs. experimental stress analysis of inhomogeneities in solids. *Le Journal de Physique IV* 6 (C1), C1–139.
- Mura, T., 1987. *Micromechanics of defects in solids*. Vol. 3. Kluwer Academic Pub.
- Murakami, S., 2012. *Continuum Damage Mechanics*. Springer.
- Murakami, S., Ohno, N., 1982. A constitutive equation of creep based on the concept of a creep-hardening surface. *International Journal of Solids and Structures* 18 (7), 597–609.

- Nemat-Nasser, S., Hori, M., 1999. *Micromechanics: overall properties of heterogeneous materials*. Vol. 2. Elsevier.
- Nemat-Nasser, S., Yu, N., Hori, M., 1993. Bounds and estimates of overall moduli of composites with periodic microstructure. *Mechanics of Materials* 15 (3), 163–181.
- Oden, J. T., Reddy, J. N., 2012. *An introduction to the mathematical theory of finite elements*. Courier Dover Publications.
- Ostoja-Starzewski, M., 2006. Material spatial randomness: From statistical to representative volume element. *Probabilistic Engineering Mechanics* 21 (2), 112–132.
- Paley, M., Aboudi, J., 1992. Micromechanical analysis of composites by the generalized cells model. *Mechanics of Materials* 14 (2), 127–139.
- Pan, Y., Pelegri, A. A., 2011. Progressive damage analysis of random chopped fiber composite using finite elements. *Journal of Engineering Materials and Technology* 133 (1).
- Pinho, S., Darvizeh, R., Robinson, P., Schuecker, C., Camanho, P., 2012. Material and structural response of polymer-matrix fibre-reinforced composites. *Journal of Composite Materials* 46 (19-20), 2313–2341.
- Ponte Castañeda, P., 1991. The effective mechanical properties of nonlinear isotropic composites. *Journal of the Mechanics and Physics of Solids* 39 (1), 45–71.
- Ponte Castañeda, P., 1992. New variational principles in plasticity and their application to composite materials. *Journal of the Mechanics and Physics of Solids* 40 (8), 1757–1788.
- Ponte Castañeda, P., 1996. Exact second-order estimates for the effective mechanical properties of nonlinear composite materials. *Journal of the Mechanics and Physics of Solids* 44 (6), 827–862.
- Ponte Castañeda, P., 2002. Second-order homogenization estimates for nonlinear composites incorporating field fluctuations: I—theory. *Journal of the Mechanics and Physics of Solids* 50 (4), 737–757.
- Ponte Castañeda, P., Suquet, P., 1997. Nonlinear composites. *Advances in applied mechanics* 34, 171–302.
- Puck, A., Schürmann, H., 1998. Failure analysis of FRP laminates by means of physically based phenomenological models. *Composites Science and Technology* 58 (7), 1045–1067.
- Rabotnov, Y. N., Leckie, F. A., Prager, W., 1969. *Creep problems in structural members*. North-Holland Publishing Company Amsterdam.

-
- Renard, J., Marmonier, M., 1987. Study of damage initiation in the matrix of a composite material by an homogenization method. *Rech. Aerosp.* (24), 43–51.
- Reuss, A., 1929. Berechnung der fließgrenze von mischkristallen auf grund der plastizitätsbedingung für einkristalle. *ZAMM-Journal of Applied Mathematics and Mechanics/Zeitschrift für Angewandte Mathematik und Mechanik* 9 (1), 49–58.
- Rice, J., Rudnicki, J., 1980. A note on some features of the theory of localization of deformation. *International Journal of Solids and Structures* 16 (7), 597–605.
- Rousselier, G., 1981. Finite deformation constitutive relations including ductile fracture damage. In: *Three-dimensional constitutive relations and ductile fracture*. North-Holland Publishing, pp. 331–355.
- Roussette, S., Michel, J.-C., Suquet, P., 2009. Nonuniform transformation field analysis of elastic–viscoplastic composites. *Composites Science and Technology* 69 (1), 22–27.
- Saanouni, K., 1988. Sur l’analyse de la fissuration des milieux élasto-viscoplastiques par la théorie de l’endommagement continu. Ph.D. thesis, Université de Technologie de Compiègne.
- Saanouni, K., Forster, C., Hatira, F. B., 1994. On the anelastic flow with damage. *International Journal of Damage Mechanics* 3 (2), 140–169.
- Saanouni, K., Nesnas, K., Hammi, Y., 2000. Damage modeling in metal forming processes. *International Journal of Damage Mechanics* 9 (3), 196–240.
- Sánchez-Palencia, E., 1980. Fluid flow in porous media. In: *Non-homogeneous Media and Vibration Theory*. Vol. 127. Springer, pp. 129–157.
- Sato, N., Kurauchi, T., Sato, S., Kamigaito, O., 1991. Microfailure behaviour of randomly dispersed short fibre reinforced thermoplastic composites obtained by direct sem observation. *Journal of Materials Science* 26 (14), 3891–3898.
- Schmidt, I., 2011. Numerical homogenisation of an elasto-plastic model-material with large elastic strains: macroscopic yield surfaces and the eulerian normality rule. *Computational Mechanics* 48 (5), 579–590.
- Schneider, M., 2014. Convergence of FFT-based homogenization for strongly heterogeneous media. *Mathematical Methods in the Applied Sciences*.
- Schossig, M., 2011. *Schädigungsmechanismen in faserverstärkten Kunststoffen*. Vieweg+Teubner.
- Schröder, J., 2014. A numerical two-scale homogenization scheme: the FE²-method. In: *Plasticity and Beyond*. Springer, pp. 1–64.

- Sciarra, F. M. d., 1997. General theory of damage elastoplastic models. *Journal of Engineering Mechanics* 123 (10), 1003–1011.
- Segurado, J., Llorca, J., 2002. A numerical approximation to the elastic properties of sphere-reinforced composites. *Journal of the Mechanics and Physics of Solids* 50 (10), 2107–2121.
- Simo, J., Hughes, T., 1998. *Computational inelasticity*. Springer.
- Simo, J., Ju, J., 1987a. Strain-and stress-based continuum damage models—i. formulation. *International Journal of Solids and Structures* 23 (7), 821–840.
- Simo, J., Ju, J., 1987b. Strain-and stress-based continuum damage models—ii. computational aspects. *International Journal of Solids and Structures* 23 (7), 841–869.
- Simo, J., Ju, J., 1989. On continuum damage-elastoplasticity at finite strains. *Computational Mechanics* 5 (5), 375–400.
- Simo, J., Oliver, J., Armero, F., 1993. An analysis of strong discontinuities induced by strain-softening in rate-independent inelastic solids. *Computational Mechanics* 12 (5), 277–296.
- Sliseris, J., Andrä, H., Kabel, M., 2014a. Multiscale simulation framework of strength and stiffness for medium density cellulose fiberboards. In: *Progress in Paper Physics*.
- Sliseris, J., Andrä, H., Kabel, M., Dix, B., Plinke, B., Wirjadi, O., Frolovs, G., 2014b. Numerical prediction of the stiffness and strength of medium density fiberboards. *Mechanics of Materials* 79, 73–84.
- Smit, R., Brekelmans, W., Meijer, H., 1998. Prediction of the mechanical behavior of nonlinear heterogeneous systems by multi-level finite element modeling. *Computer Methods in Applied Mechanics and Engineering* 155 (1), 181–192.
- Song, J., Belytschko, T., 2009. Multiscale aggregating discontinuities method for micro–macro failure of composites. *Composites Part B: Engineering* 40 (6), 417–426.
- Spahn, J., Andrä, H., Kabel, M., Müller, R., 2014a. A multiscale approach for modeling progressive damage of composite materials using fast Fourier transforms. *Computer Methods in Applied Mechanics and Engineering* 268, 871–883.
- Spahn, J., Andrä, H., Kabel, M., Müller, R., Linder, C., 2014b. Multiscale modeling of progressive damage in elasto-plastic composite materials. In: *Proceedings of the 11th World Congress on Computational Mechanics*.
- Staub, S., Andrä, H., Kabel, M., Zangmeister, T., 2012. Multi-scale simulation of viscoelastic fiber-reinforced composites. *Technische Mechanik* 32 (1), 70–83.

-
- Suquet, P., 1985. Local and global aspects in the mathematical theory of plasticity. *Plasticity today: modelling, methods and applications*, 279–310.
- Suquet, P., 1993. Overall potentials and extremal surfaces of power law or ideally plastic composites. *Journal of the Mechanics and Physics of Solids* 41 (6), 981–1002.
- Suquet, P., 1995. Overall properties of nonlinear composites: a modified secant moduli theory and its link with Ponte Castañeda’s nonlinear variational procedure. *Comptes rendus de l’Académie des sciences. Série II, Mécanique, physique, chimie, astronomie* 320 (11), 563–571.
- Suquet, P. M., 1987. Elements of homogenization for inelastic solid mechanics. In: *Homogenization techniques for composite media*. Vol. 105. Springer, pp. 193–278.
- Talbot, D., Willis, J., 1985. Variational principles for inhomogeneous non-linear media. *IMA Journal of Applied Mathematics* 35 (1), 39–54.
- Tasan, C., Hoefnagels, J., Geers, M., 2012. Identification of the continuum damage parameter: An experimental challenge in modeling damage evolution. *Acta Materialia* 60 (8), 3581–3589.
- Temizer, I., Wriggers, P., 2008. On the computation of the macroscopic tangent for multiscale volumetric homogenization problems. *Computer Methods in Applied Mechanics and Engineering* 198 (3), 495–510.
- Terada, K., Hori, M., Kyoya, T., Kikuchi, N., 2000. Simulation of the multi-scale convergence in computational homogenization approaches. *International Journal of Solids and Structures* 37 (16), 2285–2311.
- Torquato, S., 2002. *Random heterogeneous materials: microstructure and macroscopic properties*. Vol. 16. Springer.
- Tsai, S., Wu, E., 1971. A general theory of strength for anisotropic materials. *Journal of composite materials* 5 (1), 58–80.
- Tvergaard, V., Needleman, A., 1984. Analysis of the cup-cone fracture in a round tensile bar. *Acta metallurgica* 32 (1), 157–169.
- Unger, J. F., Eckardt, S., 2011. Multiscale modeling of concrete. *Archives of Computational Methods in Engineering* 18 (3), 341–393.
- Voigt, W., 1889. Ueber die beziehung zwischen den beiden elastizitätskonstanten isotroper körper. *Annalen der Physik* 274 (12), 573–587.
- Weinan, E., Engquist, B., Li, X., Ren, W., Vanden-Eijnden, E., 2007. Heterogeneous multiscale methods: a review. *Communications in Computational Physics* 2 (3), 367–450.

- Wriggers, P., 2008. *Nonlinear finite element methods*. Springer.
- Zeller, R., Dederichs, P., 1973. Elastic constants of polycrystals. *Physica status solidi* (b) 55 (2), 831–842.
- Zeman, J., Vondřejc, J., Novák, J., Marek, I., 2010. Accelerating a FFT-based solver for numerical homogenization of periodic media by conjugate gradients. *Journal of Computational Physics* 229 (21), 8065–8071.
- Zhang, W., Cai, Y., 2010. *Advanced Topics In Science and Technology In China: Continuum Damage Mechanics and Numerical Applications*. Springer.
- Zhu, Y., Cescotto, S., 1995. A fully coupled elasto-visco-plastic damage theory for anisotropic materials. *International Journal of Solids and Structures* 32 (11), 1607–1641.
- Zienkiewicz, O. C., Taylor, R. L., 2005. *The finite element method for solid and structural mechanics*. Butterworth-Heinemann.
- Zohdi, T., Feucht, M., Gross, D., Wriggers, P., 1998. A description of macroscopic damage through microstructural relaxation. *International Journal for Numerical Methods in Engineering* 43 (3), 493–506.
- Zohdi, T., Wriggers, P., 1999. A domain decomposition method for bodies with heterogeneous microstructure based on material regularization. *International Journal of Solids and Structures* 36 (17), 2507–2525.
- Zohdi, T., Wriggers, P., 2008. *An introduction to computational micromechanics*. Vol. 20. Springer.

Curriculum Vitae

Name:	Johannes Spahn
1988 – 1992	Walther-Grundschule, Würzburg
1992 – 2001	Röntgen-Gymnasium, Würzburg Abschluss: Allgemeine Hochschulreife, Abitur
2001 – 2002	Zivildienst Geriatrische Rehabilitationsklinik, Würzburg
2002 – 2007	Studium der Kunststoff- und Elastomertechnik Fachhochschule Würzburg-Schweinfurt Abschluss: Diplom-Ingenieur (FH)
2007 – 2009	Studium des Maschinenbaus Friedrich-Alexander-Universität Erlangen-Nürnberg Abschluss: Master of Science
2011 – 2014	Doktorand, Wissenschaftlicher Angestellter Fraunhofer-Institut für Techno- und Wirtschaftsmathematik Lehrstuhl für Technische Mechanik, TU Kaiserslautern